Experimental Near-Field Characterization of Plasmonic Nanostructures

Dissertation

zur

Erlangung des Doktorgrades (Dr. rer. nat.)

der

Mathematisch-Naturwissenschaftlichen Fakultät

der

Rheinischen Friedrich-Wilhelms-Universität Bonn

von

Mike Prämassing

aus

Adenau

Bonn, 2020

Abstract

A promising platform to overcome the diffraction limit in nanophotonic applications is the field of plasmonics, which involves so-called surface plasmon polaritons (SPPs). A SPP results from the coupling between an electromagnetic wave and charge density oscillations in a metal. Essentially, SPPs are bound electromagnetic waves, which propagate along an interface between the metal and a dielectric and exhibit an evanescent character in the direction perpendicular to this interface. This characteristic conditions a high confinement and enhancement of the involved electromagnetic fields at the metal-dielectric interface. Shrinking the SPP propagation degree of freedom to one dimension in plasmonic waveguides or localizing the SPPs completely on plasmonic nanostructures can further increase the field confinement and enhancement. These properties qualify plasmonic nanostructures and waveguides for various applications in nanophotonics. While plasmonic waveguides are promising candidates for the realization of nanophotonic circuits, plasmonic nanostructures are successfully applied for biological and chemical sensing or in nanoscale quantum optics. Due to the bound nature of the SPPs, conventional optical microscopy only allows for their indirect observation through leakage radiation from propagating SPPs or scattered radiation from localized SPPs (LSPPs). However, there are near-field imaging techniques available, which allow for probing the evanescent fields of the SPPs perpendicular to the metal-dielectric interface directly with a resolution far beyond the diffraction limit.

In this work, two different near-field imaging techniques, namely electron energy-loss spectroscopy (EELS) and scattering-type scanning near-field optical microscopy (s-SNOM) are applied on plasmonic structures. The investigated plasmonic sample systems range from extended array structures featuring thin-film SPPs over one dimensional plasmonic waveguide structures up to LSPPs occurring on random nanoporous gold structures. A brief introduction to the fabrication of plasmonic nanostructures is presented in chapter 3 including the preparation of solid and nanoporous thin gold films and patterning of the first via focused ion beam milling. In this context, a new approach for the fabrication of freestanding structured thin gold film is presented.

In chapter 5, plasmonic hole arrays in both freestanding and silicon nitride supported thin gold films are investigated by near-field measurments utilizing EELS and s-SNOM, respectively. Both techniques are complemented with far-field optical transmission spectroscopy. Upon resonant excitation of SPPs via the hole arrays, the samples exhibit an extraordinary optical transmission, which can be explained by the SPPs passing through the holes and scattering to far-field radiation via the array on the other side of the film. The hole

arrays feature different standing wave patterns of the resonantly excited SPPs for different excitation energies according to the eigenmodes of the arrays. These standing wave patterns are observed by the near-field measurements and consistently attributed to corresponding features in the optical far-field transmission spectra.

In chapter 6, plasmonic slot waveguides (PSWs) and far-field couplers for an efficient excitation of their fundamental guided mode are investigated by transmission mode s-SNOM measurements. In the first part, a parametric study on PSWs of different widths between 50 nm and 170 nm in single- and poly-crystalline gold films is performed in order to study the effect of the material quality on the mode propagation. The near-field investigation at a wavelength of 1520 nm reveals the asymmetry of the guided mode and its propagation parameters, i.e. its effective mode index and propagation length. The former is shown to decrease with increasing slot width for both film types, which can be attributed to the general correlation between the mode confinement and the mode index in plasmonic waveguides. Interestingly, the propagation length exhibits a maximum at a certain slot width, which can be explained by a trade-off between Ohmic and leakage radiation losses. For the very narrow PSWs below 80 nm, the propagation length is improved by up to a factor of two when using the high quality single-crystalline films. In the second part of the chapter, the selective excitation of two PSWs by a plasmonic ring coupler upon illumination with circularly polarized light is qualitatively demonstrated via transmission mode s-SNOM measurements. The excitation is mostly restricted to one or the other output PSW when switching the helicity of the circularly polarized excitation beam. A spectroscopic analysis reveals that the directional functionality of the coupler is preserved in a wavelength range between 1450 nm and 1650 nm.

In chapter 7, near-field measurements are performed on nanoporous gold films via EELS on an electron transparent substrate and via s-SNOM on a glass substrate. In all cases, hotspots originating form LSPPs are observed. The EEL spectra reveal LSPP resonances at energies between 1.0 eV and 1.5 eV, which give rise to the hotspots. The s-SNOM measurements are performed in three measurement modi, namely reflection mode with primarily vertical and horizontal incident polarization and transmission mode configuration. The best visibility of the hotspots is provided by measurements with horizontal incident polarization both in reflection and transmission mode. The occurrence of hotspots in the transmission mode measurement implies that some LSPPs range through the entire 125 nm thick film.

Contents

Introduction

Light is probably the most important information transfer channel for human beings. Naturally, this includes the perception of our environment by the sense of light. Furthermore, electromagnetic waves are indispensable for wireless or fiber based signal transmission in telecommunication and technical applications. Also for information processing, light-based computational devices may be an option to beat the current frequency limit of conventional electronic computers [1]. However, the high level of miniaturization in modern electronic devices is much harder to achieve with light-based computational or sensing and detection devices. This is due to the diffraction limit, which inhibits the confinement of a light wave to dimensions smaller than roughly half of its optical wavelength $\lambda/2$ [2, 3].

A promising platform to overcome the diffraction limit in nanophotonic applications is the field of plasmonics, which involves so-called surface plasmon polaritons (SPPs) [4, 5]. A SPP results from the coupling between an electromagnetic wave and charge density oscillations in a metal. Essentially, SPPs are bound electromagnetic waves, which propagate along an interface between the metal and a dielectric and exhibit an evanescent character in the direction perpendicular to this interface. This characteristic conditions a high confinement and enhancement of the involved electromagnetic fields at the metal-dielectric interface. Shrinking the SPP propagation degree of freedom to one dimension in plasmonic waveguides or localizing the SPPs completely on plasmonic nanostructures can further increase the field confinement and enhancement. These properties qualify plasmonic nanostructures and waveguides for various applications in nanophotonics. For instance, plasmonic waveguides [6–10] are promising candidates for the realization of nanophotonic circuits [1]. The huge electromagnetic field intensity in the proximity of plasmonic nanostructures leads to a strongly enhanced light-matter interaction, which can be utilized for sensing applications [11–13], surface enhanced Raman scattering [14, 15] or efficient coupling to quantum emitters [16, 17]. The large scattering cross sections and strong resonances of plasmonic nanostructures make them also favourable as building blocks for artificial composite materials including metamaterials [18] and metasurfaces [19].

However, the great advantages of plasmonic structures come at the price of large energy dissipation, due to significant Ohmic losses caused by the scattering of free electrons at optical frequencies. This implies limitations to the quality factor and lifetimes of resonances in plasmonic nanostructures [4] and the propagation distance of light in plasmonic waveguides [20–22]. One possible attempt to face these limitations is improving the material quality by using single-crystalline metallic nanostructures [23] and waveguides [24, 25]. In this context, single-crystalline plasmonic slot waveguides (PSWs) are investigated in section 6.1 and the work was published in reference [21].

The diffraction limit of light not only entails limitations on technical applications, but also on the scientific characterization of samples via optical microscopy. Importantly, the fundamental limit of $\lambda/2$ also holds for the imaging resolution. In contrast, utilizing electron microscopy or atomic force microscopy (AFM) [26], an atomic resolution can be achieved in the extreme case [27, 28]. However, these techniques do not reveal optical information, i.e. information of the electromagnetic near-fields at the sample surface upon optical excitation in the first place. This information can only be revealed by near-field imaging techniques like scanning near-field optical microscopy (SNOM) [29, 30], which is based on AFM, or electron energy-loss spectroscopy (EELS) [31, 32] and cathodoluminescence (CL) spectroscopy [33], which are based on electron microscopy. Among many other applications, these techniques have been proven to be powerful tools for the near-field characterization of plasmonic nanostructures [32, 34–36], waveguides [7, 20] and freely propagating SPPs [37].

In this thesis, the optical near-fields of different kinds of plasmonic structures are investigated utilizing EELS and scattering-type SNOM (s-SNOM). Chapter 2 introduces the theoretical background necessary for the understanding of the following chapters. The phenomenon of electromagnetic wave propagation in a medium is derived from Maxwell's equations, followed by a discussion of the diffraction limit and evanescent fields in the framework of Fourier optics. Lastly, an introduction to plasmonics is given by covering the optical properties of gold and a mathematical description of SPP waves. Chapter 3 includes different fabrication methods of thin gold films as a basis for plasmonic samples. Furthermore, nanopatterning of the gold films via focused ion beam (FIB) milling for the fabrication of plasmonic nanostructures is introduced. In chapter 4, the two utilized near-field imaging techniques, namely EELS and s-SNOM are explained. In chapter 5, EELS and s-SNOM are applied on two different sample systems of plasmonic hole arrays. The near-field measurements are complemented by optical far-field transmission spectra. Chapter 6 presents s-SNOM measurements on PSWs and coupling structures to excite the PSWs from the far-field. Chapter 7 reports on near-field investigations via EELS and s-SNOM on nanoporous gold films. Lastly, a conclusion of the most important findings in this thesis and ideas for further research on these topics is given in chapter 8.

Theoretical foundations

This chapter introduces some essential theoretical foundations needed to understand the utilized methods presented in chapter 4 and the results of the experimental investigations in the following chapters. In the first section, a very brief introduction to the foundations of classical electrodynamics is given including Maxwell's equations in matter as a starting point for the derivation of the Helmholtz equation. Plane waves together with the disperion of light in matter follow as a solution of the Helmholtz equation. In the second section, fundamental limits of resolution of optical microscopy are tackled and the concept of evanescent waves is introduced in the framework of Fourier optics. The findings of this section clarify the purpose and necessity of near-field imaging techniques to overcome the diffraction limit, which are elaborated in detail in chapter 4. The last section elaborates the phenomenon of SPPs, which play a central role in all experimental investigations presented in this thesis.

2.1 Foundations of classical electrodynamics

In 1873, James Clerck Maxwell established a fundamental set of equations, which fully describe classical electrodynamics in combination with the Lorentz force law. The so-called macroscopic Maxwell equations [5]

$$
\begin{aligned}
\boldsymbol{\nabla} \times \boldsymbol{H}(\boldsymbol{r}, t) &= \frac{\partial \boldsymbol{D}(\boldsymbol{r}, t)}{\partial t} + \boldsymbol{j}(\boldsymbol{r}, t), \\
\boldsymbol{\nabla} \times \boldsymbol{E}(\boldsymbol{r}, t) &= -\frac{\partial \boldsymbol{B}(\boldsymbol{r}, t)}{\partial t}, \\
\boldsymbol{\nabla} \cdot \boldsymbol{B}(\boldsymbol{r}, t) &= 0, \\
\boldsymbol{\nabla} \cdot \boldsymbol{D}(\boldsymbol{r}, t) &= \rho(\boldsymbol{r}, t),
\end{aligned}
\tag{2.1}
$$

comprise four partial differential equations describing the interplay between electric and magnetic fields, free charges and electric currents in matter. The six occurring quantities are

the electric field E, the magnetic field H, the electric displacement D, the magnetic induction B as well as the free charge density ρ and the free current density j in matter. The electric displacement and the magnetic induction include the response of the material to the external electric and magnetic field by taking into account the macroscopic polarization $P(r, t)$ and magnetization $M(r, t)$ of the material [5]:

$$
\begin{aligned}
D(r, t) &= \epsilon_0 E(r, t) + P(r, t), \\
B(r, t) &= \mu_0 [H(r, t) + M(r, t)].
\end{aligned}
\tag{2.2}
$$

The quantities ϵ_0 and μ_0 are the electric permittivity and the magnetic permeability of vacuum, respectively. The macroscopic polarization and magnetization are related to the external electric and magnetic field via material specific response parameters χ_e and χ_m. In linear, non-dispersive and isotropic media, the relations take the simple form

$$
\begin{aligned}
P &= \epsilon_0 \chi_e E, \\
M &= \chi_m H,
\end{aligned}
\tag{2.3}
$$

which can be used to rewrite equations (2.2) as

$$
\begin{aligned}
D &= \epsilon_0 \epsilon E, \\
B &= \mu_0 \mu H,
\end{aligned}
\tag{2.4}
$$

with the introduced material parameters $\epsilon = 1 + \chi_e$ and $\mu = 1 + \chi_m$. Together with Ohm's law [38]

$$
j = \sigma E,
\tag{2.5}
$$

the material equations (2.3) and (2.4) are commonly referred to as constitutive relations [5, 39]. Here, σ denotes the electric conductivity of the material. When discarding the restrictions to the medium made above, the constitutive relations become more involved. For instance, to account for nonlinear optical effects in a medium, the right hand sides in equations (2.4) have to be supplemented with higher order terms. For anisotropic media, the material parameters ϵ and μ have to be represented in tensorial form. When temporal and spatial dispersion is apparent, the multiplication in equations (2.4) has to be replaced by a convolution integral over space and time. For the electric displacement field, the convolution integral reads [5]

$$
D(r, t) = \epsilon_0 \iint \bar{\epsilon}(r - r', t - t') E(r', t') \mathrm{d}r' \mathrm{d}t',
\tag{2.6}
$$

where $\bar{\epsilon}$ is the response function in space and time. The convolution integral can be formulated analogously for the magnetic field with the replacements $D \rightarrow B$, $E \rightarrow H$, $\bar{\epsilon} \rightarrow \bar{\mu}$ and $\epsilon_0 \rightarrow \mu_0$. The electric displacement D not only depends on the instantaneous and local electric field at time t and location r, but also on the electric field at all previous times t' and

neighboring locations r'. The integration over space accounts for spatial dispersion, which is present in so-called non-local media. These non-local effects are rarely present in naturally occurring materials but can appear e.g. in artificially designed metal-dielectric composite materials, where the structural sizes of the metallic elements approach the field penetration depths [40]. Since spatial dispersion has to be taken into account only in very special cases, it is not considered in the following. However, temporal dispersion, which is accounted for by the time integration is very common and more or less present in almost every natural medium.

Further simplification of Maxwell's equations and of the convolution integral in time domain can be achieved by transforming all quantities to the frequency domain via Fourier transformation. For an arbitrary quantity $a(r,t) \in \{E, D, H, B, j, \rho, \epsilon, \mu, \sigma\}$ the Fourier transform is given by

$$\hat{a}(r,\omega) = \frac{1}{2\pi} \int_{-\infty}^{\infty} a(r,t)e^{i\omega t}\mathrm{d}t, \tag{2.7}$$

with the angular frequency ω. In frequency space, the relation in equation (2.6) and its magnetic counterpart simplify to

$$\hat{D}(r,\omega) = \epsilon_0 \hat{\epsilon}(r,\omega)\hat{E}(r,\omega),$$
$$\hat{B}(r,\omega) = \mu_0 \hat{\mu}(r,\omega)\hat{H}(r,\omega), \tag{2.8}$$

due to the convolution theorem. Furthermore, the time derivatives in Maxwell's equations are replaced by $-i\omega$, which yields [5]

$$\nabla \times \hat{H}(r,\omega) = -i\omega\hat{D}(r,\omega) + \hat{j}(r,\omega),$$
$$\nabla \times \hat{E}(r,\omega) = i\omega\hat{B}(r,\omega),$$
$$\nabla \cdot \hat{B}(r,\omega) = 0,$$
$$\nabla \cdot \hat{D}(r,\omega) = \hat{\rho}(r,\omega). \tag{2.9}$$

The following discussions are restricted to monochromatic time dependencies of the occurring fields, i.e. all fields E, D, H, B can be written as

$$E(r,t) = \mathrm{Re}[E(r)e^{i\omega_0 t}]. \tag{2.10}$$

Since Maxwell's equations defined in (2.9) hold separately for every complex frequency component $\hat{E}(r,\omega)$, they apply in particular to the complex amplitude $\hat{E}(r,\omega_0) = E(r)$ of the monochromatic fields. As the above arguments hold for every frequency ω_0, the notation of the quantities in Fourier space is omitted as follows: $\hat{E}(r,\omega_0) \to E(r)$ for the quantities E, D, H, B, j, ρ and $\hat{\epsilon}(r,\omega_0) \to \epsilon(r,\omega) \to \epsilon(\omega)$ for the material parameters ϵ, μ, σ. The second replacement of the material parameters is only possible for homogeneous media. Furthermore, an isotropic and linear medium is assumed in the following. Using

the constitutive relations in (2.8) and Ohm's law in (2.5), D,B and j can be expressed via E and H in the two curl equations in (2.9). The resulting two equations can be decoupled by multiplying $\mu(\omega)^{-1}$ and applying the curl operator to both sides of the second equation. Subsequently substituting $\nabla \times H(r)$ using the first equation results in the wave equation for the electric field [5]

$$\nabla \times \mu(\omega)^{-1} \nabla \times E(r) - \frac{\omega^2}{c^2}\left[\epsilon(\omega) + \frac{i\sigma(\omega)}{\omega\epsilon_0}\right] E(r) = 0, \tag{2.11}$$

where $c = 1/\sqrt{\epsilon_0\mu_0}$ represents the speed of light in vacuum. The expression in brackets considers the material response to electric fields including the polarization via $\epsilon(\omega)$ and the generation of free currents in a conductive medium via $i\sigma(\omega)/\omega\epsilon_0$. These two effects are ordinarily not distinguished and the expression in brackets is considered by a single complex-valued material constant $\left[\epsilon(\omega) + i\sigma(\omega)/\omega\epsilon_0\right] \rightarrow \epsilon(\omega) := \epsilon'(\omega) + i\epsilon''(\omega)$, which is commonly referred to as the dielectric function of the medium. The imaginary part of the dielectric function ϵ'' determines the optical losses in a medium. For optical frequencies, relevant in this thesis, naturally occurring materials exhibit no magnetism ($\mu(\omega) = 1$). Furthermore, assuming a charge free medium ($\rho = 0$), the result in (2.11) can be further simplified by applying the identity $\nabla \times \nabla\times = -\nabla^2 + \nabla\nabla$ and utilizing the last equation in (2.9) to obtain the Helmholtz equation

$$\left(\nabla^2 + \frac{\omega^2}{c^2}\epsilon(\omega)\right) E(r) = 0. \tag{2.12}$$

A well known solution of (2.12) is the monochromatic plane wave [39]:

$$E(r, t) = E_0 e^{ikr - i\omega t}. \tag{2.13}$$

Analogous equations to (2.12) and (2.13) can be found for the magnetic field. The plane wave solutions for the electric and magnetic field form a transverse electromagnetic wave, i.e. the complex amplitude vectors of the plane wave E_0 and B_0 and the the wavevector k form a set of orthogonal vectors. The wavevector holds the information about the propagation direction and the spatial oscillation frequency given by its magnitude:

$$|k| := k = \sqrt{\epsilon(\omega)}\frac{\omega}{c} := n(\omega)\frac{\omega}{c} := n(\omega)k_0, \tag{2.14}$$

where $n(\omega) = \sqrt{\epsilon(\omega)}$ defines the refractive index of the medium and k_0 is the magnitude of the wavevector in vacuum. Equation (2.14) is generally called the dispersion relation. The dispersion relation determines the phasor in the plane wave solution in (2.13) and essentially describes the propagation of the electromagnetic wave in a medium.

2.2 Diffraction limit and Fourier optics

In the last section, the fundamental equations of classical electrodynamics - Maxwell's equations - have been used to derive electromagnetic waves in media, which essentially describe the propagation of light. Utilizing light as a probe to examine a sample consisting of small features, i.e. using optical microscopy, is often a natural starting point for a scientific sample characterization. However, due to the wave nature of light, the achievable resolution in optical microscopy is fundamentally limited to about half of the light wavelength. The fundamental theory of resolution was stated by Ernst Abbe in 1873 [2] and Lord Raighley in 1879 [3]. The key result of their work is a formula for the minimum distance d between two distinct points to be separately resolved in an optical microscope [2]:

$$d = 0.61 \frac{\lambda_0}{n \sin(\theta)},$$
(2.15)

which is commonly referred to as Abbe's diffraction limit. Thus, the imaging resolution is connected to the employed light wavelength in vacuum $\lambda_0 = 2\pi c/\omega$ and the numerical aperture (NA) $n \sin(\theta)$ of the imaging system, where θ is the maximum light collection angle of the microscope objective. This limit holds whenever the observer or detector is far away from the object compared to the light wavelength, which is commonly referred to as far-field. The information of features with sizes smaller than d are lost during light propagation from the object to the far-field. However, in the near-field region closer to the sample than the light wavelength, this information is still present.

The framework of Fourier optics provides a simple and elegant approach to describe the gradual loss of information about small features during light propagation from the surface of a sample to the far-field. The basic concept of the Fourier optics approach is described in the following, based on the textbooks [5] and [41]. Without loss of generality the coordinate system is chosen such that the sample surface lies in the x-y-plane. The complex electric field distribution $\boldsymbol{E}(x, y, z = 0)$ at the sample surface arising from reflection or scattering of incident light can be decomposed into its spatial frequency spectrum via Fourier transformation:

$$\hat{\boldsymbol{E}}(k_x, k_y; z = 0) = \frac{1}{2\pi} \iint\limits_{-\infty}^{\infty} \boldsymbol{E}(x, y, z = 0) e^{-i(k_x x + k_y y)} \mathrm{d}x \, \mathrm{d}y,$$
(2.16)

where k_x and k_y denote the spatial frequency counterparts of the spatial x and y coordinates. Consequently, the original complex field distribution can be recovered by the inverse Fourier transform:

$$\boldsymbol{E}(x, y, 0) = \frac{1}{2\pi} \iint\limits_{-\infty}^{\infty} \hat{\boldsymbol{E}}(k_x, k_y; 0) e^{i(k_x x + k_y y)} \mathrm{d}k_x \mathrm{d}k_y.$$
(2.17)

The electric field distribution above the sample surface (x-y-plane) can be calculated similarly

in dependence on the z-coordinate with the knowledge of $\hat{E}(k_x, k_y; z)$:

$$E(x, y, z) = \frac{1}{2\pi} \iint\limits_{-\infty}^{\infty} \hat{E}(k_x, k_y; z) e^{i(k_x x + k_y y)} \mathrm{d}k_x \mathrm{d}k_y. \tag{2.18}$$

Thus, the evolution of the Fourier components $\hat{E}(k_x, k_y; z)$ during propagation along the z-axis directly determines the field distribution $E(x, y, z)$. Assuming $E(x, y, z)$ to be a time harmonic field as in the last section (c.f. equation (2.10)) it has to satisfy the Helmholtz equation (2.12). Inserting equation (2.18) into the Helmholtz equation leads to the following differential equation:

$$\frac{d^2}{dz^2} \hat{E}(k_x, k_y; z) + (k^2 - k_x^2 - k_y^2) \hat{E}(k_x, k_y; z) = 0. \tag{2.19}$$

An elementary solution of this differential equation is given by

$$\hat{E}(k_x, k_y; z) = \hat{E}(k_x, k_y; 0) e^{\pm i k_z z}, \tag{2.20}$$

with $k_z := \sqrt{k^2 - k_x^2 - k_y^2}$. Finally, the field distribution in any plane parallel to the x-y-plane can be recovered by inserting equation (2.20) into (2.18):

$$E(x, y, z) = \frac{1}{2\pi} \iint\limits_{-\infty}^{\infty} \hat{E}(k_x, k_y; 0) e^{i(k_x x + k_y y \pm k_z z)} \mathrm{d}k_x \mathrm{d}k_y. \tag{2.21}$$

The latter equation is commonly referred to as the angular spectrum representation. The integral can be regarded as a summation of plane wave contributions with various transverse spatial frequencies (k_x, k_y). The plane wave contributions are weighted by the complex Fourier components $\hat{E}(k_x, k_y; z)$ in order to reconstruct the field distribution $E(x, y, z)$ in real space. The propagation of the plane wave components is essentially governed by the propagator

$$e^{\pm i k_z z} = e^{\pm i \sqrt{k^2 - k_x^2 - k_y^2} z} \tag{2.22}$$

in equation (2.20). The "$\pm$" in the exponent accounts for a wave propagation in positive "+" and negative "$-$" z-direction, respectively.

In a lossless but dispersive medium, where n and thus also k are purely real numbers, one can distinguish between two different cases, for which the propagator changes its properties fundamentally. Thereby, the relevant quantity for the behaviour of the propagator is the total transverse wavevector component $q = \sqrt{k_x^2 + k_y^2}$. For the case $q < k$, k_z is a purely real number and the propagator only affects the phase of the Fourier components $\hat{E}(k_x, k_y; z)$, which corresponds to propagating plane waves. The propagation angle θ of the respective

plane wave components with respect to the z-axis is determined by $\sin(\theta) = q/k$. In case of $q > k$, the wave vector component k_z is a purely imaginary number, which leads to an exponential field decay in z-direction. These rapidly decaying field components are called evanescent waves. Combining the latter two findings, every lossless medium can be regarded as an efficient low-pass filter for the spatial frequency spectrum of the field distribution at the sample surface. The cut-off value q_{max} for the transverse spatial frequency component is determined by the refractive index of the medium and the light wavelength:

$$q_{max} = k = nk_0 = n\frac{2\pi}{\lambda_0}. \tag{2.23}$$

Only the contributions to the plane wave spectrum with transverse spatial frequencies below the cut-off can contribute to the field distribution in the far-field. The higher frequency components are subject to rapid decay within the near-field zone. Note that $q_{max} = k$ corresponds to propagation angles of $\theta = 90°$ and represents the ultimate limit of propagating waves. In microscopy applications, the maximum collection angle $\theta < 90°$ is determined by the NA of the objective and shrinks the maximum transverse spatial frequency further to $q_{max} = k\sin(\theta)$.

Concluding the findings above, the Fourier optics approach enables the description of the information-loss during light propagation from the near- to the far-field. For instance, the information about very small features at the sample surface is contained in the Fourier components $\hat{E}(k_x, k_y; 0)$ with very high spatial frequencies k_x and k_y, eventually causing $q > q_{max}$ and thus rapid decay of this information upon propagation. The corresponding smallest feature size d, which can be carried by propagating waves to the far-field can be estimated by

$$d \approx \frac{1}{q_{max}} = \frac{1}{k\sin(\theta)} = \frac{\lambda_0}{2\pi\sin(\theta)n}. \tag{2.24}$$

Equation (2.24) recovers Abbe's diffraction limit in equation (2.15) except for a constant factor.

From the discussion above, one may conclude, that in any case, the maximum achievable resolution of an imaging system is ultimately limited by the free space wavelength of the utilized light, connected to its frequency or energy. However, there are approaches to circumvent the fundamental limit of diffraction. In 2000, John Pendry proposed a "perfect lens", which is theoretically able to recover the image of an object with its full information, i.e. with its complete angular spectrum including all evanescent wave components [42]. This "perfect lens" relies on a hypothetical negative index material with $\epsilon = \mu = -1$, which turns the exponential decay of the evanescent wave components into an equivalent exponential growth in order to compensate the evanescent decay in vacuum. However, the state of the art experimental realization attempts of such a negative index material involve strong resonances, which restricts its functionality to a narrow frequency band accompanied by large losses at optical frequencies [18]. Other concepts to circumvent the diffraction limit include the so-called super- and hyperlenses [43–45]. For the latter, propagating waves are

allowed for in-plane wavevectors $q \gg k$. However, also these approaches facilitate only limited functionalities due to their narrow bandwidth and large optical losses. Apparently, transferring all information about deep subwavelength spatial features of a sample from the object plane to the image plane simultaneously remains a nearly impossible task. Nevertheless, a direct measurement of the optical field at a certain position of the sample surface is possible by utilizing a deep subwavelength probe in the near-field region of the sample, where the evanescent waves are still present. A raster-scan of this near-field probe can reveal the field distribution directly at the sample surface with a resolution far beyond the diffraction limit. These scanning probe techniques for near-field imaging constitute a central part of this thesis and are extensively discussed in chapter 4 and utilized for near-field measurements in chapters 5, 6 and 7.

2.3 Surface plasmon polaritons

In the previous section, the propagation of light in three-dimensional (3D) space has been described by the simple model of plane wave components in homogeneous dispersive media. In this context, spectral plane wave components have been classified as propagating waves and evanescent waves depending on the magnitude of the lateral wavevector component q. Evanescent waves are subject to a rapid decay within the near-field region around the source object. Another optical phenomenon, that involves the concept of propagating and evanescent waves are surface waves, which can appear at interfaces between two materials with different dielectric functions $\epsilon(\omega)$ under certain circumstances. Per definition, surface waves can propagate freely along the interface, but exhibit an evanescent character perpendicular to the interface i.e. they are tightly bound to the interface within the near-field region. Prominent examples for such bound surface waves are SPPs [4, 46] or surface phonon polaritons [44, 47, 48]. Both of them result from an opposite algebraic sign of the dielectric function of the media at both sides of the interface. Further kinds of surface waves are for example hybrid surface phonon plasmon polaritons [49, 50], Dirac SPPs on graphene monolayers [51, 52], or Dyakonov waves, which can occur at an interface between isotropic and anisotropic media [53, 54]. In the following, only SPPs will be discussed in more detail for which the change of the algebraic sign of the dielectric function, or to be more precise, of the real part of the dielectric function, occurs at a metal-dielectric interface.

2.3.1 A simple model to describe the permittivity of metals

The negative permittivity provided by the metallic medium over a broad spectral range results from oscillations of the free conduction electrons with respect to the atomic cores driven by the external light field. A very simple model to analytically derive an expression for the dielectric function of a metal was initially introduced by Paul Drude in 1900 [55] and is still very commonly used as a simple description of the optical properties of metals. A brief insight into the model is given here based on reference [5]. The model assumes that only the

conduction electrons, which are approximated as "free" contribute to the optical properties. In this context the term "free" electrons excludes interactions among themselves or with the remaining core ions. The only impacts accounted for, which hamper their movement are distinct collision events. The average distance of free movement for an electron between two collision events is called mean free path l. Given this simplifications, the equation of motion for a conduction electron can be written as

$$m_e \frac{d^2 r}{dt^2} + m_e \Gamma \frac{dr}{dt} = e E_0 e^{-i\omega t},$$ (2.25)

with the position r, the charge e and the mass m_e of an electron. The damping rate $\Gamma = v_F / l$ is governed by the Fermi velocity v_F and the mean free path l. The monochromatic external light field causes the driving force on the right hand side of equation (2.25). The equation of motion can be solved using the ansatz of a harmonic oscillation $r(t) = r_0 e^{-i\omega t}$. Calculating the macroscopic polarization from the solution via $P = n_e e r$ and using equations (2.2), (2.3) and (2.4) one can find the following expression for the dielectric function of a metal [5]:

$$\epsilon_{\text{Drude}} = 1 - \frac{\omega_p^2}{\omega^2 + i\Gamma\omega} = 1 - \frac{\omega_p^2}{\omega^2 + \Gamma^2} + i \frac{\Gamma \omega_p^2}{\omega(\omega^2 + \Gamma^2)}.$$ (2.26)

Here,

$$\omega_p = \sqrt{\frac{n_e e^2}{m_e \epsilon_0}}$$ (2.27)

is the so-called plasma frequency and n_e denotes the number density of the conduction electrons. In the last part of equation (2.26) the dielectric function is explicitly split into its real part ϵ' and imaginary part ϵ''. For $\omega > \omega_p$, i.e. if the light frequency exceeds the plasma frequency, the real part of the dielectric function takes positive values. However for light frequencies below the plasma frequency ($\omega < \omega_p$), the model predicts a negative real part of the permittivity.

Of course, in reality there are more contributions to the optical properties of metals than only the collective oscillation of the conducting electrons. The most prominent additional contribution to mention are oscillations of the valence electrons, which are bound to the atomic cores. They can also be treated in the framework of a simple analytic model quite similar to the Drude model discussed above, which has been introduced by Lorentz in 1905 [56–58]. In this model, the bound electrons are described by a driven harmonic oscillator model. Therefore, the left hand side of the equation of motion in (2.25) is extended by a restoring force term. The damping term, which considered the collisions in the Drude model primarily considers radiative damping in this case. The result is a resonant behaviour of the oscillation amplitude r_0 in the presence of an electronic transition between two energetic levels of the atom. This resonant behaviour is conveyed to the behaviour of the permittivity. Each possible interband transition between atomic energy levels of the valence electrons

can contribute with resonances of different amplitude to the total dielectric function of the material. The sum of all interband transition resonances and the response from the Drude model can describe the optical properties of a metal in a good approximation. The interband transitions often result in a significant deviation from the simple Drude model in the visible spectral range. However, for frequencies sufficiently below the lowest frequency interband transition (and the plasma frequency) the real part of the permittivity can be safely considered negative for metals. In this regime, the permittivity can still be described by a modified Drude model, which accounts for the high frequency interband transitions by a constant additive component ϵ_∞:

$$\epsilon_{\text{Drude}} = \epsilon_\infty - \frac{\omega_{\text{p}}^2}{\omega^2 + i\Gamma\omega}. \tag{2.28}$$

Figure 2.1 shows a comparison between the dielectric data of gold measured by Johnson and Christy [59] with a fit of the model in equation (2.28) [32]. The model fit is in very good agreement with the measured data in the whole near-infrared regime. According to the experimental data, the dielectric function of gold exhibits a negative real part ($\epsilon' < 0$) in the complete visible and near-infrared range, which facilitates the existence of SPPs at a gold-dielectric interface.
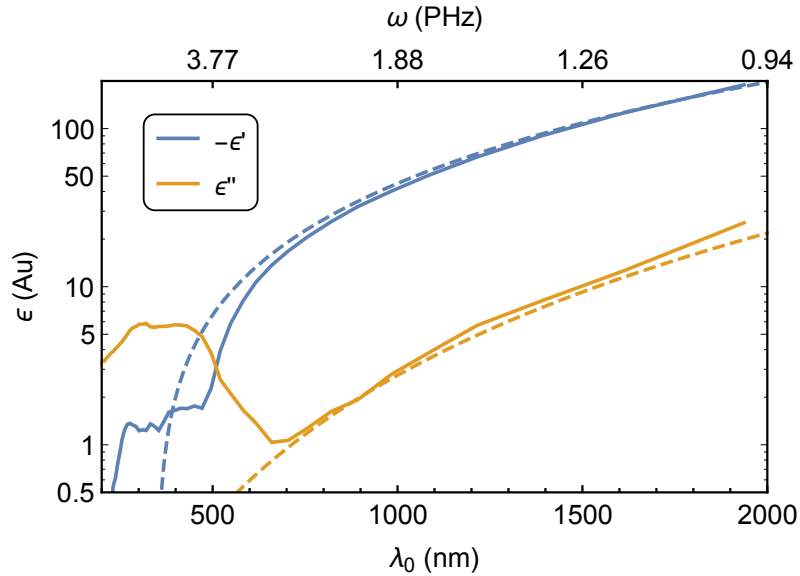

Figure 2.1: Negative real part $-\epsilon'$ and imaginary part ϵ'' of the dielectric function of gold. Data measured by Johnson and Christy [59] (solid curves) and a fit of the Drude model in equation (2.28) to this data (dashed curves). The used parameters in the model are $\epsilon_\infty = 6.21$, $\omega_p = 13, 4\,\text{PHz}$ and $\Gamma = 0.1\,\text{PHz}$ taken from [32].

2.3.2 Propagating SPPs

The nature and mathematical description of propagating SPPs is derived in the following based on reference [4]. As already stated above, the propagation of an SPP is restricted to a metal-dielectric interface, which is considered to lie in the x-y-plane at $z = 0$ in the following. Without loss of generality, the SPP propagation can be reduced to a one-dimensional (1D) problem, i.e. assuming propagation along the x-direction. Consequently, the involved electromagnetic fields exhibit no dependence on the y-coordinate. The above simplifications can be implemented by the following ansatz for the electric field:

$$\boldsymbol{E}(\boldsymbol{r}) = \boldsymbol{E}(z)e^{i\beta x}, \tag{2.29}$$

where β is the SPP propagation constant or SPP wavevector. This ansatz is equally holding for the magnetic field $\boldsymbol{H}$. Assuming monochromatic harmonic time dependency, both fields must fulfill the Helmholtz equation (2.12), leading to the wave equation

$$\frac{\partial^2 \boldsymbol{E}(z)}{\partial z^2} + (\epsilon_j k_0^2 - \beta^2)\boldsymbol{E}(z) = 0 \quad ; \quad j = 1, 2 \tag{2.30}$$

for the electric and magnetic field. The wave equation has to be fulfilled separately in the dielectric ($j = 1$, $z > 0$) and in the metal ($j = 2$, $z < 0$). Furthermore, the fields have to satisfy the curl equations in (2.9). It can be shown, that a self consistent solution requires a transverse magnetic (TM) polarized solution with only E_x, E_z and H_y being nonzero [4]. For this solution the set of curl equations can be reduced to

$$E_x = -i\frac{1}{\omega\epsilon_0\epsilon_j}\frac{\partial H_y}{\partial z},$$

$$E_z = -\frac{\beta}{\omega\epsilon_0\epsilon_j}H_y. \tag{2.31}$$

The wave equation simplifies to the TM wave equation

$$\frac{\partial^2 H_y(z)}{\partial z^2} + (\epsilon_j k_0^2 - \beta^2)H_y(z) = 0. \tag{2.32}$$

In this case, the ansatz in (2.29) can be further specified for the magnetic field to

$$H_y(\boldsymbol{r}) = A_j e^{i\beta x \mp \alpha_j z}, \tag{2.33}$$

where "$-$" applies in the dielectric ($j = 1$, $z > 0$) and "$+$" applies in the metal ($j = 2$, $z < 0$). The sign convention ensures bound solutions to the interface. The ansatz in (2.33) is a

solution to the wave equation (2.32) with

$$\alpha_j = \sqrt{\beta^2 - \epsilon_j k_0^2} \tag{2.34}$$

determining the evanescent field decay in both media. Inserting equation (2.33) into the equations in (2.31) yields expressions for the electric field components:

$$E_x = \pm i \frac{A_j \alpha_j}{\omega \epsilon_0 \epsilon_j} e^{i\beta x \mp \alpha_j z}$$

$$E_z = -\frac{\beta A_j}{\omega \epsilon_0 \epsilon_j} e^{i\beta x \mp \alpha_j z} \tag{2.35}$$

The continuity of the tangential components H_y and E_x at the metal dielectric interface demands

$$A_1 = A_2 \quad \text{and} \quad \frac{\alpha_2}{\alpha_1} = -\frac{\epsilon_2}{\epsilon_1}. \tag{2.36}$$

The second relation manifests the requirement stated in the beginning that the dielectric function must change its sign at the interface. This enables simultaneously positive values for α_1 and α_2, to ensure the exponential decay of the fields in both directions perpendicular to the interface as a prerequisite for a confined surface wave. Combining the second equation of (2.36) and equation (2.34) results in the dispersion relation for SPPs:

$$\beta = k_0 \sqrt{\frac{\epsilon_1 \epsilon_2}{\epsilon_1 + \epsilon_2}} \tag{2.37}$$

In general $\beta = \beta' + i\beta''$ takes complex values. The real part β' determines the SPP wavelength

$$\lambda_{\text{SPP}} = \frac{2\pi}{\beta'} \tag{2.38}$$

and the imaginary part β'' determines the propagation losses, i.e. the propagation length after which the SPP intensity has dropped by a factor of $1/e$:

$$L_{\text{SPP}} = \frac{1}{2\beta''}. \tag{2.39}$$

Figure 2.2 shows a plot of the SPP dispersion relation (2.37) at a gold-vacuum interface. The solid and dashed lines correspond to the metal permittivities ϵ_2 respectively taken from the Johnson and Christy data and the Drude model fit shown in 2.1. The thin gray line displays the dispersion relation $\omega = k_0 c$ of light in vacuum. The dispersion relation resulting from the Drude data (dashed lines) exhibit a resonance at a frequency around $5\,\text{PHz}$. The resonance occurs at the root of the denominator in equation (2.37), where $\epsilon_2 = -\epsilon_1$ i.e. $\epsilon_2 \approx -1$ for the gold vacuum interface. Since the dielectric function of gold (ϵ_2) is a complex number
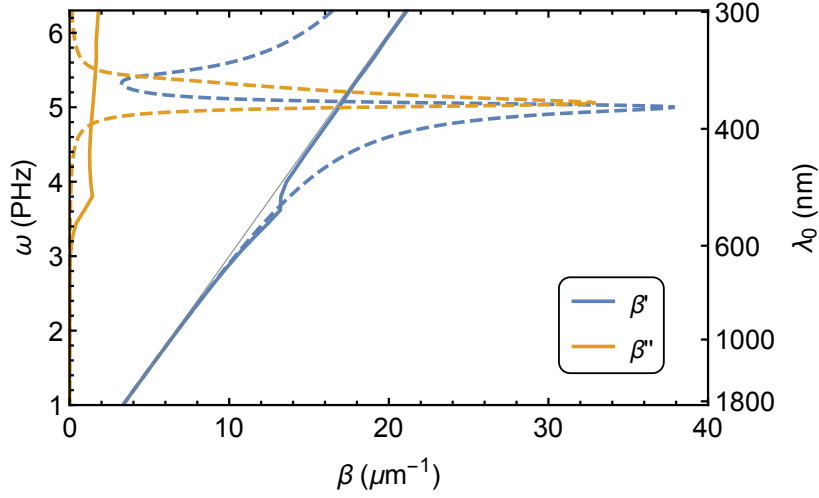
Figure 2.2: Plot of the SPP dispersion relation (2.37) at a gold-vacuum interface. The solid and dashed curves use the respective permittivity data of gold from the solid (Johnson and Christy [59]) and dashed (Drude model fit according to reference [32]) curves shown in figure 2.1.

with a finite imaginary part, the resonance condition can only be approximately fulfilled and β remains a finite number. The dispersion relation resulting from the experimentally determined permittivity data does not exhibit such large β values, because the resonance is damped due to the large imaginary part ϵ_2'' caused by the interband transitions of gold.

2.3.3 Thin film SPPs

In real world experiments and applications, it is often the case that the metal dielectric interface for SPPs is provided by a thin metallic film with sub-100 nm thickness. For such configurations, SPPs can exist on both sides of the metal film at the two metal-dielectric interfaces. For thin enough metal films, the SPPs on both interfaces start to interact and can no longer be treated independently. Omitting the discussion of higher order guided modes with oscillatory behaviour in z-direction, the set of equations given in (2.31) and (2.32) still hold separately in both dielectrics and the metal film. Again, the tangential field components have to be continuous at both interfaces. This system of equations has two bound TM solutions which obey the following thin film SPP dispersion relation [60]:

$$\tanh(\alpha_2 d_z) = -\frac{\epsilon_2 \alpha_2 (\epsilon_1 \alpha_3 + \epsilon_3 \alpha_1)}{\epsilon_1 \epsilon_3 \alpha_2^2 + \epsilon_2^2 \alpha_1 \alpha_2}, \tag{2.40}$$

where the permittivities are ϵ_1 for the superstrate, ϵ_2 for the metal film and ϵ_3 for the substrate and d_z is the thickness of the metal film. The dispersion relation can not be solved explicitly for β. However, for a symmetric dielectric environment, i.e. $\epsilon_3 = \epsilon_1$ it can be explicitly split

15

into two separate dispersion relations [60]:

$$\tanh(\alpha_2 d_z/2) = -\frac{\epsilon_1 \alpha_2}{\epsilon_2 \alpha_1},$$
$$\tanh(\alpha_2 d_z/2) = -\frac{\epsilon_2 \alpha_1}{\epsilon_1 \alpha_2}. \tag{2.41}$$

In particular, this means that the single interface SPP dispersion splits up into two dispersion branches described by the two relations in (2.41). For very thick layers, the left hand side of both equations becomes 1, and the two relations are identical with the second relation in (2.36) for the single interface. In contrast for very thin films, the relations in (2.41) behave very differently. Taking the limit $d_z \to 0$ in the first relation leads to $\alpha_2 \ll \alpha_1$. Thus, the exponential field decay away from the interfaces is much stronger in the dielectric than in the metal. Consequently the major fraction of the electromagnetic fields is concentrated in the lossy metal film leading to a high imaginary part of this dispersion branch. This causes higher propagation losses and therefore this branch is called the short range SPP mode. The behaviour of this branch for three different film thicknesses is clarified by the blue curves in figure 2.3. The lighter the color, the thinner the assumed thickness of the metal film. The
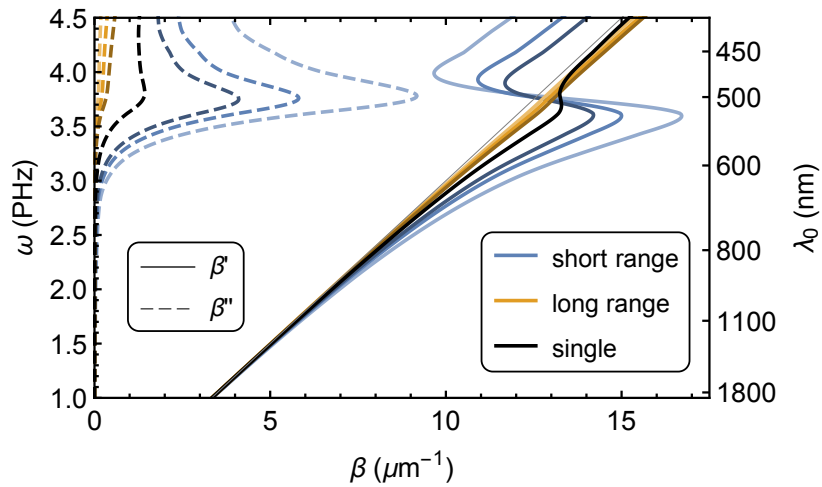
Figure 2.3: SPP dispersion relation of a thin gold film (dielectric data from [59]) surrounded by vacuum according to the relations in (2.41). Blue curves: short range mode (first equation). Brown curves: Long range mode (second equation). The different lightness of the colors correspond to different film thicknesses: 30 nm, 40 nm and 50 nm from lighter to darker colors. The black curve reproduces the single interface SPP dispersion, corresponding to the limit $d_z \to \infty$. The solid curves represent the real part and the dashed curves the imaginary part of β.

solid curves represent the real part β' and the dashed curves represent the imaginary part β'' of the propagation constant. The black curves represent the SPP dispersion (2.37) for a single metal-dielectric interface. For frequencies below the resonance, the short range mode exhibits

higher real and imaginary parts of the propagation constant than for the single interface SPP. The thinner the metal film, the larger the deviations from the single interface dispersion.

Taking the limit $d_z \to 0$ in the second relation in (2.41) yields $\alpha_2 \gg \alpha_1$, which means the fields inside the metallic film are strongly suppressed. In this case, most of the mode power resides in the low-loss dielectric surrounding, leading to a small imaginary part of the propagation constant. Therefore this mode is called long range SPP mode. Demanding a finite value for α_2, requires $\alpha_1 \to 0$, which means the mode more and more spreads in the complete dielectric environment as the film thickness becomes very small. The behaviour of the long range mode is displayed by the brown curves shown in figure 2.3. For thinner films, the real part of the propagation constant approaches the light line and the imaginary part goes to zero i.e. the complex propagation constant tends to the wavevector in the dielectric ($\beta \to k_0$ for vacuum). Ultimately, for $d_z = 0$ this corresponds to a propagating plane wave in x-direction.

2.3.4 SPP excitation and detection

Apparently, for all dispersion relations shown in figures 2.2 and 2.3, the condition $\beta' > k_0$ is always fulfilled below the SPP resonance. In other words, the dispersion relation always lies on the right hand side of light line (thin gray line) in the dispersion plots. As a consequence, SPPs can not couple to propagating plane waves, i.e. they can neither be excited from incident plane waves nor radiate their power into plane waves propagating away from the interface. In terms of the Fourier optics approach discussed in the previous section, the SPP couples to the components of the angular spectrum with $\beta' = k_x$. This requires $k_x > k_0$, which is only possible for evanescent waves. Thus, in order to excite SPPs, evanescent wave components have to be provided in the near-field region of the metal-dielectric interface. There are a few possibilities to generate the evanescent waves needed for the SPP excitation. For instance, structures of subwavelength size at the metal-dielectric interface can efficiently provide components of the angular spectrum with $q > k_0$. Thereby, it is already sufficient to have a structure, which has a subwavelength size only in one lateral dimension, like a groove in the metal, which is extended in y-direction but of subwavelength width in x-direction, or an edge of a finite metal film along y-direction. Upon plane wave illumination from the far-field, these structures provide high k_x components at the surface, including also components with $k_x = \beta$, leading to SPPs propagating in x-direction away from the groove or edge. This effect can be observed for example in the near-field measurements in chapter 6. Instead, a subwavelength sized particle or hole can launch SPPs towards all in-plane directions, which radially propagate away from the excitation. The same effect can also be achieved by approaching a sharp tip with subwavelength apex dimensions into the near-field region of the metal film, which is realized in scanning near-field optical microscopy described in section 4.2. A very efficient and well-defined way to excite SPPs can be realized by a grating structure, whose period p is chosen such that $\beta = 2\pi/p$, leading to a phase matched SPP excitation at each lattice site upon perpendicular plane wave illumination. This effect is discussed in further detail in chapter 5, where it is employed to excite SPPs via an array

of holes in thin gold films. Other configurations for SPP excitation, which are less relevant for this thesis are the so-called Otto and Kretschmann configurations, where the required in-plane momentum $k_x > k_0$ is provided by plane wave propagation through a higher index medium [5].

In general, all arrangements for SPP excitation discussed above apply similarly in opposite direction, i.e. they can scatter an impinging SPP wave at the interface into propagating plane waves. This opens up possibilities to investigate SPPs from the far-field e.g. via leakage radiation microscopy [61, 62] or scanning near-field optical microscopy. The latter technique represents a central aspect of this thesis and is extensively elaborated in section 4.2 as a general near-field imaging technique and especially as a tool for SPP visualization.

The excitation and detection methods discussed so far rely on an energy exchange between the SPP and freely propagating light. Alternatively, SPPs can also be excited by electrons. A fast traversing electron can provide a small fraction of its kinetic energy and momentum to excite an SPP at a suitable interface. Consequently, a focused electron beam can act as an efficient white light source for SPPs. Statistical analysis of the energy distribution of the transmitted electrons can provide information about the excited SPP modes. This technique is called electron energy-loss spectroscopy and is elaborated in section 4.1.

2.3.5 Plasmonic waveguides and localized SPPs

To this point, the understanding of freely propagating SPPs at two-dimensional 2D interfaces has been elaborated. Thereby the propagation direction has been arbitrarily chosen to be parallel to the x-direction. In general, SPPs are free to propagate in any direction parallel to the metal-dielectric interface. Imposing an additional confinement in the x-y-plane by e.g. by an appropriate manipulation of an otherwise homogeneous metal film can lead to a further restriction of the propagation to one dimension. Such configurations, which support bound propagating SPP modes are commonly considered as plasmonic waveguides. In general, an increased confinement is accompanied by an increase of the propagation constant. An example for this behaviour is already given by the thin film SPPs discussed above. The confinement in z-direction perpendicular to the interface is increased and decreased for the short range and long range mode, respectively compared to the single interface SPPs, which is accompanied by an increase and decrease of the propagation constant β. Thereby the increase of β combines two effects: The increase of β' leads to a shorter wavelength of the SPP mode and simultaneously, the increase of β'' manifests the higher propagation losses that occur as a larger fraction of the electromagnetic field intensity is concentrated in the metal. In this context, the dispersion depends not only on the excitation frequency but also on the film thickness d_z. The same holds for the guided SPPs in a 1D plasmonic waveguide. The dispersion is critically dependent on the details of the structural modifications applied to the metal dielectric interface to define the waveguide. Utilizing these insights, the dispersion of a plasmonic waveguide i.e. the mode confinement and the propagation losses can be tailored to a certain degree to match the application needs. In this context, various plasmonic waveguide geometries have been proposed and studied experimentally in literature, e.g. metal

nanowires [6, 8, 63, 64], metal stripes [7, 65], arrays of metallic nanoparticles [66, 67] , v-shaped grooves in metal films [9, 68] and PSWs [20, 69–71]. The properties of the latter are extensively investigated via s-SNOM near-field measurements in chapter 6. The subwavelength confinement achievable in plasmonic waveguides makes them favorable with respect to dielectric waveguides for applications, requiring a tight lateral field confinement, e.g. integrated nanophotonic circuits or nanoscale quantum optics [1]. In the context of nanophotonic circuits, plasmonic waveguides were already applied to realize nanolasers [72], modulators [10], directional couplers [71, 73] and integrated detectors [71]. For application in nanoscale quantum optics, one exploits the enhancement of the local electromagnetic density of states provided by plasmonic waveguides in the region of high field confinement for an efficient coupling to quantum emitters. [8, 16, 74].

The SPP propagation can also be restricted in all three dimensions, e.g. for a subwavelength metallic nanoparticle. These plasmonic nanostructures can be considered as plasmonic resonators. A simple and probably most widely used example is the plasmonic rod antenna [5]. It corresponds to a plasmonic nanowire waveguide shortened to a length $l = \lambda_{\text{SPP}}/2$, which is half of the propagation wavelength of its guided mode. Excitation of the antenna with linearly polarized light along the long axis l results in a resonant oscillation of the SPP on the rod antenna, which can be considered as a localized surface plasmon polariton (LSPP). The rod antenna is the plasmonic equivalent to a half wave antenna in the radio frequency regime. Due to the strong dispersion of the SPPs upon high confinement when approaching the visible spectral range (c.f. short range mode of the thin film dispersion in figure 2.3), the plasmon wavelength can be significantly shorter than the free space wavelength. Thus, the resonant antenna length significantly deceeds $\lambda_0/2$ known for radio frequency antennas [5]. In the near-field region of a plasmonic nanostructure on resonance, strong hot spots can evolve, which facilitate very high field enhancements. This distinguishes SPP resonators from conventional dielectric cavity resonators. For SPP resonators the high optical density of states results from the extreme field enhancement in the hotspot areas, i.e. a very small mode volume, while for cavity resonators, the high density of states is mostly achieved by the high quality factor, i.e. a large number of optical cycles inside the resonator. The strong near-field hotspots at SPP resonators and the large scattering coefficient of plasmonic nanostructures among irradiation from the far-field make them attractive for enhancing the coupling to very small emitters like artificial quantum dots [5] or even single molecules, leading to extremely large intensity enhancement factors in chemical sensing applications [11, 12].

Plasmonic nanoparticles in many different shapes have been fabricated and experimentally investigated to match requirements for various applications. Some interesting structures to mention in this context include split ring resonators [18] and V-shaped antennas [19], which find their application in metamaterials and metasurfaces, dimer antennas [75], or chiral plasmonic structures excited by circulary polarized light [71, 76]. Also the void equivalents i.e. a void of the same shape in a homogeneous metal film show a similar behaviour with exchanged roles of the electric and magnetic fields according to Babinet's principle [32, 77]. Some of the plasmonic nanostructures mentioned above exhibit several resonances for different frequencies and polarizations of the excitation.

In this thesis, arrays of plasmonic rod antennas and their void equivalent slot antennas are used for a phasematched excitation of the plasmonic slot waveguides investigated in chapter 6. In chapter 7, LSPPs featured by a randomly structured nanoporous gold film are investigated in the near-field. Furthermore, the apex of the metallic tip utilized for the near-field measurements in this thesis is itself a plasmonic nanostructure featuring LSPPs. In this context, the tip apex can be approximated by a metallic nanosphere, which enables a simple analytic description of the near-field interaction between the tip and the sample (c.f. section 4.2.5).

Fabrication Methods

To guarantee the desired performance of plasmonic nanostructures and waveguides in applications, their fabrication requires high quality metallic films. Due to its long term chemical stability under ambient conditions, gold is used for this purpose in most cases. This chapter presents two fabrication methods for thin solid gold films with either poly-crystalline or single-crystalline structure. Furthermore, an approach for the fabrication of large-scale self-assembled 3D nanoporous gold networks is outlined. Focused ion beam (FIB) milling is introduced as a nanopatterning technique for the fabrication of plasmonic structures from the solid gold films. Lastly, a fabrication method for freestanding structured gold films also based on FIB milling is introduced, which has been exclusively invented for the work presented in chapter 5 and in reference [77].

3.1 Preparation of thin gold films

In this thesis, two different approaches are utilized to prepare thin solid gold films, which are both discussed below. The first approach of thermal evaporation has become the technological standard for the preparation of thin metallic films for the application in plasmonics. The second approach involves chemical synthesis in solution and leads to thin gold single-crystals. Plasmonic nanostructures fabricated from these single-crystalline gold films exhibit superior quality compared to nanostructures made from conventional thermally evaporated gold films, mainly due to the absence of grain boundary scattering during SPP propagation on the single-crystals [23]. The superior quality of the single-crystalline samples for application in linear and nonlinear plasmonics was shown in many works [78–81] and is also revealed by the findings in chapter 6. Furthermore, an approach is presented to fabricate large-scale highly disordered gold structures. The random nature of the resulting nanoporous films support LSPPs distributed among the sample area and a wide range of excitation frequencies from the near-infrared to the visible regime. The strong LSPP resonances at the sample surface make these structures attractive e.g. for chemical sensing applications [13]. The distribution and nature of LSPP "hotspots" is investigated by near-field measurements in chapter 7.

3.1.1 Thermal evaporation

The thermal evaporation process is performed in a high vacuum chamber (*Leybold* Univex 250). A tungsten boat is filled with a few tens of milligrams of gold and mounted on high-current contacts inside the chamber. The adhesion of the gold to glass substrates is increased by a 2 nm thick chromium layer. Therefore a tungsten rod covered with chromium is mounted between another pair of high current contacts beside the gold. The two pairs of contacts enable a subsequent evaporation of the two layers without an intermediate ventilation of the vacuum chamber. The sample is mounted upside down above this arrangement, such that the evaporated materials can deposit during the process. Additionally, a quartz crystal microbalance is mounted above the sources and beside the sample holder in order to determine the deposited layer thicknesses of the evaporated materials. The quartz is driven to oscillations via electrical contacts utilizing the piezoelectric effect. During the deposition process, the mass load on the quartz crystal increases, which slightly changes its resonance frequency. Knowing the mass density of the deposited material, the deposited layer thickness can be inferred from the resonance frequency shift.

Before starting the evaporation process, the chamber is evacuated to an initial pressure below 2×10^{-6} mbar in order to guarantee a pure and high quality film. During the thermal evaporation process the source is heated up by an electrical current of tens of amperes through the tungsten boat or rod, respectively. If necessary, the 2 nm adhesion layer of chromium is deposited with a rate of 1 Å/s, followed by the gold layer of the desired thickness with a rate of 2 Å/s. The deposition rates are regulated by the heating current, which is adjusted by a feedback loop from the measured rate by the quartz crystal. The thermal evaporation process yields poly-crystalline gold films.

3.1.2 Chemical synthesis of single-crystals

The following description is mainly adopted from the related publication in Optics Express [21] and the experimental work was performed by Hans-Joachim Schill during his Bachelor thesis [82]. The single-crystalline gold films are fabricated by chemical synthesis in solution [83]. A mixture of 40 µl of a 0.5 molar aqueous solution of chloroauric acid $HAuCl_4$ and 20 ml ethylene glycol is filled into a polypropylene tube. A glass coverslip, which serves as a substrate for the grown gold crystals is immersed into the solution. The solution is heated up to 90 °C in an oven for 20 h. The thermal energy initiates a three-step chemical reaction in which the $AuCl_4^-$ is reduced stepwise to $AuCl_3^-$, $AuCl_2^-$ and finally atomic gold [84]. Under the given conditions, the gold atoms can form single-crystalline gold flakes with lateral dimensions larger than 100 µm and thicknesses of only a few tens of nanometers.

The glass coverslip is removed from the ethylene glycol solution and immersed in acetone. The remaining ethylene glycol dissolves in the acetone and the flakes detach from the glass coverslip. Subsequently, the flakes are transferred by dropcasting from the acetone solution onto a glass substrate, which is coated with a thin layer of indium tin oxide (ITO). Upon evaporation of the acetone, the flakes tightly attach to the ITO via surface adhesion forces.

The adhesion proves strong enough to permit AFM measurements at the edge. The electrical conductivity of the ITO layer ensures compatibility of the samples with scanning electron/ion microscopy, which is necessary for nanopatterning of the gold flakes via FIB milling described in the next section. Simultaneously, the ITO layer preserves a high optical transparency for near-infrared wavelengths, which is important for the s-SNOM experiments performed on these samples in chapter 6. From the optical transmission images of flake samples in figure 3.1 one can qualitatively distinguish the thickness of the flakes. A black color indicates a flake
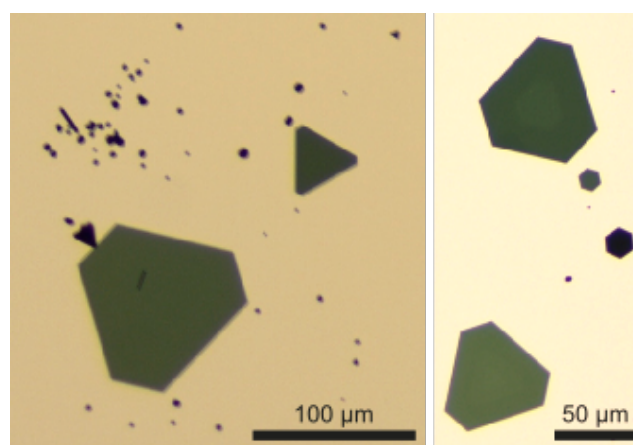

Figure 3.1: Optical transmission microscope images of chemically synthesized single-crystalline gold flakes. Taken from [21].

thickness above 100 nm, for which almost no light is transmitted. The green colored flakes exhibit thicknesses from 30 nm to 70 nm. Typically, flakes with large lateral dimensions of several tens up to 100 μm exhibit a thickness of a few tens of nanometers, whereas flakes with lateral sizes smaller than 10 μm are often thicker than 100 nm. Sufficiently large flakes with lateral dimensions above 50 μm and a suitable thickness of about 50 nm are selected via optical transmission microscopy in combination with AFM for further nanopatterning steps.

3.1.3 Nanoporous gold films

In the following, an approach for the fabrication of scalable self-assembled 3D nanoporous gold networks is outlined based on reference [85]. The elaboration of the experimental expertise for the fabrication method and the processing of all samples were done in close collaboration with Hans-Joachim Schill. The basic principle of this fabrication method is to dealloy composite leaf gold, consisting of gold and silver or other less noble metals. Therefore, the leaf is put onto 68 % nitric acid, which dissolves the metals other than gold from the alloy. After residing on the acid for the desired dealloying time, the exposure can be stopped by transferring the leaf onto distilled water. The leaf is floating on both
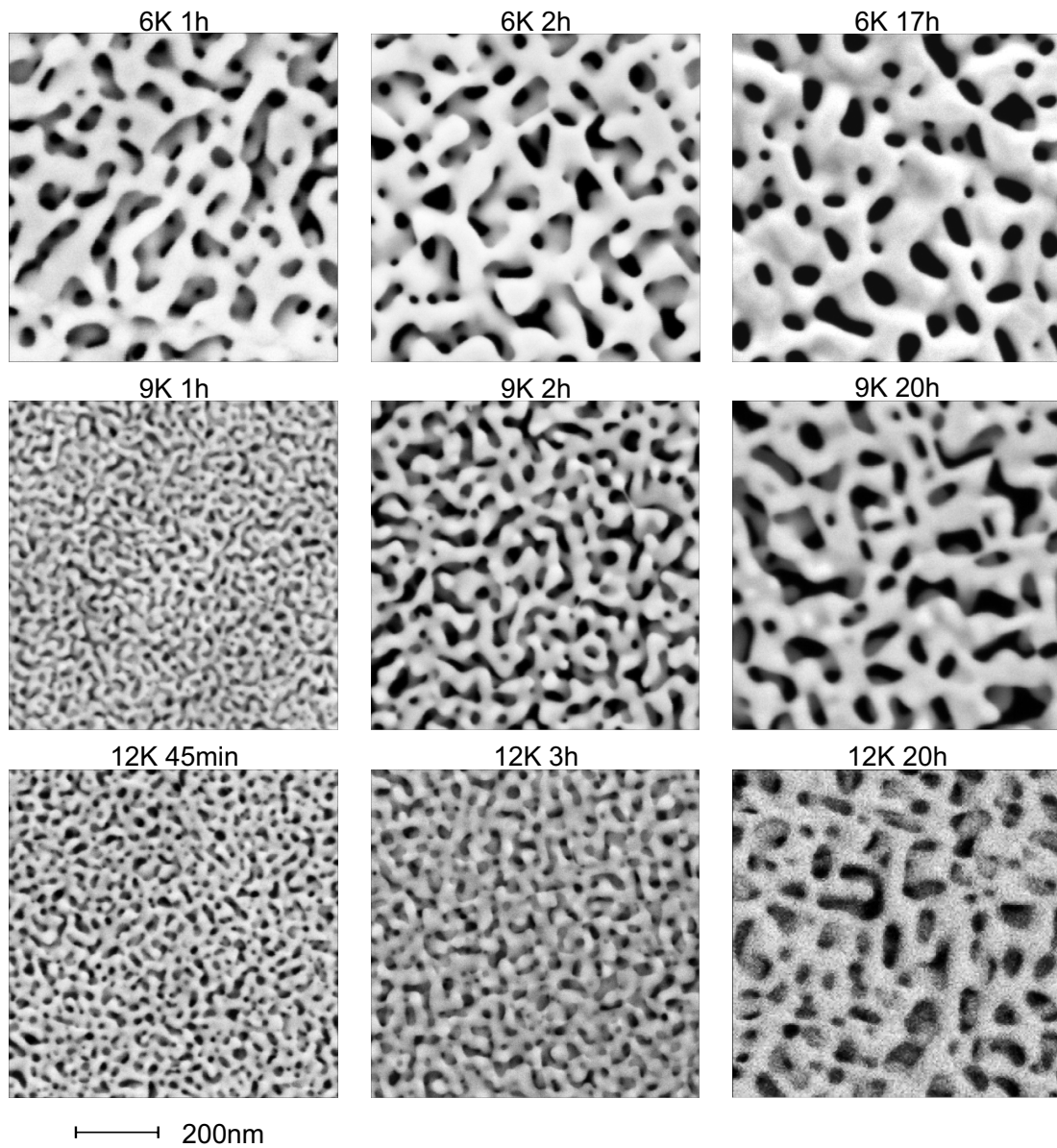
Figure 3.2: SEM images of nanoporous gold films fabricated from composite leafs with different initial gold concentrations (6K: 25 %, 9K: 37.5 % and 12K: 50 %) and different applied dealloying times.

liquids without support due to surface tension. After the dealloying process, the remaining structure is a nanoporous network, which consists mainly of gold. The nanoporous film can be transferred to any desired substrate from the distilled water. The microscopic properties of the gold network, mainly the average pore size, depend on the initial concentration of gold in the composite leaf and the dealloying time. Figure 3.2 shows scanning electron microscopy (SEM) images of nanoporous gold films fabricated from composite leafs with different initial gold concentrations and different applied dealloying times. The first row of images shows the resulting nanoporous films from 6 karat (6K) leafs with 25 % initial gold concentration for different dealloying times. Moderate times of 1 h and 2 h result in comparable pore sizes from several tens up to a few hundreds of nanometers. A long term dealloy process of 17 h further modifies the network and yields smoother pores. Additionally, the film reduces to an almost 2D network due to the large amount of dissolved material. The second row of images in figure 3.2 shows 9K (37.5 % initial gold concentration) leafs after different dealloying times. In this case, the network remains 3D also for long-term experiments. The average pore size shows a very strong dependence on the dealloying time. It is increasing from a few tens of nanometers for a dealloying time of 1 h to a few hundreds of nanometers for 20 h. Also for the 12K (50 % initial gold concentration) sample presented in the last row of images, the pore size is increasing with the dealloying time. However for the 9K film the dealloying time has the largest impact on the average pore size. The effect of the initial gold concentration on the final structure, especially on the average pore size can be observed best in the central column of figure 3.2 for moderate dealloying times between 2 h and 3 h. The average pore size is strongly decreasing with an increasing initial concentration of gold from 6K in the first row to 12K in the bottom row.

3.2 Focused ion beam milling

The nanopatterning of thin gold films in the context of this work is done by FIB milling, also referred to as ion beam lithography (IBL). The employed machine is a *Zeiss* 1540XB Crossbeam microscope. It has both a FIB and a SEM column to allow for an in-situ quality control of the IBL process via the SEM. This is possible due to a special alignment of both columns enclosing an angle of $54°$ with a shared focal point for the electron and ion beam. This so-called eucentric point is located at a working distance of 4.9 mm below the vertically aligned SEM column. The IBL process is taking place under high vacuum conditions at a pressure in the range of 10^{-6} mbar. The FIB microscope utilizes gallium (Ga^{2+}) ions. The gallium source consists of a tungsten needle which is heated up and wetted with gallium. The gallium is liquid at temperatures above $30°$C, which allows this liquid metal ion source to operate at relatively low temperatures. An extractor voltage of -7 kV to -5 kV draws gallium ions from the apex of the needle. The extracted ion current is regulated by a suppressor target to 2 µA. A condensor collimates the extracted ions to a beam of variable current density. The collimated beam is passing an aperture, which can be selected from a set of seven apertures of different sizes depending on the desired ion current throughput. For nanofabrication
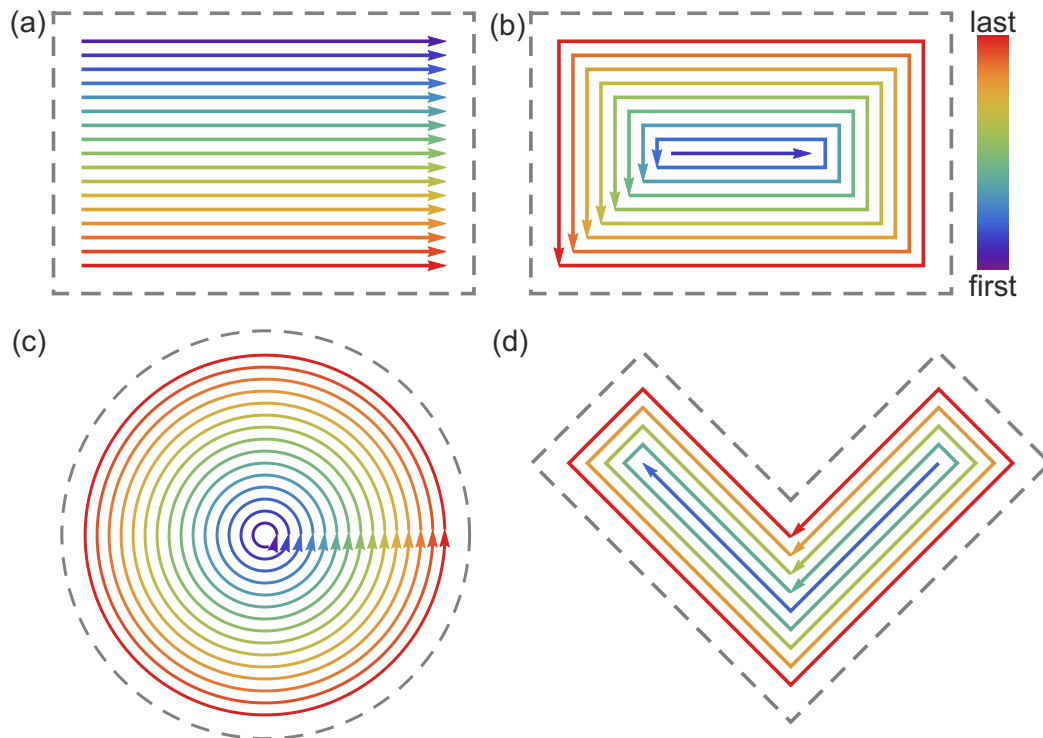
Figure 3.3: Patterning beampaths applied to the ion beam for nanostructuring. The arrows indicate an individual line path and its direction. The colour code indicates the chronological patterning order of the individual line paths. (a) Standard beampath implemented for a rectangular area element by the software. Examples of customized beampaths for optimal patterning results are given for a rectangle (b), circular hole (c) and V-shaped antenna (d).

purposes, only the smallest three available apertures achieve reasonable patterning resolution. These three aperture sizes of $10\,\mu m$, $20\,\mu m$ and $50\,\mu m$ can be used to provide currents of $1\,pA$ to $5\,pA$, $5\,pA$ to $30\,pA$ and $30\,pA$ to $100\,pA$, respectively adjustable by the condensor presets. Behind the aperture, the ions are further accelerated to $30\,kV$ and the ion beam is focused onto the sample. Generally holds, the smaller the current, the finer the focus of the ion beam. Raster-scanning the focused ion beam across the sample surface allows to mill into the material in order to create well defined structures with a resolution down to $20\,nm$. The raster-scan of the ion beam is driven by electrostatic elements, which can be steered together with the beam shutter externally by the software-controlled patterning generator Elphy Plus from *Raith*. Point, line and area patterning elements can be combined in the software in order to create arbitrary nanostructures. Depending on the desired milling depth and material, different point, line and area doses are required. The respective doses are measured in units of pC, pC/cm and pC/cm^2 and are automatically controlled by the software via the scan speed of the beam and the shutter opening time. The dose values have to be recalibrated, whenever the ion beam current is changed. When using predefined area elements like rectangles or circles, the automatic rasterization in the software is accomplished line by line, which leads

to unwanted artefacts at some edges of a structure. However, it turned out that the last written edge is always free from such artefacts. Given this fact, an accumulation of concentric closed loop trajectories for the ion beam writing from inward to outward of the structure yields the optimal result. Both the standard patterning beampath and the optimized patterning beampath are graphically clarified in figure 3.3 (a) and (b), respectively for a rectangular 150 nm × 100 nm structure. The writing direction of single line paths is symbolized by arrows and the chronological writing order of the line paths is encoded by the color. The optimized beampath in combination with a distance of 5 nm between adjacent lines and a line dose of 3 nC/cm to 5 nC/cm for gold films with thicknesses between 40 nm and 60 nm have turned out to result in optimal quality of the nanostructures. Due to the finite size of the ion beam focus, the raster-scanned area of the beampath must be designed smaller than the actual size of the structure in reality. For small beam currents below 10 pA, a margin of 10 nm corresponding to a beam diameter of 20 nm and for larger beam currents of 50 pA a margin of 20 nm must be applied. The real size of the structures for a 10 nm margin are depicted as grey dashed rectangles in the beampath plots in figure 3.3. The approach of concentric trajectories for the optimized beampath can also be applied to other structures, e.g. to the circular holes or V-shaped antennas (c.f. Figure 3.3 (c),(d)) as utilized in the next section.

3.3 Freestanding structured thin films

During the research for this thesis, a special procedure has been developed to fabricate freestanding thin structured metallic films for plasmonic applications. The freestanding nature of the resulting sample has some specific features and advantages. For instance freestanding films are perfectly suited for EELS (c.f. section 4.1), which requires electron transparent samples. The freestanding samples eliminate any additional barrier for the electrons caused by conventional supporting films like thin silicon nitrite (SiN) membranes or carbon films. Another feature is the symmetric environment of the refractive index distribution around the plasmonic structure, which might be an interesting case to study for some sample systems. The freestanding films can also be very useful in combination with the concept of metasurfaces. A metasurface is a quasi 2D arrangement of subwavelength structures, so-called metaatoms, to manipulate the phasefront of a reflected or transmitted light wave. The freestanding nature of the metasurface allow for ultraflat optics which may be combined to multifunctional layer stacks or be transferred to substrates, which do not allow for standard lithography processes, e.g. curved surfaces. Different methods for the fabrication of freestanding films have already been shown in literature like cold-rolling of silver [86, 87], or transferring the film from a solution onto a supporting grid [88]. In this work, a highly reproducible three-step method is applied to fabricate freestanding perforated metal films of different thicknesses down to 20 nm. The method description is partly identical to the related publication [77].

The fabrication process of the freestanding sample starts with a Cu 200 mesh carbon grid from *Quantifoil Micro Tools GmbH* for application in transmission electron microscopy (TEM). It consists of a 15 nm thick carbon film supported by a copper grid with windows of
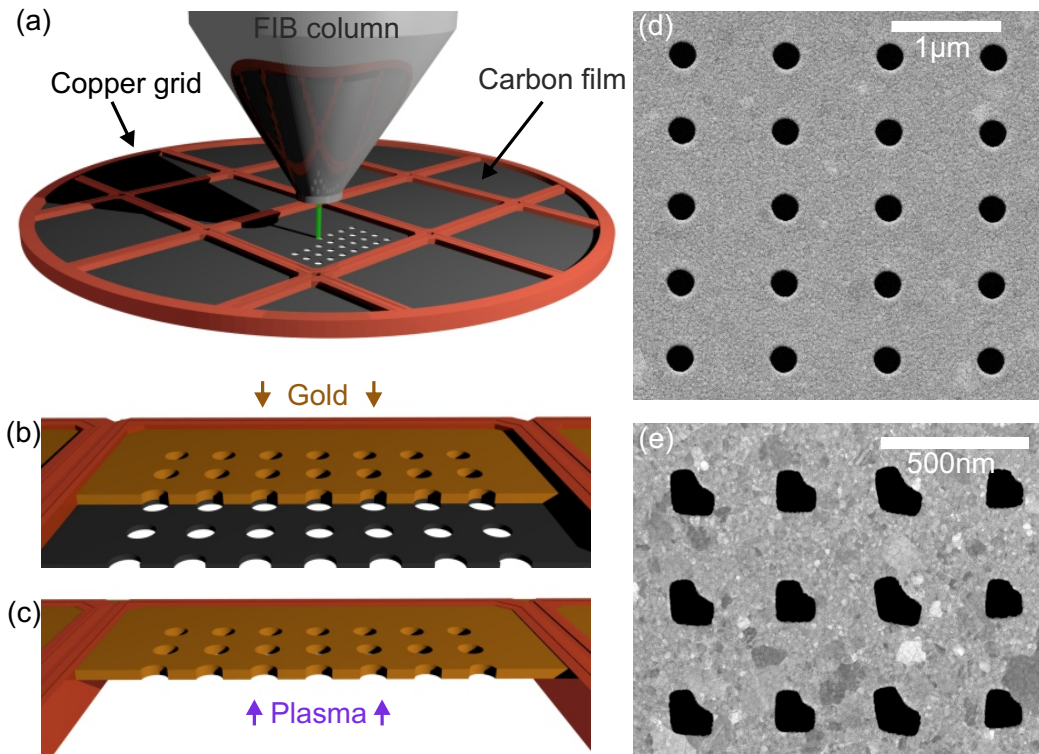
Figure 3.4: Fabrication process of freestanding perforated gold films: (a) Patterning of a carbon TEM-grid via FIB milling. (b) Thermal evaporation of gold to metallize the structures. (c) Removal of the carbon film by a plasma asching process. (d) SEM viewgraph of a hole array in a freestanding gold film. (e) TEM viewgraph of a freestanding metasurface consisting of V-shaped nanovoids. Parts of this figure are also published in the related publication [77].

about $120\,\mu m \times 120\,\mu m$. The carbon film is patterned by FIB milling as desired (see figure 3.4). Afterwards, the structured carbon film template is metallized by thermal evaporation of gold with a deposition rate of $2\,\text{Å/s}$. The minimum achievable film thickness for a stable film is about $20\,\text{nm}$. As a last step, the carbon film is removed by a plasma asching process with an 80:20 Argon-Oxygen gas compound for $420\,\text{s}$ at a pressure of $2.6\,\mu bar$ utilizing a Model 1020 Plasma Cleaner machine from *Fischione Instruments*. The fabrication method described above has been used to fabricate two different sample systems. The first one consists of an asymmetric circular hole array with $800\,\text{nm}$ period in horizontal direction and $600\,\text{nm}$ period in vertical direction. The hole diameter is about $200\,\text{nm}$ and the film thicknesses range from $22\,\text{nm}$ to $74\,\text{nm}$. Figure 3.4 (d) shows a SEM image of such a sample after all fabrication steps. The hole array shows an extraordinary high optical transmission due to an interaction of the incident light with plasmonic eigenmodes of the array. An extensive study of these samples is presented in chapter 5 utilizing EELS for their near-field characterization complemented with far-field optical transmission spectroscopy. The array consists of 100×100 holes to exclude edge effects during the optical transmission spectroscopy.

The second freestanding sample system is a plasmonic metasurface consisting of V- or rod-shaped nanovoids in a 40 nm thick gold film (see fig. 3.4 (e)). In this freestanding metasurface, each metaatom, represented by a nanovoid can be considered as a scatterer. In this manner, each metaatom acts as a source of light upon plane wave illumination from the input side. The interference of the scattered light from all metaatoms form the wavefront on the output side. A well defined geometry of each single meataatom imposes an individual phase shift to the scattered light, which can be used to shape the scattered phasefront in an arbitrary manner. The metasurfaces fabricated here have the functionality to transform a Gaussian input beam into a first order Laguerre-Gaussian Beam, with a doughnut-shaped beam profile. This functionality is realized both for linearly and circularly polarized input waves via V-shaped and rectangular-shaped nanovoids as metaatoms, respectively. For the V-shaped nanovoids the phase shift is controlled by tuning two plasmonic eigenmode frequencies of the antennas with respect to the design wavelength by altering the antenna geometry, i.e. the opening angle and the arm length [19]. The off-resonant rectangular-shaped nanovoids apply the so-called Pancharatnam-Berry phase to the scattered field, which can be steered individually by the azimuthal rotation angle of a rectangular nanovoid [89]. In both cases the transformation to the Laguerre Gaussian mode is occurring in an orthogonally polarized beam with respect to the input, i.e. a beam of perpendicular linear polarization or opposite helicity. A detailed optical characterization of the freestanding metasurfaces presented here is already published in the related work in reference [77].

Experimental near-field imaging techniques

Due to the diffraction limit, already introduced in the context of Fourier optics in section 2.2, the resolution of conventional far-field microscopy is limited to about half of the light wavelength. Information about finer details of the sample are gradually lost during light propagation from the near-field to the far-field regime. Anyway, some sophisticated techniques are available for experimental near-field characterization. These techniques rely on near-field probes which are much smaller than the free space wavelength λ_0 connected to the optical frequency of interest for the investigation of the sample. The probes are brought in very close proximity to the sample within the near-field regime, i.e. to distances much smaller than λ_0. This enables a near-field interaction between the probe and the sample via evanescent waves. In this case, the imaging resolution of the measurements is no longer limited by diffraction, but by the size and distance of the near-field probe. Near-field probes can be for example tapered fiber tips with a subwavelength aperture at the end, sharp light-scattering tips with subwavelength apex dimensions or focused electron beams.

The tip-type probes can be used in combination with SNOM [29, 30], which utilizes AFM [26] to bring the probing tip in close contact to the sample. Illumination of this arrangement by an external light source entails a near-field interaction between tip apex and the sample. When using a fiber tip, this technique is commonly referred to as aperture-type SNOM (a-SNOM) [90], where a subwavelength aperture at the tip end provides a local excitation/detection area for the near-fields above the sample, accessible through the fiber. The lateral resolution of this method is typically determined by the diameter of the aperture. However, it is not possible to reach arbitrary resolution by shrinking the size of the aperture, because the transmittance of light through a subwavelength aperture with diameter d is decreasing proportional to d^4/λ_0^4 [91], which limits the resolution to about $\lambda_0/10$ while preserving a reasonable signal-to-noise ratio [5].

In contrast, when using SNOM in combination with a sharp light-scattering tip, the so-called scattering-type SNOM (s-SNOM) [29, 47], the achievable resolution is determined

by the radius of curvature at the apex of the tip. In most cases metallized silicon tips are used, which typically enable a lateral resolution of about 25 nm. The metallic coating of the tip serves two purposes at once: Firstly, it drastically enhances the scattering efficiency of the tip. Secondly, the tip itself can act as a strong near-field source upon illumination with light polarized along the long axis of the tip due to the lightning rod effect [5]. However the major obstacle in s-SNOM are huge background contributions by direct scattering from the tip and the sample, which overlay the scattered signal of interest originating only from the near-field interaction between the tip apex and the sample. The s-SNOM technique and the methods for the extraction of a background-free complex near-field signal are discussed in more detail in section 4.2 and are used for the measurements discussed in chapters 5, 6 and 7.

As mentioned in the beginning, a focused electron beam is another possible near-field probe. A fast moving electron is surrounded by a highly localized evanescent electric field with lateral dimensions comparable or even smaller than the tip-type probes [92]. The evanescent field may interact with the sample, while the electron is passing by or being absorbed, thereby exciting optical modes of the sample. More precisely, the probability of the optical electron-sample interaction is related to the local density of states (LDOS) of photons in the interaction volume. The LDOS is in turn related to the strength of the electric near-fields of the excited optical mode [92, 93]. The interaction probability can be probed indirectly by measuring either the luminescence from the sample, utilized in cathodoluminescence spectroscopy [33], or measuring the energy-loss of electrons transmitted through the sample. The latter is used in EELS in combination with scanning transmission electron microscopy (STEM) and is restricted to electron transparent samples. The STEM-EELS approach is discussed in more detail in the next section 4.1 and utilized for near-field measurements on periodic hole arrays in freestanding gold films in chapter 5 and on nanoporous gold films in chapter 7.

4.1 Electron energy-loss spectroscopy

As already introduced above, EELS relies on the interaction of a fast electron with a nanostructure via evanescent near-fields. When passing a metallic structure, the electron can excite a plasmonic mode (c.f. Figure 4.1 (a)). The induced electric field E_{ind} of the plasmonic mode acts back on the electron decelerating it and thus causing a loss of kinetic energy. The energy-loss of the electron corresponds to the eigenenergy of the excited mode in the nanostructure. The probability of such an event is called electron energy-loss probability (EELP) and is proportional to the electromagnetic LDOS of the excited mode [93, 94]. Ultimately, the EELP for a certain energy-loss $\hbar\omega$, denoted as $\Gamma(\omega)$, is related to the electric near-field component of the excited mode along the electron beam trajectory [92, 95]:

$$\Gamma(\omega) = \frac{e}{\pi\hbar\omega} \int \text{Re}[e^{-i\omega t} \boldsymbol{v}_{\text{e}} \cdot \boldsymbol{E}_{\text{ind}}(\boldsymbol{r}_{\text{e}}(t), \omega)] \mathrm{d}t. \tag{4.1}$$
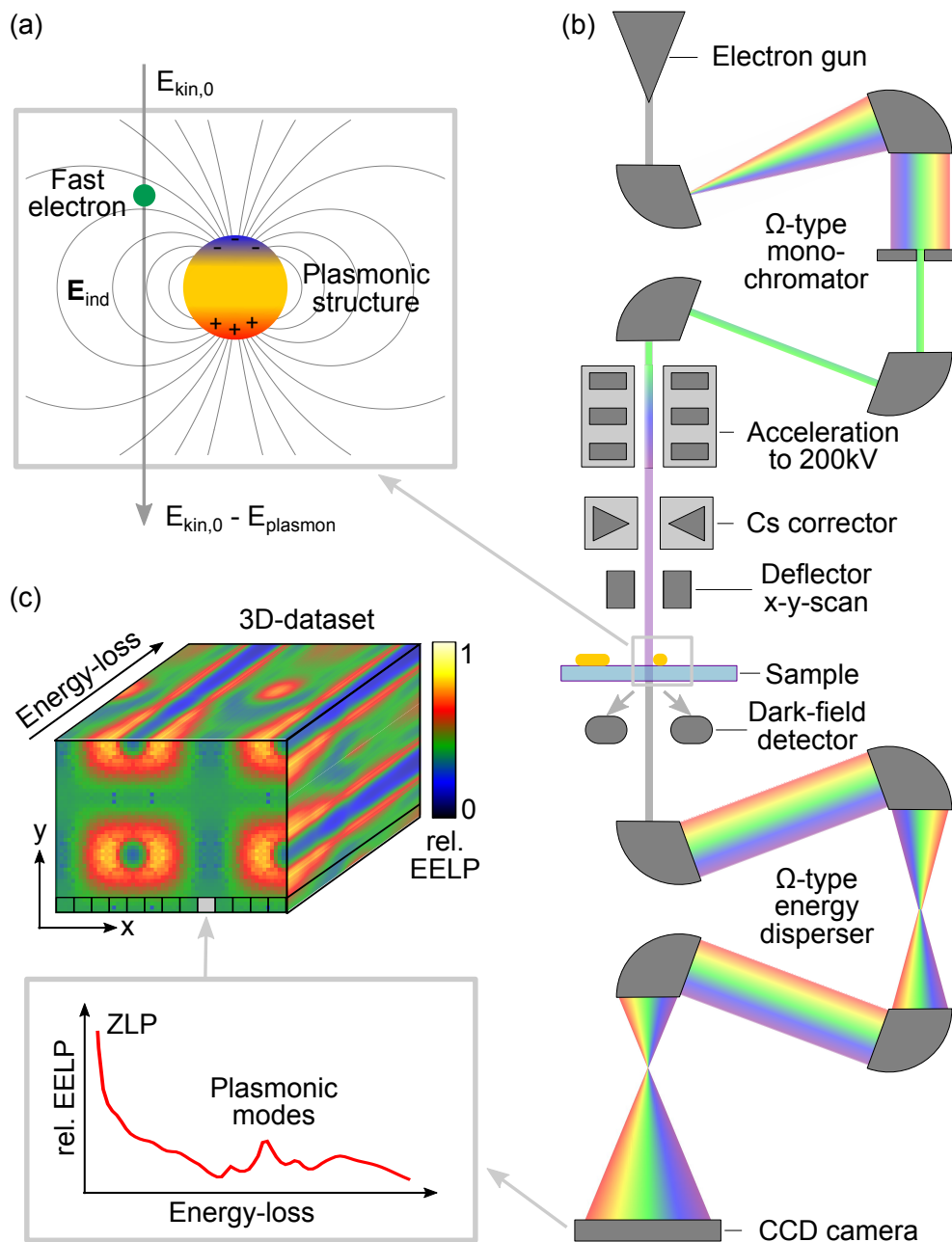
Figure 4.1: (a) Schematic illustration of the interaction between a fast electron and a plasmonic nanostructure. (b) Scheme of the EELS setup following the electron beam trajectory from its generation (top) to the final spectroscopic detection of the transmitted electrons (bottom). (c) Example for a resulting 3D EELS dataset (Simulated data from section 5.2.3). It consists of slices of equal energy-loss with spatial x,y coordinates of the sample plane. Each pixel of this plane is part of an energy spectrum. The spectral coordinate corresponds to the depth of the dataset.

Here, v_e and r_e are the velocity and position of the electron, respectively and E_{ind} is the induced near-field of the nanostructure. According to this expression, the statistical energy distribution of an electron beam traversing the sample results from the contribution of different optical modes and their near-field components along the electron trajectory. Therefore, the spectroscopic analysis of the transmitted electrons i.e. recording a so-called electron energy-loss (EEL) spectrum enables an analysis of the photonic modes of the sample. Raster-scanning the electron beam across the sample and recording EEL spectra in each pixel allows for a spatio-spectral characterization of the vertical near-field distributions of the plasmonic modes [32].

A realization of such an experiment can be achieved by the means of STEM in combination with an energy filter and an electron spectrometer. The STEM-EELS experiments in this thesis are conducted with a *Zeiss* Libra200 MC Cs-STEM, which is presented in a simplified scheme in figure 4.1 (b). The electrons are provided by a thermally assisted Schottky-type field emission gun, in which the electrons are extracted from the apex of a tungsten tip. The tip is heated up to 1300 K and the extraction voltage is set between 3.8 kV and 4.5 kV. The energy distribution of the extracted electrons is narrowed by a second-order aberration corrected Ω-type monochromator [96]. The "Ω" geometry of the beampath in the filter has a symmetry plane, where a dispersed image of the source is formed. The rainbow colors in figure 4.1 (b) denote the energy distribution of the electrons. Inserting a slit in the symmetry plane of the monochromator allows for energy filtering of the transmitted electron beam. Slits of different width enable an optimization between the energy resolution and the beam current. The energy filtering serves two purposes at once: Firstly, it reduces the chromatic aberrations in the electron optics. Secondly, the energy filtering is indispensable for the low-loss EELS experiments employed in this work. The smallest slit size of 0.5 μm results in an energy resolution of 100 meV to 150 meV, which is given by the width of the so-called zero-loss peak (ZLP). The ZLP contains all electrons passing the sample without any interaction and thus reveals the energy distribution of the original electron beam. After monochromation, the electrons are accelerated to 200 keV. Like conventional lenses used in optics, also electron optics, i.e. magnetic lenses suffer from aberrations. Before the electron beam is focused to the sample via a magnetic lens, the spherical aberrations are corrected by a so-called C_s corrector. A more detailed description of this technique can be found in [96, 97]. The focused beam can be raster-scanned across the sample by magnetic beam deflectors.

After passing the sample, the electrons are detected in two different ways depending on the type of interaction with the sample. Electrons, which are scattered from the sample at wide angles can be detected by a ring-shaped dark field detector. These electrons primarily originate from Rutherford scattering at the atomic cores in the sample and thus the contrast depends on the core mass of the material. The transmitted electrons, which preserved the initial beam direction pass an Ω-type electron spectrometer, which consists of four magnetic prisms. The dispersed electron beam hits an electron sensitive 2k × 2k pixel camera (*Gatan*, Ultrascan 1000), which can acquire a whole spectrum at once. The energy resolution of the spectrometer in combination with the camera is 16 meV/pixel. An example of an acquired spectrum at one position of the sample is shown in the lower part of figure 4.1 (c). For

a sufficiently large number of detected electrons, the counts measured by the camera are proportional to the EELP. The majority of all detected electrons are contained in the ZLP, which is located on the left side of the spectrum and is several orders of magnitude out of the scale. The low-loss region from 1 eV to a few eV contains the excitations of plasmonic modes in the sample, corresponding to the optical spectrum from the near-infrared to the near-ultraviolet regime. The higher loss-region with energy losses of several tens to thousands of electronvolts is determined by electronic excitations in the atomic shells. Characteristic absorption edges can be used to distinguish between different materials on the sample from the EEL spectra [98]. However, this work is focused on utilizing EELS for visualizing the near-fields at plasmonic nanostructures.

A consecutive acquisition of spectra during an x-y-scan across the sample yields a 3D dataset, containing a whole spectrum in each lateral pixel. An example for such a 3D dataset is shown in the upper part of figure 4.1 (c). It corresponds to the simulated EELS data of four holes in a solid gold film presented in chapter 5. The x-y-plane depicted in the front is referred to as an EELS map and is represented by a slice through the data at a certain energy-loss, in this case 1.36 eV. The EELS map reveals the 2D distribution of the EELP at a specific energy-loss and is related to the out-of plane electric field component of the excited plasmonic modes. Note that the EELS map contains information of all plasmonic modes of a certain energy at once. Eventually, the EELS map is formed by an overlay of characteristic EELP distributions of several plasmonic modes which have the same, or close eigenenergies with respect to the spectral resolution. Thus the EELS map approximately reveals the interference of the field distributions of the plasmonic modes at a certain energy. Of course there is no exact correspondence between the EELS map and the interference of the out-of-plane near-field components because there is no direct proportionality between the EELP and E_z (c.f. Equation (4.1)).

4.2 Scattering-type scanning near-field optical microscopy

As mentioned before, the s-SNOM technique relies on a sharp scattering tip acting as a near-field probe. Therefore, the tip apex has to be brought in close proximity to the sample. This can be achieved by the means of AFM, as described in the first subsection 4.2.1. The optical excitation of the sample and the detection of the scattered signals resulting from the tip require several optical beampaths built around the AFM. The commercial NeaSNOM system developed by *Neaspec* is a complete system including the AFM and the optical components for illumination and detection. It also includes detectors from external manufacturers. The light sources are not included in the NeaSNOM system in our case. The second subsection 4.2.2 briefly describes the internal detectors and the preparation of the input light for the NeaSNOM from external light sources. The third subsection 4.2.3 elaborates the illumination and detection beampaths of the NeaSNOM and its different operation modes. The scattered light from the arrangement of tip and sample in contact does not only result from the near-field interaction. In fact, the scattered field is dominated by background contributions. An efficient

approach to virtually background-free extraction of the near-field signal is presented in detail in subsection 4.2.4. The last subsection 4.2.5 treats the theoretical background of the near-field interaction between the tip apex and the sample by a simple analytical model. This enables an intuitive understanding of how the measured quantities are connected with the physical quantities of interest, i.e. the evanescent near-field above the sample or the local dielectric constant at the sample surface.

4.2.1 Atomic force microscope

A sketch of the AFM setup is depicted in figure 4.2. The tip is brought in contact with the sample via intermittent contact mode AFM. Commercial tips (Arrow NCPt manufactured by *NanoWorld*) on a cantilever with typical resonance frequencies between 250 kHz and 300 kHz are utilized. The cantilever is driven to oscillations close to its resonance frequency by a piezo actuator. The excitation frequency Ω is typically chosen slightly below the resonance frequency of the cantilever such that the oscillation amplitude is between 80% and 90% of the amplitude on resonance. Typical oscillation amplitudes of the tip are several tens of nanometers. In order to detect the movements during oscillation, the upper side of the cantilever is illuminated by a so-called deflection laser. This arrangement transfers the tiny
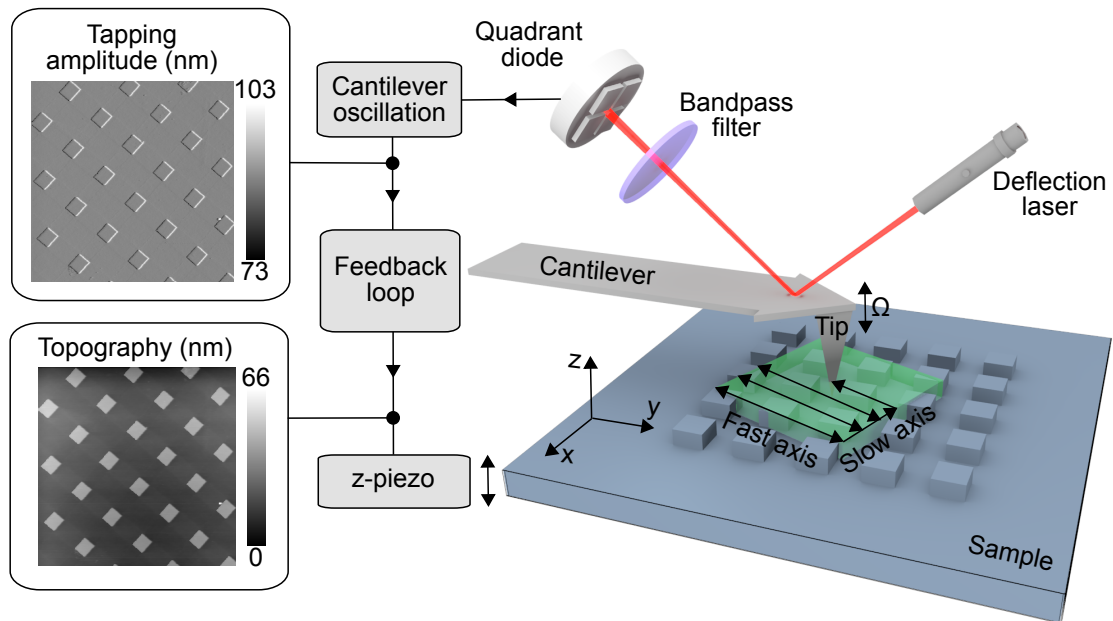

Figure 4.2: Sketch and functionality of the AFM setup. On the right side, the arrangement during an AFM measurement on a calibration sample is depicted including the beam path of the deflection laser. The scan area is highlighted in green. Left, the instances involved for the feedback loop including the output oscillation amplitude and topography from an exemplary measurement on the calibration sample are shown.

oscillations of the cantilever to a macroscopic deflection of the laser beam, which is detected by a quadrant photodiode. The deflection laser has an operating wavelength of 785 nm and is transmitted through a bandpass filter (*Edmund Optics* 785 nm CWL, 12.5 nm Dia., Hard Coated OD 4.0 10 nm Bandpass Filter). The filter has a sharp transmission window between 780 nm and 790 nm, shielding the quadrant diode from disturbing interference with external laser sources used for s-SNOM imaging at other wavelengths.

For very close tip-sample distances, below the free tip oscillation amplitude, the tip is in an intermittent contact with the sample. This means that the tip apex hits the sample at its lower turning point once in each oscillation cycle and the tapping amplitude is constrained by the distance between the sample surface and the neutral position of the tip apex. As a result, the tapping amplitude is altered by variations of the tip-sample distance and can be used as an error signal for a feedback loop. The feedback controls a piezo actuator steering the vertical (z) position of the sample, in order to hold the tip in the intermittent contact. Thereby, the intermittent contact is defined by a setpoint value for the oscillation amplitude, which is typically chosen between 80% and 90% of the free oscillation amplitude without tip-sample interaction. A precise and fast control of the feedback is enabled by a proportional integral differential (PID) regulator. A 2D raster-scan of the sample with respect to the tip reveals the topography of the sample surface, which is encoded in the movements of the z-piezo steering the sample. The lateral movements of the sample are realized by two piezo axes, which have a maximum scanning range of $100\,\mu m \times 100\,\mu m$. All movements are performed by the sample table, which is crucial for s-SNOM applications in order to preserve the alignment of the focusing optics with respect to a fixed position of the tip during the scan.

The raster-scan is performed pixel by pixel on a line in the so-called fast axis direction. The line scans are consecutively stacked in the direction of the slow axis. The scan range and the number of pixels can be chosen for the fast and slow axis independently. The scanning angle, meaning the angle of the fast axis with respect to the x-axis can be chosen arbitrarily in steps of $1°$. In normal scan mode, each line is scanned along the fast axis in both forward and backward direction, yielding a forward and backward 2D dataset for the sample topography and the oscillation amplitude of the tip. Typically applied scan speeds of the tip are about $2\,\mu m/s$. The left two panels in figure 4.2 show an example of recorded amplitude and topography forward scan data from a measurement of a calibration sample with small quadratic pillars of known height. The topography measurement can be used to determine a calibration factor, which converts the steering voltage of the z-piezo into real height values. The amplitude signal can be used to adjust the speed of the feedback regulation. Whenever the tip encounters a topographic feature, the oscillation amplitude deviates from the setpoint value until the feedback regulation stabilizes it back to the setpoint. This effect can be seen in the exemplary measurement data for the amplitude in figure 4.2 at the edges of the quadratic nanopillars. The speed of the feedback, i.e. the parameters of the PID regulation can be optimized, in order to minimize the amplitude deviations in strength as well as in lateral extension.

4.2.2 Sources and detectors

To achieve optimal results from a combination of the NeaSNOM system with an external laser source, the output beam of the latter has to be manipulated to match certain requirements regarding its diameter, collimation, profile and power. In order to achieve this, the laser beam is passing several components on the optical table until finally coupled into the NeaSNOM (c.f. figure 4.3). Firstly, the laser beam passes a combination of a super achromatic half
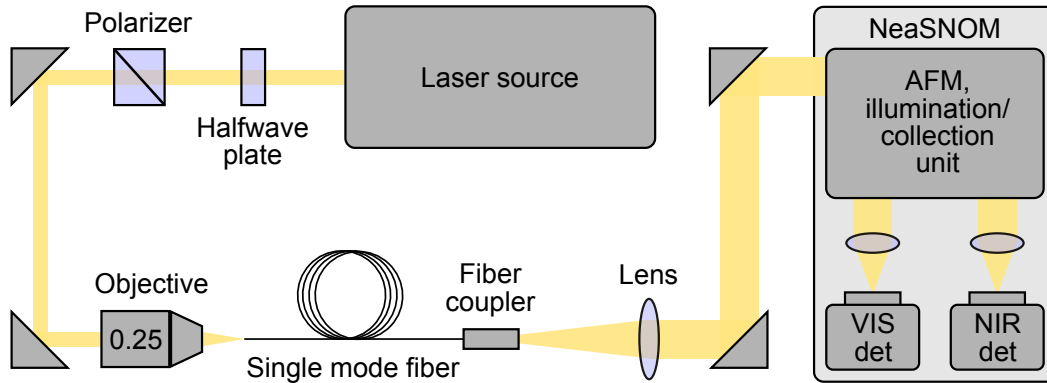

Figure 4.3: Beampath on the optical table to prepare the laser radiation from an external laser source for coupling into the NeaSNOM. The NeaSNOM system itself includes two detectors for the Visible (VIS) and Near-infrared (NIR) wavelength regime.

wave plate (*Thorlabs* SAHWP05M-1700) and a linear polarizer (*Thorlabs* GTH10M), which allows for a continuous attenuation of a linearly polarized laser output. The transmitted polarization is chosen to be perpendicular to the optical table plane. Afterwards, the beam is guided via two adjustable mirrors into a 0.25 NA NIR objective, to couple it into a polarization maintaining single mode fiber (*Thorlabs* P1-1310PM-FC-2). The adjustable mirrors in combination with a 3D micrometer stage mount for the objective allow for very fine adjustments leading to an achievable incoupling ratio of roughly 0.5. The single mode fiber acts as a spatial filter to the transverse modes of the beam, which leads to a perfect Gaussian beam profile at the output. The light is coupled out via a commercially available fiber coupler *Schäfter+Kirchhoff* 60FC-F-0-A18-45, which preserves the Gaussian beam profile. The coupler allows for a collimated output beam with a diameter of 3.3 mm (manufacturer rated after 0.5 m propagation distance). The collimation can be adjusted by a fine tuning screw at the collimator. To achieve a final beam diameter of roughly 8 mm the collimator is adjusted to produce a slightly divergent output beam, which is recollimated by a lens with a focal length of 1000 mm placed at a distance of 0.6 m to the collimator. Careful adjustment of the lens for central beam transmission on the optical axis is necessary to minimize abberations to preserve the Gaussian profile of the beam. Finally, the beam is coupled into the NeaSNOM via two adjustable mirrors. For an easy alignment, the NeaSNOM system includes a visible low-power pilot laser as a reference. Details about the internal s-SNOM setup of the NeaSNOM for the illumination of the AFM tip and the collection of the scattered light are covered in the

next subsection 4.2.3. The NeaSNOM includes two detectors from external manufacturers: *Thorlabs* PDA20CS-EC for detection in the near-infrared (NIR) and *NEW FOCUS* Model 2051 for detection in the visible (VIS). Both detectors are amplified with an adjustable gain. The applied gain is connected to the acquisition speed of the detectors and is optimized to guarantee detection of signals above 1 MHz. This is important for the extraction of the near-field signal via frequency demodulation, as discussed later in section 4.2.4. The setup on the optical table described above can be applied to four laser sources available in the laboratory. The covered wavelength ranges of all four sources and the two detectors are summarized in figure 4.4 in different colors. The resulting combined wavelength range for use
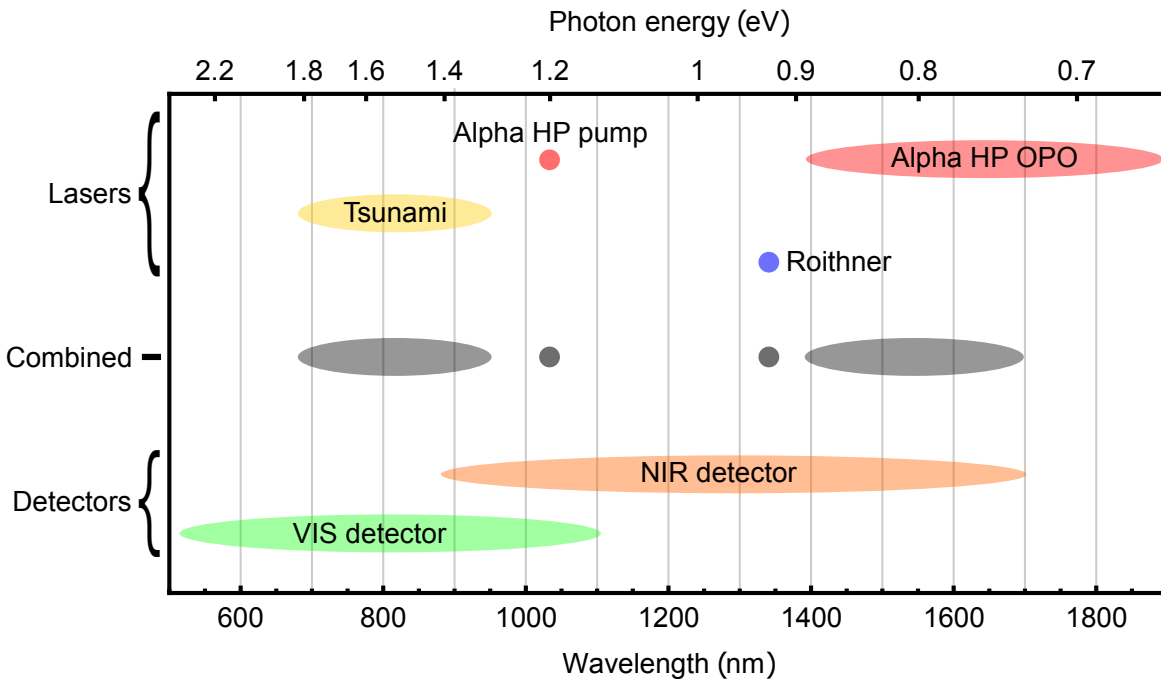

Figure 4.4: Overview of the accessible wavelength ranges for s-SNOM measurements. The output wavelength ranges of the available external laser sources are shown in the upper part. The detectable wavelength ranges of the internal VIS and NIR detectors of the NeaSNOM are shown in the lower part. The resulting combined wavelength regimes are shown in gray in the center.

in the NeaSNOM is shown in gray. The first source is a continuous wave emitting solid state laser RLTMIL-1342-100 from *Roithner Lasers* with an emission wavelength of 1342 nm and an output power of 100 mW. The second source is the Alpha-HP from *Stuttgart Instruments* including an optical parametric oscillator (OPO) pumped by a pulsed laser source utilizing an ytterbium doped potassium gadolinium tungstate (Yb:KGW) crystal [99]. In a nonlinear process, one photon of the pump laser is converted in two output photons with different energies via difference frequency generation. The photons of higher energy contribute to the signal output and the lower energy photons form the idler output. Altering the energy ratio between the signal and idler photons enables wavelength tuning of the two output

beams. The tunable signal output of the OPO has a wavelength dependent output power above 200 mW. The laser pulses have a length of approximately 400 fs in time domain [100, 101] and occur at a repetition rate of 40 MHz. The third source is the Yb:KGW pump of the Alpha-HP system, which can be coupled out separately. It has a wavelength of 1040 nm and a Fourier limited spectral width of roughly 2.5 nm. The last laser source is a Tsunami laser from *Spectra Physics*. It consists of a Ti:Sapphire crystal in a cavity and is pumped externally by a Millennia eV from *Spectra Physics* with a wavelength of 532 nm. Internal mode locking in the Tsunami leads to a pulsed output with a repetition rate of 80 MHz. The cavity includes a prism compressor which allows for adjustments of the pulse length and the spectral width, which are connected via the time-bandwidth product. Typical values for the spectral width range between 3 nm and 15 nm. The Ti:Sapphire crystal provides a broad emission spectrum between roughly 650 nm and 1050 nm. Wavelength selection is realized via a slit in the symmetry plane of the compressor, which enables a tunable output between 680 nm and 900 nm in our case. To use the Tsunami and the pump laser of the Alpha-HP in combination with the optical setup above, the fiber has to be exchanged to P1-1064PM-FC-2 from *Thorlabs* and the coupler is replaced by 60FC-F-0-A11-02 from *Schäfter+Kirchhoff* to cover a range of shorter wavelengths.

4.2.3 The s-SNOM setup

On top of the standard AFM setup described in section 4.2.1, the neaSNOM system provides different optical beam paths in order to illuminate the tip apex with external laser sources and collect scattered radiation from the near-field interaction region of the tip and the sample. A complete sketch of the optical setup is displayed in figure 4.5. Essentially, the system can be operated in reflection mode, represented by the blue beampath and in transmission mode, represented by the red beampath. The purple beampaths are shared for both operation modes. The operation mode of the neaSNOM can be switched by the input switch mirror.

When the neaSNOM is operated in reflection mode, the beam is guided to a beamsplitter, which divides the beam in two arms of a Michelson interferometer. At the end of one arm, the beam is focused onto the tip by the upper parabolic mirror. The focused beam is incident at an inclination angle of about $30°$ with respect to the sample surface in the x-y-plane and at an azimuthal angle of $45°$ with respect to the x-axis. The polarization of the incident laser radiation is p-polarized, containing a large field component along the vertical axis of the tip. Due to the elongated tip shape, this polarization is favourable for a strong direct tip excitation via the lightning rod effect [5]. In this configuration, the tip apex acts as a sharp localized near-field source, which gives rise to a strong near-field interaction between the tip and the sample. Due to this interaction, the radiation scattered by the tip contains information about the local optical properties of the sample, which is further elaborated in 4.2.5. The scattered light is collected by the upper parabolic mirror and takes the reverse excitation beampath back to the beamsplitter. The latter overlays the scattered signal with the reference beam, which is reflected by the end mirror in the other interferometer arm. Afterwards, the reflection mode beampath is reunited with the transmission mode beampath.
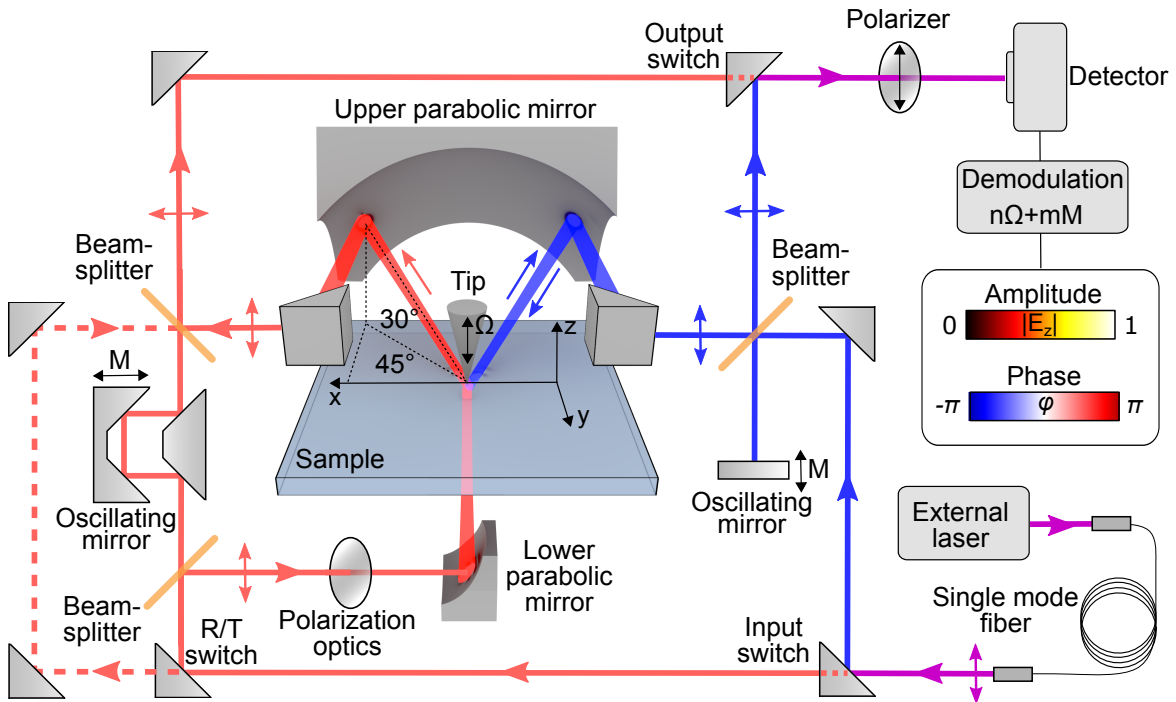
Figure 4.5: Sketch of the s-SNOM setup. The s-SNOM system can be used in reflection and transmission mode. The blue beam path for reflection mode and the red beam path for transmission mode include a Michelson interferometer and a Mach-Zehnder interferometer, respectively. Beam focusing to the probing tip in contact with the sample is realized by parabolic mirrors. The demodulation of the detected signal reveal the amplitude and phase of the near-field above the sample.

The shared beampath is passing a vertically oriented linear polarizer before reaching the detector. Conditioned by the geometric arrangement of the tip and the sample and the elongated tip shape in vertical direction, the scattered light from the near-field interaction is mainly polarized in vertical direction, which is transmitted by the polarizer. Background contributions with a horizontal polarization e.g. by direct scattering from the sample can be eliminated by the polarizer. Further suppression of background contributions can be eliminated by careful demodulation of the detected signal. Therefore, the neaSNOM system implements the so-called pseudoheterodyne detection scheme, in which the end mirror in the Michelson interferometer is driven to oscillate at a frequency of roughly $M = 300\,\text{Hz}$ by a piezo actuator. The tip oscillation frequency Ω and the mirror oscillation frequency M are essential for a background-free extraction of the amplitude- and phase-resolved near-field signal from the scattered light. The background free near-field signal is contained in the side bands of the higher harmonics of the tip oscillation frequency generated by the oscillation of the end mirror. Demodulation for these sidebands at $n\Omega + mM$ ($m \in \mathbb{Z}$, $n \in \mathbb{N}$) yields the near-field amplitude and phase. This signal processing is described more detailed in the next subsection 4.2.4.

When the neaSNOM system is operated in transmission mode configuration, the input switch mirror is shifted, such that the laser beam is guided along the red beampath. By the R/T switch mirror, one can choose between illumination from above via the upper parabolic mirror (red dashed beampath) and illumination from below via the lower parabolic mirror (red solid beampath). The illumination from above is only used for the alignment of the upper parabola in the first place. For the illumination from below, the beam is divided by a beamsplitter in a part that is guided to the lower parabola and a part that constitutes the reference beampath of a Mach-Zehnder interferometer. Before being focused to the sample from below by the lower parabola, the light can pass an optional polarizer. For instance, the incident linear polarization can be rotated or converted to circularly polarized light. Different from reflection mode operation, the vertically incident beam has only in-plane polarization components. Therefore, nanostructures on the sample with large in-plane polarizabilities are primarily excited, rather than the tip itself. The near-field above the excited nanostructures couple to the tip. In analogy to reflection mode operation, the scattered radiation from the tip contains information of the near-field interaction, or more precisely is related to the out of plane near-field component E_z above the sample. This connection is further elaborated in section 4.2.5. The upper parabola turns the scattered light into a collimated beam, which is united with the reference beam and guided to the detector. The reference beam is modulated by an oscillating mirror arrangement at the same frequency M as for reflection mode. The detected signal is processed in the same manner as in reflection mode operation, which is discussed in the following in further detail.

4.2.4 Extraction of the complex near-field signal

The neaSNOM system implements the so-called pseudoheterodyne detection scheme, which allows for an efficient background suppression and simultaneous decoupling of amplitude and phase of the near-field signal. This detection method is based on the investigation of the frequency spectrum of the measured intensity, i.e. the output voltage of the detector.

The near-field interaction between the tip and the sample is limited to a subwavelength volume with lateral dimensions on the order of the tip apex and a vertical dimension of several tens to a few hundreds of nanometers. However, the focused illuminating laser spot has a much larger size of a few micrometers. This gives rise to a large amount of background signal, which overlays the near-field signal. Typical sources of background signal are direct scattering from the tip shaft or from small particles on the sample surface. Also a combination of reflections at the tip shaft and the sample could possibly be collected by the upper parabola directly. In general, the detected intensity resulting from background contributions exceeds the detected intensity resulting from the near-field interaction. Therefore, the pseudoheterodyne detection as an efficient method for background suppression is indispensable for reliable near-field investigations. The following overview of this technique is based on the original work of N. Ocelic. [102, 103]. It starts with the general concept of background suppression in s-SNOM utilizing the fact, that the scattered light resulting from the near-field interaction and the background contributions spread differently among the frequency components $n\Omega$

resulting from the tip oscillations. The second part focuses on the functionality of the pseudoheterodyne detection, which is characterized by an oscillating mirror in the reference beam of the interferometer.

The key feature utilized for background suppression is the oscillation of the tip during intermittent contact AFM operation. Since the typically utilized cantilever oscillation amplitudes of a few tens of nanometers are very small compared to the cantilever length on the order of a hundred micrometers, the restoring forces can be assumed to be linear. Hence, to very good approximation, the cantilever can be treated as a harmonic oscillator, leading to a sinusoidal oscillation with the tapping amplitude Δz, where the tip-sample distance, i.e. the height of the tip apex above the sample surface H can be described by $H(t) = \Delta z[1 + \cos(\Omega t)]$. The scattered light, which results from the tip-sample interaction strongly depends on $H(t)$ and thus exhibits a time dependency modulated by the tip oscillation. The scattered field is related to the incident field by scattering coefficients of the background signal σ_b and the near-field signal σ:

$$E_s(t) = E_i(t)[\sigma(t) + \sigma_b(t)]. \tag{4.2}$$

A complete vectorial description of the problem including tensorial scattering coefficients is omitted here, since the microscopic details of the near-field interaction are not relevant for the general concept of the background suppression. A very simple approach to consider the vector nature of the involved electric fields, especially highlighting the difference between reflection and transmission mode s-SNOM is given in the next section 4.2.5.

The time dependence of the scattered field is on one hand determined by the incident field through $E_i(t) = A(t)e^{i\omega_0 t}$, where $A(t)$ is the pulse envelope of the laser source in time domain, in case of a pulsed source. When a continuous wave source is utilized, one can set $A(t) = 1$. On the other hand, the time dependence due to the tip oscillations, is encoded in the scattering coefficients, which contain frequency components of multiples of Ω and can be separately expanded in Fourier series:

$$\sigma(t) = \sum_{n=0}^{\infty} \sigma_n \cos(n\Omega t), \quad \sigma_b(t) = \sum_{n=0}^{\infty} \sigma_{b,n} \cos(n\Omega t). \tag{4.3}$$

Each frequency component is a complex number constituted from a scattering amplitude and phase:

$$\sigma_n = s_n e^{i\varphi_n}, \quad \sigma_{b,n} = s_{b,n} e^{i\varphi_{b,n}}. \tag{4.4}$$

The detected background intensity, which originates from direct scattering or reflections from the sample only occurs in the DC component $\sigma_{b,0}$. Higher order components of the background contribution $\sigma_{b,n}$ with $n > 0$ must stem from scattering or reflection processes involving the tip. They depend on the change of the field distribution of the incident electric field around the tip E_{tip}. As long as the oscillation amplitude of the tip is significantly smaller than the illumination wavelength ($\Delta z \ll \lambda_0$), the variation of E_{tip} can be linearized in the oscillation range of Δz. In this case, the harmonic time dependency of the tip oscillation is transferred to the background contribution σ_b. An almost harmonic time dependency

of σ_{b} corresponds to a large magnitude of the $\sigma_{\text{b},1}$ and only minor magnitudes of the $\sigma_{\text{b},n}$ components with $n > 1$. Higher harmonic background contributions $\sigma_{\text{b},n}$ possibly arise either from a small error by assuming a linear alteration of $E_{\text{tip}}(H)$ or deviations from a perfect sinusoidal motion of the cantilever e.g. caused by a nonlinear restoring force of the cantilever.

In contrast, the near-field interaction between the tip apex and the sample via evanescent fields is varying strongly nonlinear over the tip oscillation range of $2\Delta z$. The nonlinear dependence of the near-field interaction yields significant values in higher harmonics with $n > 1$ of the scattered near-field signal σ_n. Consequently, a sufficiently high order n_0 features a huge near-field to background ratio $\sigma_{n_0}/\sigma_{\text{b},n_0} \gg 1$, which enables an efficient suppression of the background signal with respect to the near-field signal. The required order n_0 depends on the employed laser wavelength and the tapping amplitude Δz. Shorter wavelengths and higher tapping amplitudes increase the amount of background contributions and demand a higher demodulation order for compensation. Generally holds, the higher the demodulation order, the lower the residual background on the measured near-field signal. Simultaneously, higher demodulation orders yield lower signal-to-noise ratios. Typical experimental values for the tapping amplitude and the demodulation order in the near-infrared wavelength regime are $\Delta z = 60\,\text{nm}$ and $n_0 = 3$ or $n_0 = 4$ at $\lambda_0 = 1600\,\text{nm}$ and $\Delta z = 40\,\text{nm}$ and $n_0 = 4$ or $n_0 = 5$ for $\lambda_0 = 800\,\text{nm}$. With these values, a reasonable agreement of low background contributions and high signal-to-noise ratio can be achieved.

In the interferometric detection scheme, the scattered signal collected by the upper parabola is overlayed with a reference beam. The resulting output voltage $U(t_0)$ of the detector at a certain read-out time t_0 is given by the time average of the incident intensity, which composes of the scattered field E_{s} and the reference field E_{ref}:

$$
\begin{aligned}
U(t_0) \propto \langle I(t) \rangle_{t_0,T} &= \frac{1}{T} \int_{t_0}^{t_0+T} |E_{\text{s}}(t) + E_{\text{ref}}(t)|^2 dt \\
&= \frac{1}{T} \int_{t_0}^{t_0+T} |E_{\text{i}}(t)|^2 dt \cdot |\sigma(t_0) + \sigma_{\text{b}}(t_0) + \sigma_{\text{ref}}|^2 \\
&= \langle I_{\text{i}} \rangle_{t_0,T} \cdot |\sigma(t_0) + \sigma_{\text{b}}(t_0) + \sigma_{\text{ref}}|^2.
\end{aligned}
\tag{4.5}
$$

The integration time span T is related to the data acquisition speed of the detector. For a reasonable signal extraction in combination with a pulsed laser source it should hold $1/(n_{\text{max}}\Omega) \gg T \gg T_{\text{rep}}$. This ensures, the acquisition is fast enough to resolve the higher harmonics of the tip oscillation frequency up to the order n_{max}, but averages out the pulse envelope $A(t)$ of the laser source with repetition rate T_{rep}. For this reason, the scattering coefficients σ and σ_b can be simply evaluated at t_0 instead of applying the time average (c.f. second step in equation (4.5)). The time-averaged incident intensity $\langle I_{\text{i}} \rangle_{t_0,T}$ also depends on the point of time t_0 of the detector read-out to account for instabilities of the incident light e.g. through noise of the laser source at frequencies below $1/T$. The time dependency of the scattering coefficients introduce a modulation of $U(t_0)$ at higher harmonics of the tip tapping

frequency as well. Therefore, also $U(t_0)$ can be expanded in a Fourier series

$$U(t_0) = \sum_{n=0}^{\infty} u_n \cos(n\Omega t_0). \tag{4.6}$$

The frequency components u_n can be found by inserting equations (4.3) and (4.4) together with the complex coefficient $\sigma_{\text{ref}} = s_{\text{ref}} e^{i\varphi_{\text{ref}}} = E_{\text{ref}}/E_{\text{i}}$ relating the reference field to the initial field into equation (4.5). Assuming $s_{\text{b},0}, s_{\text{ref}} \gg s_{\text{b,n}}, s_{\text{n}}$ and $n > 0$, the leading term of a frequency component is given by (c.f. appendix):

$$\begin{aligned} u_n &\propto 2s_{\text{ref}}[s_{\text{b},n}\cos(\varphi_{\text{b},n} - \varphi_{\text{ref}}) + s_n\cos(\varphi_n - \varphi_{\text{ref}})] \\ &+ 2s_{\text{b},0}[s_{\text{b},n}\cos(\varphi_{\text{b},n} - \varphi_{\text{b},0}) + s_n\cos(\varphi_n - \varphi_{\text{b},0})]. \end{aligned} \tag{4.7}$$

When implementing a non-interferometric detection ($s_{\text{ref}} = 0$), but choosing $n \geq n_0$, equation (4.7) becomes

$$u_n \propto 2s_{\text{b},0}s_n\cos(\varphi_n - \varphi_{\text{b},0}). \tag{4.8}$$

In this case the near-field phase is related to the phase of the background signal φ_{b}, which is generally not constant during the measurement. Additionally, the factor $s_{\text{b},0}$, which is commonly referred to as multiplicative background, can be subject to changes during the scan, e.g. because of an inhomogeneous reflection coefficient of the sample surface. These two remaining influences of the background signal hamper the extraction of a reproducible near-field signal from a non-interferometric measurement.

The multiplicative background and the phase relation between near-field and background can be partly eliminated by applying the so-called Homodyne detection. This method takes advantage of a dominant power in the reference beam with respect to the DC background contribution ($s_{\text{ref}} \gg s_{\text{b},0}$). In combination with the demodulation for higher harmonics ($n \geq n_0$), equation (4.7) simplifies to

$$u_n \propto 2s_{\text{ref}}s_n\cos(\varphi_n - \varphi_{\text{ref}}). \tag{4.9}$$

The independent determination of the amplitude and phase is possible via two consecutive measurements with different positions of the reference mirror, i.e. a variation of the reference phase φ_{ref}. However, the accuracy of this method is experimentally limited mainly by the ratio $s_{\text{ref}}/s_{\text{b},0}$ between the signal strength of the reference beam and the DC background contribution and the stability of the reference phase φ_{ref} during the whole time of the two consecutive measurements.

The experimental limitations to the homodyne detection method have given rise to the development of a more sophisticated method called pseudoheterodyne detection, which enables a complete suppression of the multiplicative background and is robust to instabilities of the interferometer. Therefore, an oscillating mirror is placed in the interferometer, which alters the phase of the reference beam periodically. The frequency mixing of the tip and mirror oscillations introduce new frequency components to the detector output, which contain

the near-field information in principle free from background. The sinusoidal oscillations of the mirror can be taken into account by defining

$$\sigma_{\text{ref}}(t) = s_{\text{ref}}e^{i\gamma \sin(Mt)+\varphi_{\text{ref}}}. \tag{4.10}$$

In the experiment, the mirror is oscillating at $M \approx 300\,\text{Hz}$ and the phase modulation depth γ can be adjusted via the mirror oscillation amplitude. The reference phase φ_{ref} occurs as a constant phase offset. Equation (4.10) can be expanded into a Fourier series:

$$\sigma_{\text{ref}}(t) = \sum_{m\in\mathbb{Z}} \sigma_{\text{ref},m}e^{imMt}. \tag{4.11}$$

Utilizing the definition of the Bessel function of the first kind J_m of order m, the Fourier coefficients can be written as [103]

$$\sigma_{\text{ref},m} = s_{\text{ref}}J_m(\gamma)e^{i\varphi_{\text{ref}}+im\pi/2}. \tag{4.12}$$

The frequency mixing of the tip oscillation frequency with the mirror oscillation frequency and their higher harmonics leads to additional side bands in the power spectrum of the detector output voltage. The resulting power spectrum at the detector can be calculated by inserting equations (4.11) and (4.3) into equation (4.5). The spectral components of the sidebands for a suppressed additive background ($n \geq n_0$) are given by [103]

$$u_{n,m} \propto 2s_{\text{ref}}J_m(\gamma)s_n\cos(\varphi_n - \varphi_{\text{ref}} - m\pi/2) \quad n, m \neq 0. \tag{4.13}$$

A qualitative plot of the resulting power spectrum is given in figure 4.6. The black lines
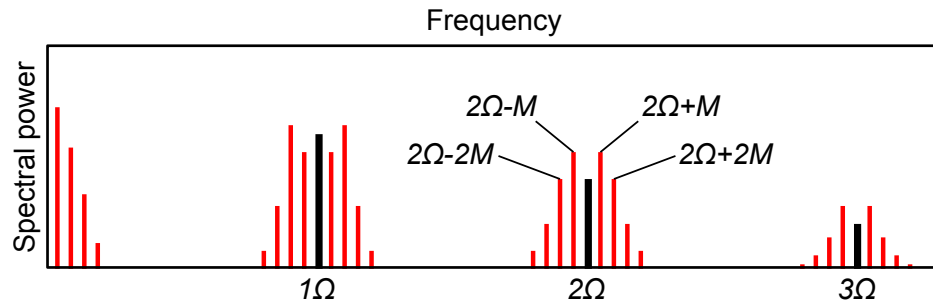

Figure 4.6: Qualitative power spectrum of the measured detector output voltage U during pseudoheterodyne signal detection. The mirror oscillation in the reference beam with frequency M splits up the spectral components of the higher harmonics of the tip oscillation frequency $n\Omega$ (black lines) into additional side bands at $n\Omega + mM$ (red lines). Figure reproduced from [103].

represent the higher harmonics $n\Omega$ of the tip oscillation frequency. The side bands at $n\Omega + mM$, shown in red, are free from multiplicative background, regardless of the ratio $s_{\text{ref}}/s_{\text{b},0}$. The complex near-field signal can be calculated utilizing equation (4.13) together

with Euler's formula from two successive sidebands e.g. $m = 1$ and $m = 2$:

$$\sigma_n \propto \frac{e^{i\varphi_{\text{ref}}}}{2s_{\text{ref}}} \left(i\frac{u_{n,1}}{J_1(\gamma)} - \frac{u_{n,2}}{J_2(\gamma)} \right). \tag{4.14}$$

By adjusting the phase modulation depth γ i.e. the oscillation amplitude of the mirror, such that $J_1(\gamma) = J_2(\gamma)$, the first two successive side bands directly contain the imaginary and real part of the near-field scattering coefficient:

$$\sigma_n \propto (iu_{n,1} - u_{n,2}). \tag{4.15}$$

The amplitude and phase of the near-field scattering coefficient is then given by:

$$s_n \propto \sqrt{u_{n,1}^2 + u_{n,2}^2} \qquad \varphi_n = -\arctan\left(\frac{u_{n,1}}{u_{n,2}}\right) + \varphi_{\text{ref}}. \tag{4.16}$$

The frequency components $u_{n,m}$ can be directly extracted from the detector output voltage via frequency demodulation utilizing a lock-in amplifier.

Although the pseudoheterodyne detection enables an extraction of the near-field signal σ_n in principle free from background, there are still some sources for disturbances left under experimental conditions. For instance, noise contributions from the external light source in the frequency range of the frequency components $u_{n,m}$ are directly transferred to the measured near-field signal. Furthermore, the long term stability of the reference phase φ_{ref} is limited, which is also transferred to σ_n. This often leads to a continuous drift of the extracted near-field phase φ_n along the slow axis of an s-SNOM scan. In general, choosing a "sufficiently high" demodulation order n_0 to suppress the additive background ($\sigma_{\text{b},n} \ll \sigma_n$) is always a compromise between minimal residual background and high signal-to-noise ratio in the measurement.

4.2.5 The near-field interaction

Until now, we have isolated the complex-valued scattering coefficient σ_n contribution to the scattered field, which purely stems from the near-field interaction between the tip and the sample. The important question remaining open is how the microscopic quantities, e.g. the near-field between the tip and the sample, or the local optical properties of the sample are encoded in σ_n. The following brief discussion highlights two different contributions to the tip-sample interaction, simplified to an extend, such that they can be described by a simple analytical model, the so-called point dipole model (PDM). The two contributions differ by the assumption of whether the tip or the sample is excited in the first place by the incident radiation, corresponding to figure 4.7 (a) or (b), respectively. In both cases, the tip is approximated by a point dipole with polarizability α above the sample. Due to the elongated shape of the tip in vertical direction, the point dipole approximating the tip can be assumed to be vertically aligned. In this case, the tensorial polarizability can be described
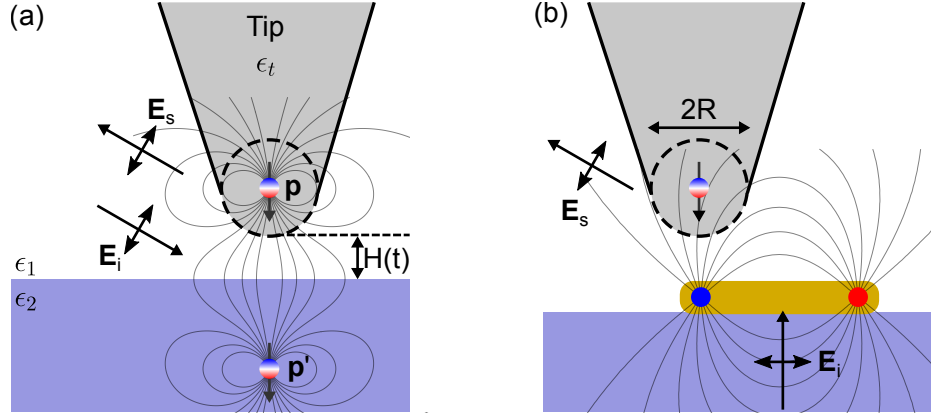
Figure 4.7: Schematic representation of the tip-sample interaction in the framework of the point dipole model for reflection mode s-SNOM in combination with a homogeneous sample (a), transmission mode s-SNOM above a resonantly excited plasmonic rod antenna (b).

by a single scalar value α_z: $\alpha = \text{diag}\left[0, 0, \alpha_z\right]$. Furthermore we can approximate α_z by the polarizability of a spherical particle [4]

$$\alpha_z = 4\pi R^3 \frac{\epsilon_t - 1}{\epsilon_t + 2},\tag{4.17}$$

with the dielectric function ϵ_t of the tip located in vacuum. The radius can be reasonably estimated to the radius of curvature of the tip apex $R \approx 25\,\text{nm}$.

When using the neaSNOM system in reflection mode, the incident light is p-polarized with an inclination angle of 30° with respect to the sample surface. Therefore it has a large fraction of vertical polarization and can strongly excite the tip directly. The excited dipole moment of the point dipole i.e. polarization of the tip is given by

$$\boldsymbol{p} = \boldsymbol{E}_i \alpha = [0, 0, E_{i,z} \alpha_z].\tag{4.18}$$

However, the total polarization of the tip-sample system changes due to the near-field interaction. Neglecting direct excitations of the sample e.g. surface plasmons or resonances in nanostructures, one can describe the response of the sample in the framework of image charges. The point dipole above the sample induces an image dipole inside the sample (c.f. figure 4.7 (a)), whose strength $\boldsymbol{p}' = r_p \boldsymbol{p}$ is related to the Fresnel reflection coefficient for p-polarized light

$$r_p = \frac{\epsilon_2 k_{z,1} - \epsilon_1 k_{z,2}}{\epsilon_2 k_{z,1} + \epsilon_1 k_{z,2}} = \frac{\epsilon_2 \sqrt{\epsilon_1 k_0^2 - q^2} - \epsilon_1 \sqrt{\epsilon_2 k_0^2 - q^2}}{\epsilon_2 \sqrt{\epsilon_1 k_0^2 - q^2} + \epsilon_1 \sqrt{\epsilon_2 k_0^2 - q^2}}\tag{4.19}$$

of the sample surface. Here, ϵ_2 denotes the dielectric function of the sample and ϵ_1 is the

permittivity of the medium above the sample. The near-field interaction is taking place via strongly evanescent fields with a lateral wavevector component $q \gg k_0$. Furthermore assuming $\epsilon_1 = 1$ leads to the reflection coefficient

$$r_{\mathrm{p}} = \frac{\epsilon_2 - 1}{\epsilon_2 + 1} \tag{4.20}$$

for evanescent fields. The excited image dipole in the sample reacts on the initial dipole in the tip leading to an additional dipole moment. An analytical self-consistent solution of the system of the two dipoles leads to the effective polarizability [29]

$$\alpha_{\mathrm{eff},z} = \frac{\alpha_z}{1 - \frac{\alpha_z r_{\mathrm{p}}}{16\pi(H+R)^3}} \tag{4.21}$$

of the tip in the presence of the sample. The scattered radiation is directly proportional to the dipole moment of the tip and therefore to the effective polarizability and the incident field:

$$E_{\mathrm{s}} = E_{\mathrm{i}}\sigma \propto \alpha_{\mathrm{eff},z} E_{\mathrm{i},z}. \tag{4.22}$$

The proportionality is sufficient to gather information of the local optical properties of the sample i.e. r_{p} by extraction of σ_n according to the description in the previous section. This can be done by normalizing the measured signal above a region of interest on the sample to a known reference material, i.e. calculating the so-called s-SNOM contrast $\sigma_n/\sigma_{n,\mathrm{r}}$. The reference signal $\sigma_{\mathrm{n,r}}$ is often measured on a metallic surface like gold or silver implying $r_{\mathrm{p}} = 1$ for large negative values of the metal permittivity ϵ_2 well below the plasma frequency. Despite the high level of simplification and approximation, PDM calculations are in reasonable agreement with experimentally determined near-field contrasts in reflection mode [104, 105]. Furthermore, the PDM predicts a resonance of $\alpha_{\mathrm{eff},z}$ for $\epsilon_2 \approx -1.7$, which can actually be measured in near-field experiments, however at a slightly different value of ϵ_2 [47]. A more refined model also utilizing the image charge approach, but describing the tip apex as a finite dipole reproduces the experimental contrasts and the position of the near-field resonance even better [106]. The models are also capable of describing layered samples by inserting the reflection coefficient r_{p} of the layer stack, which can be determined by the transfer matrix method [107]. The excellent quantitative agreement of these models with the experiments allow for a reliable extraction of local values of r_{p} and therefore also the dielectric constant ϵ_2 of the sample in many cases.

When using the NeaSNOM system in transmission mode, the light is vertically incident to the sample from below and thus has only polarization components in the sample plane (c.f. figure 4.7 (b)). The tip with its primarily vertically oriented polarizability α_z can not be excited directly by the incident radiation to a first appwoximation and the near-field interaction is initiated only by the sample. The evanescent waves for the near-field interaction can be provided e.g. by resonantly excited nanostructures or SPPs on the sample. This situation is depicted in figure 4.7 (b) with a plasmonic nanorod antenna acting as a resonantly excited

sample. In this case, the near-field interaction can be further simplified to an excitation of a dipole moment in the tip according to equation (4.18), with $E_{i,z}$ being the local vertical evanescent near-field above the sample. The influence of the excited point dipole in the tip on a laterally structured sample can no longer be described by the simple image charge model and is neglected here. The scattered light is then recovered by equation (4.22) replacing $\alpha_{\mathrm{eff},z}$ by α_z. Assuming α_z to be constant during the measurement, the measured quantity σ_n is directly proportional to the local vertical evanescent near-field above the sample. In this very simplified picture, the amplitude $|E_z|$ and phase φ of the vertical near-field above the sample directly correspond to the extracted values for the complex scattering coefficient s_n and φ_n in equation (4.16). However, one has to emphasize, that the correspondence between $|E_z|$ and s_n is only a proportionality. An absolute comparison of $|E_z|$ between different measurements on different samples, or even the same sample is not possible due to changing experimental conditions, like the power of the external source, or the microscopic geometry at the tip apex. Also the phase φ_n is defined only relative to the reference φ_{ref}, which is defined randomly for every new measurement and is typically subject to a drift even during a measurement, mainly originating from a thermal drift in the interferometer. Finding a reference for signal normalization to overcome this problem is more involved here than for reflection mode s-SNOM, because the sample has to be excited in the first place. Especially for spectroscopy applications, a potential normalization structure is required to give a broad and flat spectral response. Possible attempts could be off-resonant plasmonic structures, whose resonance(s) lie at much higher excitation frequencies compared to the examination frequency or inherently broadband effects like a propagating SPP launched from an extended edge. However, both attempts will probably not lead to large signals for the normalization amplitude $|E_{z,\mathrm{r}}|$ which may lead to relatively large errors due to a low signal-to-noise ratio.

4.3 Comparison of EELS and s-SNOM

As discussed in the previous sections, EELS and s-SNOM are experimental techniques to characterize evanescent near-fields. Although both techniques mainly reveal the vertical near-field component, there are significant differences, which make the two approaches rather complementary than redundant. Obviously, the first difference to mention is the excitation mechanism of optical modes in the sample. In EELS, the fast moving electron acts as an evanescent light source and can excite the sample only very locally. In s-SNOM the excitation depends on the operating mode. In reflection mode, the charge oscillations excited in the tip apex can also act as a local evanescent light source. However, when operating the s-SNOM in transmission mode, only the sample is primarily excited by the incident light from below in the first place. This far-field excitation is governed by the in plane polarizability of the investigated structure and the polarization of the incident beam. In contrast, localized sources can excite optically dark modes, which can not be excited from the far-field. This effect can be observed in the EELS measurements in chapter 5.

The interferometric detection scheme in s-SNOM enables the extraction of a complex near-field signal, i.e. near-field amplitude $|E_z|$ and phase φ, while the EELP is only related to $|E_z|$ assuming $\boldsymbol{v}_e$ parallel to the z-direction (c.f. equation (4.1)). In transmission mode, the s-SNOM is even capable of detecting propagating waves by separating the excitation via the lower parabolic mirror from the detection via the tip and the upper parabolic mirror. This feature is used for the near-field characterization of plasmonic slot waveguides (PSWs) in chapter 6.

A big advantage of EELS is the intrinsic broad spectral range. In principle the fast electron acts as a white light near-field source and can excite the sample over a huge spectral range. Therefore, an EELS measurement reveals the whole spectroscopic data of the investigated sample at once. Spectroscopic imaging in s-SNOM is either possible by recording consecutive images at different wavelengths in combination with a tunable light source, or by applying so-called nano Fourier transform infrared microscopy (nano-FTIR) in combination with a broadband light source [108]. Another advantage of EELS for spectroscopic analysis is the inherent possibility of signal normalization to the total amount of transmitted electrons, without the need of a normalization structure on the sample as required in s-SNOM. This ensures a better comparability between different EELS measurements. General limitations of the spectral range are given by the ZLP in EELS, which reaches out up to 1 eV corresponding to the near-infrared. In contrast, s-SNOM is applicable from the microwave regime up to the visible. However, for rather short wavelengths in the visible regime, the background suppression in s-SNOM is less efficient and the measurements can contain more artefacts, which do not result from the near-field interaction.

Another significant difference between EELS and s-SNOM are the requirements to the sample and the surrounding conditions. EELS requires an electron transparent sample in high vacuum conditions. Reflection mode s-SNOM can be operated under ambient conditions on every sample, which enables tapping mode AFM. Only very soft or extremely rough samples could lead to complications in this case. In addition, for transmission mode s-SNOM, the substrate of the sample must be transparent for the incident laser beam. Both EELS and s-SNOM can be considered as non-destructive and minimal invasive to the sample. In EELS, the electron beam may release carbon atoms from residual CO_2 molecules in the high vacuum, which locally deposit on the sample surface. During the tapping-mode AFM scan in s-SNOM measurements, very soft samples may be damaged by the tip. However, for most of the plasmonic samples investigated in this thesis, consisting of a thin gold film on a glass substrate, no damages of the sample due to the tip could be observed. Only when used in combination with freestanding thin film samples in section 5.3.3, the s-SNOM measurements have to be conducted very carefully to not destroy the samples.

Plasmonic hole arrays

In 1998, Ebbesen et. al. demonstrated the effect of an extraordinary optical transmission (EOT) through subwavelength hole arrays in thin, but optically opaque metallic films [109]. The "extraordinary" aspect of this finding lies in the fact that the power throughput even exceeds the integrated intensity over the complete aperture area constituted by all holes. Since then, the fundamental physics leading to this effect has been studied extensively in both theoretical and experimental works [110–115]. The mechanism behind the EOT phenomenon is the excitation of SPPs via the incident light due to the periodic arrangement of the holes in an array. As already discussed in section 2.3, the SPPs are confined to the surface and exhibit a smaller wavelength than a free space wave. These properties enable the SPPs to reach the other side of the metallic film through the holes and couple out to far-field radiation via the array again. Since the in- and outcoupling relies on the resonant excitation of the array, the EOT phenomenon is a relatively narrow-band effect. Variation of the array parameters opens up possibilities to tailor the resonance position and utilize the EOT phenomenon e.g. for optical color filters [116, 117] or so-called plasmonic printing [57]. The light confinement provided by the SPPs also makes the structure an attractive candidate for chemical sensing applications [118, 119]. Despite the huge number of fundamental studies regarding theory and experimental far-field measurements, there are only a few reports on near-field studies of comparable structures utilizing SNOM [120–125] and two studies on oligomer hole structures utilizing energy-filtered transmission electron microscopy (EFTEM) and EELS [86, 87]. The objective of this chapter is to provide a combined far- and near-field study of the SPPs involved in the EOT phenomenon. Prior to the experimental investigations, theoretical considerations are presented in the first section 5.1, which are restricted to freestanding plasmonic hole arrays for simplicity. The subsequently presented experimental investigations are performed on two different sample systems. In section 5.2, a combined far-field and EELS analysis is performed on a freestanding plasmonic hole array. These experimental results are compared with numerical computations and simulations. In section 5.3, plasmonic hole arrays, supported by a thin SiN membrane, are investigated by far-field and s-SNOM measurements.

5.1 Theoretical considerations

The EOT phenomenon involves SPPs excited by the periodic arrangement of the holes in an array. An efficient SPP excitation requires phase matching of the SPPs launched by each individual hole. For an incident plane wave onto the array, this resonance condition can be formulated as an equation in momentum space:

$$\boldsymbol{\beta}' = \boldsymbol{G} + \boldsymbol{k}_{\parallel}. \tag{5.1}$$

The occurring vectors lie in the plane of the thin film. $\boldsymbol{\beta}'$ is the real part of the SPP wavevector which has the magnitude β' known from the SPP dispersion relation discussed in section 2.3 and points into the SPP propagation direction. $\boldsymbol{k}_{\parallel}$ is the in-plane wavevector component of an incident plane wave under an angle with respect to the surface normal. For a normally incident plane wave, $\boldsymbol{k}_{\parallel}$ vanishes. $\boldsymbol{G}$ is the reciprocal lattice vector of the hole array. For a rectangular array with periods p_x and p_y as depicted in figure 5.1 (a), the reciprocal lattice vector is given by

$$\boldsymbol{G}_{m,n} = \frac{2\pi m}{p_x}\boldsymbol{e}_x + \frac{2\pi n}{p_y}\boldsymbol{e}_y, \tag{5.2}$$

where $\boldsymbol{e}_x$ and $\boldsymbol{e}_y$ are unit vectors along x and y-direction and m, n are integer numbers. Assuming normal plane wave incidence one can rewrite the phase matching condition (5.1) to the following scalar equation:

$$\beta'(\omega) = 2\pi\sqrt{\frac{m^2}{p_x^2} + \frac{n^2}{p_y^2}}, \tag{5.3}$$

Since the investigated plasmonic hole arrays in the following sections exhibit very thin film thicknesses below $100\,\mathrm{nm}$, the excited SPPs have to be described by the thin film SPP dispersion relation (2.40), which accounts for the coupling of the SPPs at the two interfaces of the film. According to the discussions in section 2.3.3, the thin film supports two propagating SPP modes, namely the long range mode and the short range mode, described by two dispersion branches (c.f. figure 2.3). In the limit of very thin films, only the short range mode exhibits a strong confinement to the interfaces. This opens two possible transfer channels for the excited short range SPP mode through the film. Firstly, the SPPs feature an enhanced direct transmission through the holes, enabled by the strong mode confinement as already known for thicker films [112]. Secondly, the short range SPPs enable a direct transfer through the thin film due to the coupled nature of the mode [115]. For a symmetric refractive index environment around the film considered here, the propagation constant β' of short range SPP mode is implicitly given by the first equation in (2.41). Inserting this short range SPP dispersion into equation (5.3), the resonance energies for an efficient excitation of the short range SPPs can be calculated numerically. A graphical representation of equation (5.3) is given in figure 5.1 (b). The energy dispersion of the short range thin film SPP mode for a
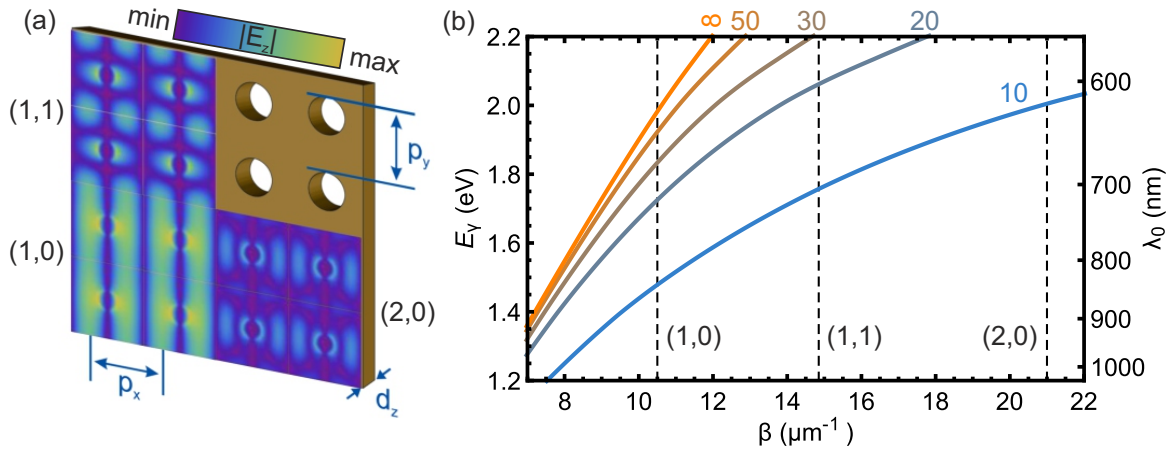
Figure 5.1: (a) Scheme of a thin gold film with a hole array. The color maps display the amplitude of the field perpendicular to the film $|E_z|$ in case of a resonant excitation of different array eigenmodes gained by finite element method simulations described below. (b) Short range SPP dispersion relation of a closed gold film of various thicknesses surrounded by vacuum according to the first equation in (2.41) in section 2.3.3. The dashed lines represent the values for β' calculated via equation (5.3), corresponding to the first three eigenmodes with $(m.n) = \{(1,0),(1,1),(2,0)\}$ of an array with $p_x = p_y = 600$ nm.

gold film surrounded by vacuum is plotted for different thicknesses in the same manner as in section 2.3.3. Additionally, the resonance positions for β' defined by the right hand side in equation (5.3) are marked by the vertical dashed lines for the first three occurring array eigenmodes with $(m.n) = \{(1,0),(1,1),(2,0)\}$ for a quadratic array with $p_x = p_y = 600$ nm. The intersections of the dashed lines and the dispersion relations reveal the resonance energies of the respective array mode and film thickness. The solutions for the eigenenergies of the first three modes are plotted over film thickness as solid lines in figure 5.2 . The calculations predict a blueshift of the resonance energies with increasing film thickness, which saturates for large film thicknesses, as the short range SPP dispersion approaches the single interface dispersion (c.f. section 2.3.3).

In addtion to the predictions of the calculations from the analytical model, figure 5.2 also includes data points which were extracted as a result from finite element method simulations. The simulations are performed with the commercially available software package *Comsol Multiphysics*. The simulation domain includes a single hole in the center of a quadratic piece of gold film with edge lengths of 600 nm corresponding to the period of the holes (see inset of figure 5.2). Periodic boundary conditions are applied to each edge of the film. The film thickness is varied in six discrete steps between 10 nm and 100 nm. The simulation domain has a total height of 500 nm in z-direction and the film is centered in the middle. The simulation domain is delimited by an input port on the lower side and an output port on the upper side. The input port defines a plane wave excitation vertically incident from below onto the hole array. From the two ports, one can extract the optical transmission and
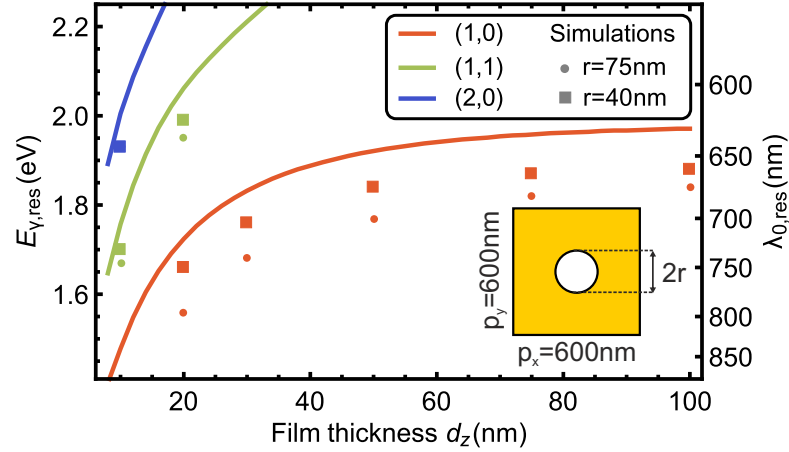
Figure 5.2: Resonance energies $E_{\gamma,\mathrm{res}}$ for the first three array modes $(m.n) = \{(1,0),(1,1),(2,0)\}$ for different film thicknesses. The solid curve results from the resonance condition in equation (5.3) numerically solved for the photon energy. The distinct datapoints correspond to resonance positions extracted from finite element method simulations of the structure for two different hole radii and different film thicknesses.

reflection. The excitation frequency is swept from 375 THz to 500 THz in steps of 5 THz corresponding to an energy range of 1.55 eV to 2.07 eV and a wavelength range of roughly 600 nm to 800 nm in each simulation. From the acquired transmission and reflection data, one can also calculate the absorption. The resonance energies displayed in figure 5.2 are identified by local maxima in the absorption spectrum. The film thickness and frequency sweep is executed for the two different hole radii 75 nm and 40 nm. Both simulation series are depicted in figure 5.2 as discrete datapoints. In general, both simulation series follow the same trend as the calculations from the analytical model, i.e. the resonance energies of the (1,0) and (1,1) mode, shift blue for increasing film thickness. The (2,0) resonance could only be observed for a 10 nm film in the frequency range of the sweep. In general, the simulation series of both hole sizes underestimate the resonance energies compared to the calculations from the analytical model. However, the deviation is larger for the large hole radius of 75 nm. These findings can be explained by a shift of the SPP dispersion relation in the presence of the holes with respect to the dispersion relation of a closed film. A potential explanation could be a reduction of the plasma frequency due to the dilution of the metal film by the holes, which leads to a redshift of the whole SPP dispersion relation. The larger the holes, the stronger the effect of the dilution and the stronger the redshift.

5.2 Freestanding hole arrays

The experimental investigations presented in this section include EELS as a broadband energy, nanoscale near-field imaging technique. However, the application of this technique

requires the samples to be transparent for fast electrons. In order to maximize the electron transparency, freestanding metal films are the most desirable choice as a sample system. The investigated samples are fabricated by the approach for freestanding structured thin gold films presented in section 3.3 with different film thicknesses from 22 nm to 74 nm. Each sample includes an asymmetric circular hole array with 800 nm period in horizontal (x) direction and 600 nm period in vertical (y) direction. The arrays consist of 100×100 holes, leading to array dimensions exceeding the focal size of the illuminating spot to exclude edge effects during the optical transmission spectroscopy. The radius of each individual hole is about 100 nm. All samples are characterized by optical transmission measurements in the far-field. The thinnest sample of 22 nm film thickness is additionally characterized in the near-field utilizing EELS. The experimental results are compared with numerical computations based on the discontinuous Galerkin time-domain (DGTD) method [126, 127]. These computations were performed by Thomas Kiel from the group of Professor Kurt Busch at the Institut für Physik, Humboldt-Universität zu Berlin.

5.2.1 Optical transmission spectra

The optical transmission spectra are recorded with the setup depicted in figure 5.3. The light of a halogen lamp is collimated by a lens and coupled into a multimode fiber with a mode field diameter of 50 μm by a second lens. The fiber output serves as a point light source which is collimated by another lens. The unpolarized beam is passing a rotatable Glen-Thomsen polarizer to arbitrarily determine the transmitted polarization. The polarized beam is focused onto the sample via a 0.1 NA objective and the transmitted or scattered radiation is collected and recollimated by a 0.4 NA objective.
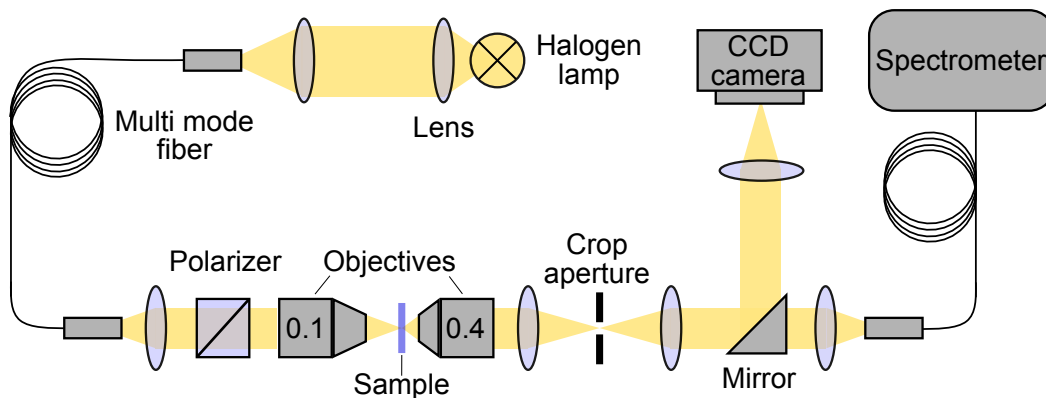
Figure 5.3: Setup for far-field optical transmission spectroscopy. The sample is illuminated by a collimated polarized beam created by a fiber setup from the light of a halogen lamp. Illumination and collection of the light is realized by two objectives around the sample. The subsequent imaging setup includes a charge-coupled device (CCD) camera for real space imaging and a fiber coupled spectrometer for the analysis of the transmitted light.

The choice of the NAs combine a preferably perpendicular illumination of the sample with a large spherical angle of collection for the transmitted light. The structures of interest on the sample can be positioned in the shared focus of the two objectives via a three-axis mechanical micrometer stage. A nonmagnifying Gallilei telescope creates an intermediate real image of the sample. An adjustable rectangular aperture at this position allows to reduce the following spectroscopic analysis to a desired rectangular region of intrest. The intermediate real image can be mapped onto a CCD camera via an optional beampath provided by a replaceable magnetic mirror in order to adjust the sample position and the crop region. When the magnetic mirror is removed, the beam is coupled into a *Princeton Instruments* SP2150 spectrometer via another multimode fiber. The incident spectrum is filtered by a reflection grating in combination with a slit aperture. The intensity is detected by an amplified Silicon / indium-gallium-arsenide sandwitch diode. This enables a spectral measuring range roughly from 500 nm to 1650 nm. For normalization, all spectra are divided by a reference spectrum, which is recorded without the sample directly after the respective measurement on the sample. This procedure cancels the spectral characteristics of the setup, e.g. from the light source, detector and optical elements.

The optical transmission measurements of the hole arrays are performed with a polarization of the incident light in x- and y-direction, respectively. The upper left panel of figure 5.4 shows experimental optical transmission spectra for x-polarized excitation of samples with all film thicknesses d_z given in nanometers in the corresponding color. Inspecting the red curve for the 22 nm thick film, one can observe two clear resonances around 1.3 eV and 1.8 eV respectively. The first observed resonance with the lowest energy at 1.3 eV corresponds to the $(1,0)$ mode of the hole array. The second resonance around 1.8 eV can be attributed to the $(1,1)$ mode. It exhibits a higher resonant optical transmission than the $(1,0)$ mode and is spectrally braoder. Both resonances exhibit a blueshift and a decreasing amplitude with increasing thickness of the gold film. The observed spectral shift recovers the findings in the theoretical considerations in section 5.1 and is caused by a shift of the SPP thin film dispersion relation. The exceptionally larger transmission in the $(1,0)$ mode resonance for the 29 nm film than for the 22 nm film can be explained by a slightly smaller diameter of the holes in the latter. For the $(1,1)$ mode, there is no exceptionally higher transmission for the 29 nm film with respect to the 22 nm sample. The slightly different hole sizes may have smaller impact here, because the SPP wavelength is shorter and the confinement is higher. Thus the SPP wave can better pass the smaller holes of the 22 nm sample.

The upper right panel of figure 5.4 shows experimental optical transmission spectra for y-polarization. The first resonance, which lies around 1.55 eV for the 22 nm film corresponds to the $(0,1)$ mode of the array. As expected, it lies at higher energies than the $(1,0)$ mode due to the smaller period in y-direction. Also the $(0,1)$ mode is blueshifted with increasing film thickness. The exceptional transmission behaviour for the 29 nm film observed for the $(1,0)$ mode is also recovered in the $(0,1)$ mode. Additionally, the $(1,1)$ mode can be observed at around 1.9 eV, however with a weaker optical transmission enhancement than the $(1,0)$ mode in this case. The $(1,1)$ resonance is also weaker compared to the measurements with horizontal polarization and slightly blueshifted.
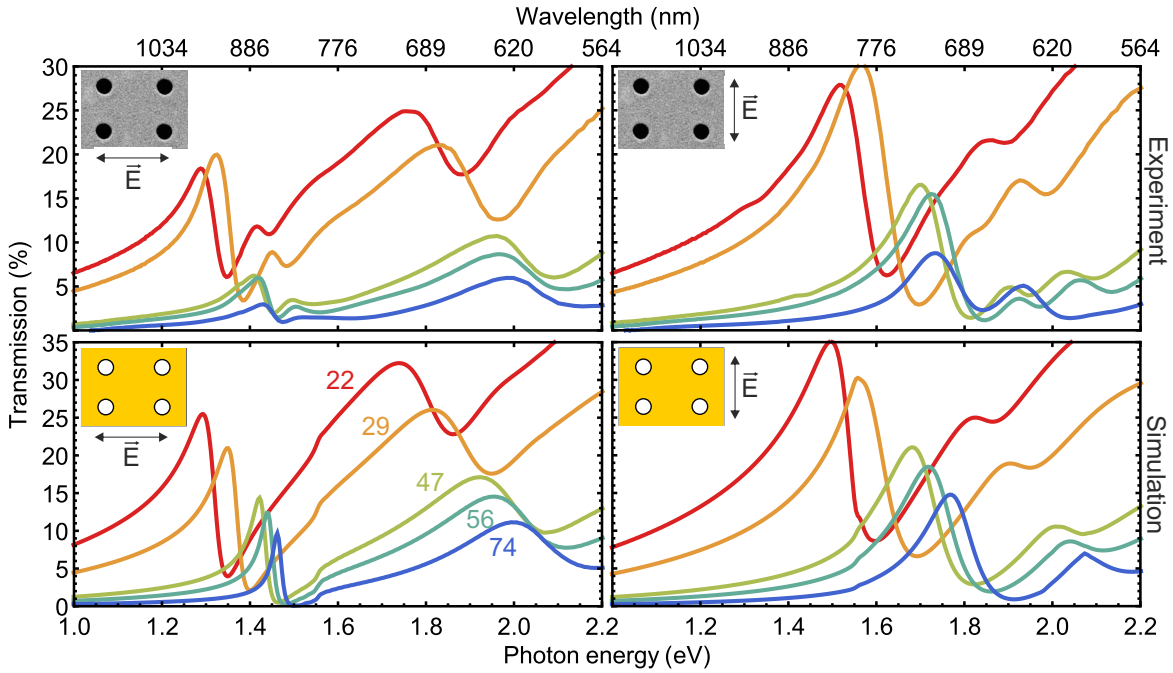
Figure 5.4: Optical transmission spectra of the freestanding hole arrays with different film thicknesses and incident polarizations. The film thicknesses are given in nanometers in the respective color. The electric field is polarized along the horizontal (x) direction (800 nm array period) in the left panels and along the vertical (y) direction (600 nm array period) in the right panels. Experimental spectra are shown in the upper panels. Simulated spectra are shown in the lower panels. In this case, a plane wave is incident normal to the sample surface.

The two lower panels in figure 5.4 show the corresponding simulated transmission spectra by Thomas Kiel for comparison. In the simulations, a pulsed plane wave is send under straight incidence on a single $p_x = 800$ nm times $p_y = 600$ nm unit-cell. The transmission spectrum is obtained from the transmitted energy flux, which is normalized to the incident flux. The thickness of the film is varied between $d = 22$ nm to $d = 74$ nm and the hole radius is 100 nm to match the experimental conditions. The surrounding air is modelled with $\epsilon = 1$ and the gold film is modelled using a Drude-Lorentz-model similar to reference [128]. The spectral positions of the two array resonances are in excellent agreement with the experimental data. The overall transmission in the calculated spectra is larger, which indicates a slight underestimation of the losses for the SPPs on the metal film. The blueshift of all resonances is also recovered in the simulations. However, the exceptional behaviour of the 29 nm film is absent in this case, which is in accordance with the interpretation of a slightly smaller hole diameter of the 22 nm sample in the experiments. Another significant difference between simulation and measurement is an additional feature in the experimental spectra, which occurs between the $(1, 0)$ mode and the $(1, 1)$ mode for horizontal incident polarization and between the $(0, 1)$ mode and the $(1, 1)$ mode for vertical incident polarization. This additional feature may result from the fact, that the incident beam is focused onto the sample

in the experiments leading to a nonvanishing in-plane wavevector component in contradiction to a vertically incident plane-wave illumination for the simulations.

5.2.2 EELS Experiment

In addition to the optical transmission spectra, an EELS measurement is performed on the thinnest 22 nm film. For the thicker samples, EELS measurements are not evaluated, since the thicker samples transmit a significantly lower amount of electrons, which leads to an unreasonable signal-to-noise ratio. The EELS measurement is conducted with the *Zeiss* Libra200 MC Cs-STEM which is explained in further detail in section 4.1. In order to record EELS maps, the electron beam is raster-scanned across the sample with a resolution of 4.9 nm per pixel. A spectrum is recorded in each pixel with an acquisition time of 8 ms. As a postprocessing step, the spectra in each pixel are normalized to their total number of counts and the ZLP is centered at 0 eV respectively. The energy resolution is roughly 0.13 eV in this case and is limited by the energy width of the ZLP. Figure 5.5 (a) shows the optical
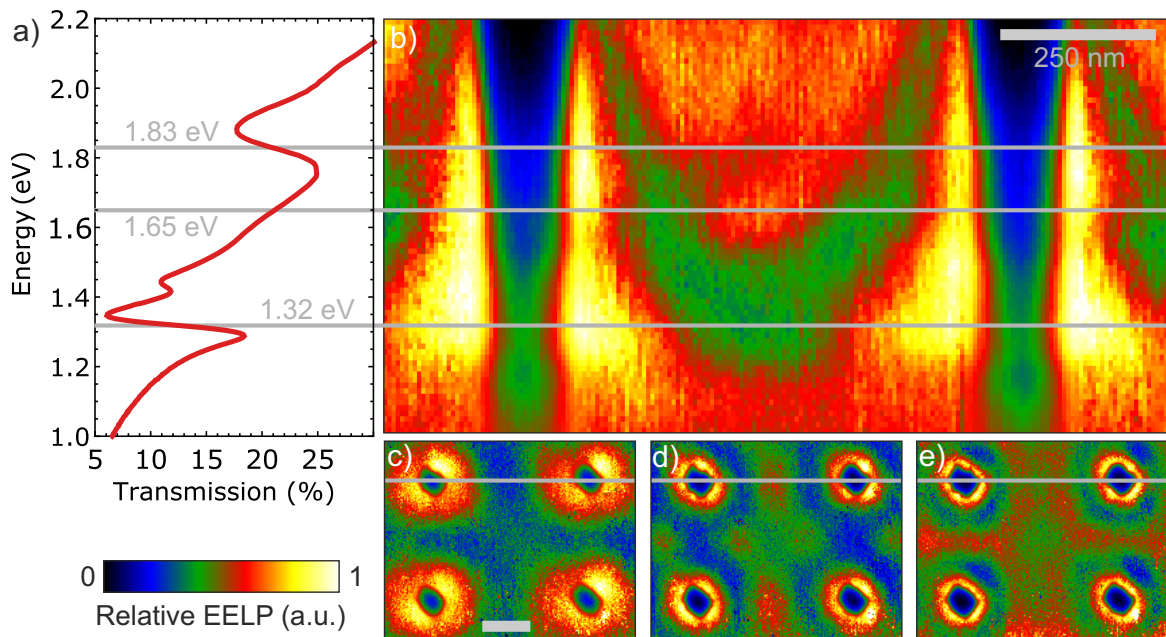
Figure 5.5: Comparison of the optical transmission spectrum with EELS data for the 22 nm film. (a) Optical transmission spectrum. (b) EELS data extracted from a horizontal line profile through two holes extruded over the energy range of the optical transmission data. The grey lines indicate important near- and far-field features. (c-e) EELS maps of the corresponding features in (a,b). (c): 1.32 eV, (d): 1.65 eV, (e): 1.83 eV. The scale bar in (c) is 250 nm.

transmission spectrum of the 22 nm film in comparison with the EELP of a line profile through two holes in horizontal direction extruded over the energy range from 1 eV to 2.2 eV (Figure 5.5 (b)). From the data shown in figure 5.5, one can identify three spectral features

at the energies of 1.32 eV, 1.65 eV and 1.83 eV respectively. Figures 5.5 (c,d,e) show EELP maps of the recorded dataset including 4 holes at each energy-loss corresponding to the spectral features. Each feature is highlighted by a grey solid line which indicates its energetic position in (a) and (b), as well as the vertical position of the profiles in the EELP maps in figures (c,d,e), which contribute to figure 5.5 (b).

The first spectral feature at 1.32 eV (c) corresponds to the $(1,0)$ mode of the hole array which consists of a standing wave between the holes on the horizontal axis. The standing wave pattern exhibits two antinodes between a pair of holes, corresponding a phase shift of 2π between two successive holes as expected for the $(1,0)$ mode. The next spectral feature, which occurs at an energy of about 1.65 eV can only be observed in the EEL spectra, but not in the optical transmission measurement. The mode pattern revealed by the EELP map in (d) can be interpreted as a standing wave with three antinodes between two holes, which corresponds to a phase shift of 3π. Therefore, this mode can not be excited by a vertically incident plane wave and the spectral feature is absent in the optical transmission spectrum. In contrast, the swift electron used for the EELS measurement is capable to excite this dark "$(1.5,0)$" mode of the array, because it acts as a local source. The spectral feature in the optical transmission spectrum occurring at 1.83 eV corresponds to the $(1,1)$ mode of the array. It has in-plane momentum contributions both in horizontal and vertical directions. The phase shift between two adjacent holes on the horizontal axis as well as on the vertical axis should amount 2π, respectively. Therefore it can be excited by a plane wave and is observed in the optical transmission spectrum. The expected phase shift of 4π on the two diagonal axes between the holes can be observed from the EELS map in figure 5.5 (e) from the occurrence of four antinodes on these axes.

For the two observed bright (1,0) and (1,1) modes, the data shown in figure 5.5 reveal a spectral redshift of the near-field resonance defined by the standing wave patterns with respect to the far-field resonance defined by the optical transmission maximum. This discrepancy is well-known for LSPPs on plasmonic nanostructures and can be explained by a shift between the maximum kinetic energy and the maximum potential energy of a damped driven harmonic oscillator [129]. For large plasmonic particals, the redshift can amount up to half of the resonance bandwidth. This behaviour is reproduced by the resonances of the array eigenmodes. In order to support the interpretation of the experimental data, regarding the assignment of the modes to the spectral features table 5.1 lists the magnitudes of the SPP wavevector requiered for the different array modes respectively. Since the dispersion relation $E(\beta)$ of the thin film SPPs is monotonically increasing (c.f. figure 5.1 (b)), the order of appearance of the different modes with respect to the resonance energy observed in the experiments should match the order related to the total momentum of the SPP wavevector β listed in the table. Comparing the table to the findings from the experimental investigations, the different modes appear in the expected order. The modes with larger in-plane momentum than 13.1 μm^{-1} of the $(1,1)$ mode can not be clearly identified from the measurements. This can be attributed to the fact, that the required mode energy is approaching the first interband transition of gold. In order to investigate these modes experimentally one could either enlarge the periods in the array or use silver films.

Mode	β (μm^{-1})	λ_{SPP} (μm)
$(1, 0)$	7.9	0.8
$(0, 1)$	10.5	0.6
$(1.5, 0)$	11.8	0.53
$(1, 1)$	13.1	0.48
$(0, 1.5)$	15.7	0.4
$(2, 0)$	15.7	0.4

Table 5.1: Total in-plane momentum of the SPP wavevector calculated by equation (5.3) for different array modes (m,n) of the array with $p_x = 800\,nm$ and $p_y = 600\,nm$.

5.2.3 EELS Simulation

To further confirm the experimental EELS results and support the interpretation, numerical computations based on the DGTD method have been performed. The conduction and the following short description of the simulation method was elaborated by Thomas Kiel.

In contrast to the plane wave excitation used for the transmission spectra, the field of a swift electron moving at $v = 0.77\,c$ is used as source-term for the computations of the EELP spectra. The loss probability can be computed from the field scattered back from the $d = 22\,nm$ thick gold film in the no-recoil approximation via [92, 95]

$$\Gamma(\omega) = \frac{e}{\pi\hbar\omega} \int dt\, Re\left[e^{-i\omega t} \boldsymbol{v} \cdot \boldsymbol{E}_{ind}(\boldsymbol{r}_0 + \boldsymbol{v}t, \omega) \right]. \qquad (5.4)$$

A variation of the transverse position of the swift electron trajectory yields spatially resolved EELP spectra. To circumvent the numerical problem of evaluating the diverging electron field when the electron beam hits the material, a radial Gaussian charge distribution is imposed with a width of $\sigma = 2\,nm$ in the rest-frame of the electron. Furthermore, the computational domain needs to be extended from a single unit-cell using periodic boundary conditions to a super-cell of 9×9 unit-cells here. Otherwise, every unit-cell would be excited by a swift electron simultaneously. Outside the 9×9 unit-cell the gold-film is terminated using stretched coordinate perfectly matched layers [130, 131]. The utilized finite-element mesh discretization includes elements with side lengths as small as $20\,nm$ to guarantee a sufficient resolution to represent the holes. A third-order Lagrange polynomial basis is used for the expansion of the electromagnetic fields.

The computed EELS-data is displayed in the same manner as the experimental data in figure 5.6. In general, the simulated EELS data is in excellent agreement with the experiment. The spectral features found for the experimental data are reproduced by the calculations. The mode energies are in accordance with the experiment within a few tens of meV. Also the observed redshift of the near-field resonances with respect to the far-field transmission maxima is reproduced by the simulation data.
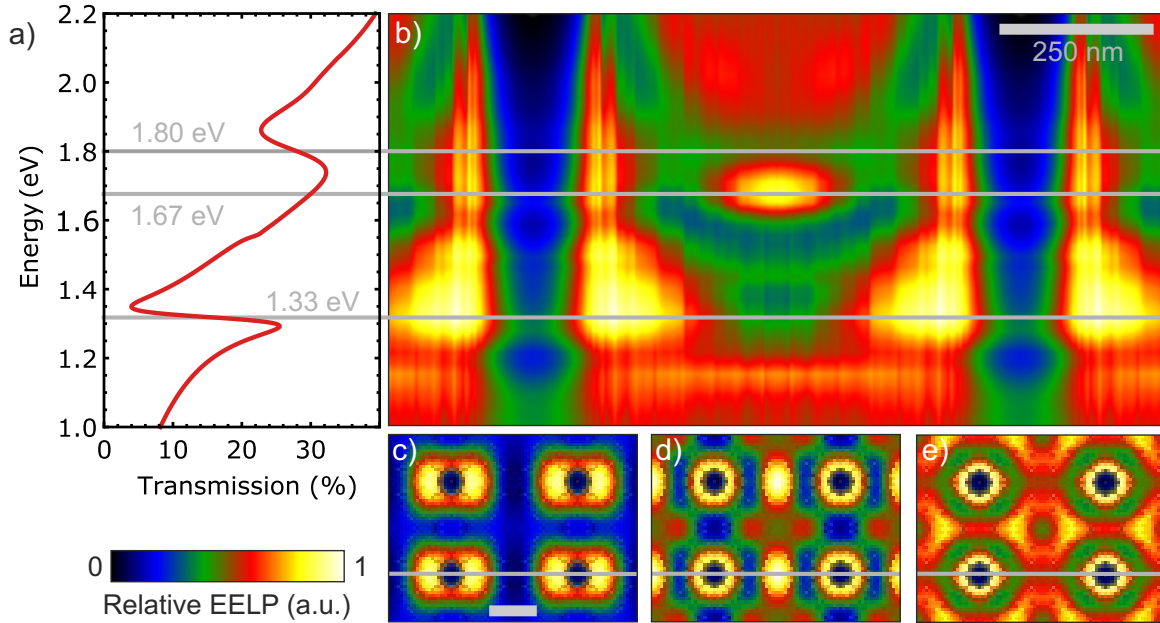
Figure 5.6: Simulated optical transmission and EELS data corresponding to the experimental results in figure 5.5.

5.2.4 Summary

Figure 5.7 summarizes the experimental and simulation results of the latter section in comparison with theoretical predictions from the thin film SPP dispersion. The colored curves show the resonance energies of the first three bright modes extracted from all experimental and simulated optical transmission spectra. The resonance positions correspond to the turning point between the minimum and maximum of the corresponding far-field resonance as exemplarily given by the gray lines in figure 5.5 (a) at 1.32 eV and 1.83 eV. For the $(1, 1)$ mode, the extracted values of the measurements and simulations with horizontal and vertical incident polarizations are averaged. The calculated points (marked as rhombs) correspond to the solution of the resonance condition in equation (5.3) inserting the dispersion relation $\beta(\omega)$ of the short range thin film SPP dispersion. The values for β of the respective array modes are taken from table 5.1. For all three modes, one can observe an excellent agreement of the experimental and simulated data. However, the calculated values exhibit significantly higher resonance energies compared to the measurements and simulations. As already discussed in section 5.1, this can be understood by a shift of the plasma frequency due to an effective dilution of the metal film by the holes.

The three black datapoints correspond to a dark mode of the array, which can only be extracted from the EELS measurements. This mode can be effectively described by setting $(m, n) = (1.5, 0)$ in equation (5.3), corresponding to a phaseshift of 3π between two adjacent holes on the horizontal axis. Therefore an optical excitation via a vertical incident plane wave leads to a destructive interference of the SPPs excited by two adjacent holes and hence
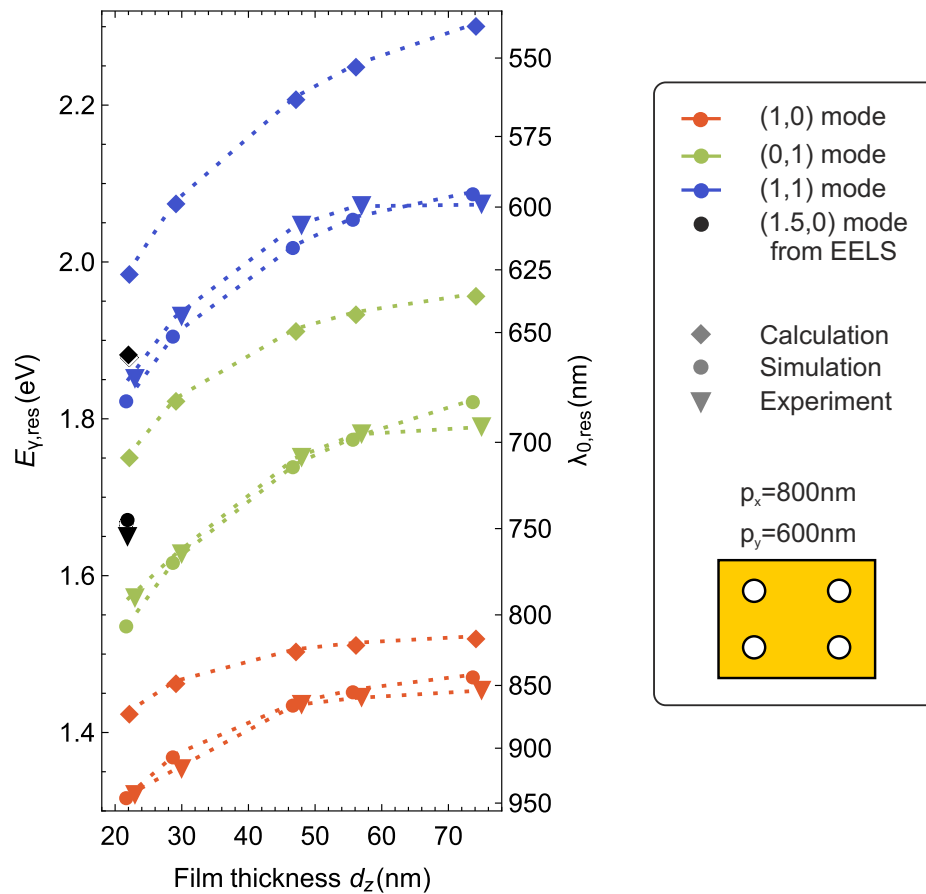
Figure 5.7: Summarizing graph of the experimental (triangles) and simulation (disks) results in comparison with theoretical calculations (rhombs). The different colors correspond to the first three bright modes of the array. The black datapoints represent the dark "$(1.5, 0)$" mode.

the mode can not be excited. The extracted datapoints from the experimental and simulated EELS data of the thinnest 22 nm film lie between the corresponding datapoints of the $(0, 1)$ and $(1, 1)$ mode, as expected from the order in table 5.1. This behaviour is also recovered by the calculated datapoints. Like for the bright modes, the calculations predict a higher resonance energy than gained by the experiment and simulation, which might be due to the dilution of the metal film by the holes.

5.3 SiN supported hole arrays

In addition to the investigation of freestanding plasmonic hole arrays presented above, another investigation on a sample system of SiN supported plasmonic hole arrays is presented in this section. A sketch of the sample system is depicted in figure 5.8. The plasmonic hole array is buried below a continuous SiN layer with a thickness of 30 nm. The intended purpose of
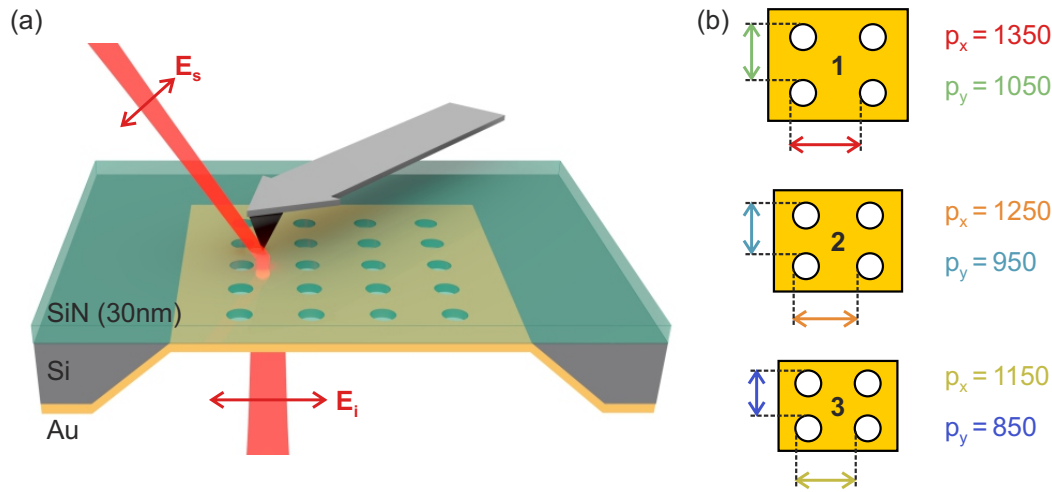
Figure 5.8: (a) Sketch of the SiN supported plasmonic hole array during a transmission mode s-SNOM measurement. The gold film is buried below the 30 nm SiN supporting film, which allows for s-SNOM scans on the top side of the sample. (b) The three fabricated variations of asymmetric hole arrays. The periods in horizontal and vertical directions are given in the respective colors, which cover the spectrum from blue to red corresponding to the range from shortest to longest array periods.

this sample system is to simultaneously allow for s-SNOM and EELS measurements. The continuous SiN layer enables AFM scans on the top side and is thin enough to transmit a significant amount of the evanescent near-fields from the buried plasmonic hole array to the tip. In principle, the SiN layer is also thin enough to serve as an electron transparent sample for EELS measurements [132, 133]. However, for the plasmonic hole array samples, the interest lies on the near-fields on the gold film, rather than inside the holes. Therefore, to resolve the regions of interest via EELS, the electron beam has to transmit both the SiN layer and the gold film. The combined thickness of gold and SiN film significantly drops the transmission of the electron beam during an EELS measurement. Additionally, the samples were designed to support array resonances in the near-infrared regime at wavelength around 1500 nm corresponding to photon energies of 0.83 eV. Therefore, the detectable energy-loss during an EELS measurement is already in close proximity to the ZLP, which caused further complications in this context. For these reasons EELS measurements could not be successfully performed on this sample system and only a s-SNOM and far-field analysis is presented in the following. The experimental investigation includes a parametric study of samples with different combinations of asymmetric hole arrays and thicknesses of the gold film.

5.3.1 Samples

The fabrication of the samples starts with a commercially bought SiN membrane from *Silson Ltd*. The 30 nm SiN layer is supported by a 200 μm thick silicon frame. The Si frame exhibits

four $100\,\mu m \times 100\,\mu m$ windows, where the SiN layer is forming a freestanding membrane. As a first fabrication step, the lower side of the sample is covered with a gold film of the desired thickness via thermal evaporation according to section 3.1.1 including a 2 nm chromium adhesion layer. Secondly, the hole array is patterned into the gold film via focused ion beam milling (c.f. section 3.2) on the lower side of the membrane. Each hole is patterned by the ion beam according to the customized beampath shown in figure 3.3 (c) and exhibits a diameter of 500 nm. The applied ion beam dose is carefully chosen for each gold film via preliminary dose tests, such that the gold inside the holes is completely removed but the SiN membrane remains intact. This is important to preserve a continuous surface on the upper side of the completed sample for the s-SNOM scan, as depicted in figure 5.8 (a). The plasmonic hole arrays are fabricated in three different configurations, which are schematically depicted in figure 5.8 (b). Each configuration composes an asymmetric hole array with different array periods along the horizontal and vertical direction. The periodicities for all array configurations are clarified by the color coded text in figure 5.8 (b). The utilized colors cover the spectrum from blue to red corresponding to the range from shortest to longest array periods. All three different arrays are fabricated respectively in four gold films with variable thicknesses ranging from 20 nm to 50 nm in steps of 10 nm. For each film thickness, one Si-frame is used, where the array combinations are written in three of the four available SiN membranes. In total, this results in twelve sample membranes on four Si frames with all combinations of the four thicknesses and three array types.

5.3.2 Far-field transmission spectra

Figure 5.9 shows far-field optical transmission spectra of almost all fabricated sample combinations. The spectra are recorded with the setup depicted in figure 5.3 utilized for the freestanding samples in section 5.2.1. All spectra are recorded in a wavelength range between 600 nm and 1600 nm, which is safely included in the operating range of the illumination source (Halogen lamp) and the detector (silicon/indium-gallium-arsenide sandwich diode) to prevent errors at the borders of the operating range of the setup. The samples are illuminated from the gold covered side of the membrane. For each film thickness, all three array configurations shown in figure 5.8 (b) are measured with an incident polarization along the given x- and y-direction. The six resulting spectra per film thickness are plotted together in one panel in figure 5.9, respectively. Thereby, each spectrum is depicted in a certain color, corresponding to the color of a certain array period introduced in figure 5.8 (b), along which the incident light is polarized. For example, the red curves correspond to measurements of array configuration 1 with x-polarized incident light (along the period of 1350 nm). Exceptionally, for the thinnest film of 20 nm, there are no measured spectra for array 2 ($p_x = 1250$ nm and $p_y = 950$ nm). The supporting membrane of this array was broken after the s-SNOM measurements were performed, such that this array could not be investigated by far-field optical transmission spectra.

All recorded transmission spectra exhibit a strong resonance in the long wavelength regime of the measurement range. For the smaller array periods, the corresponding
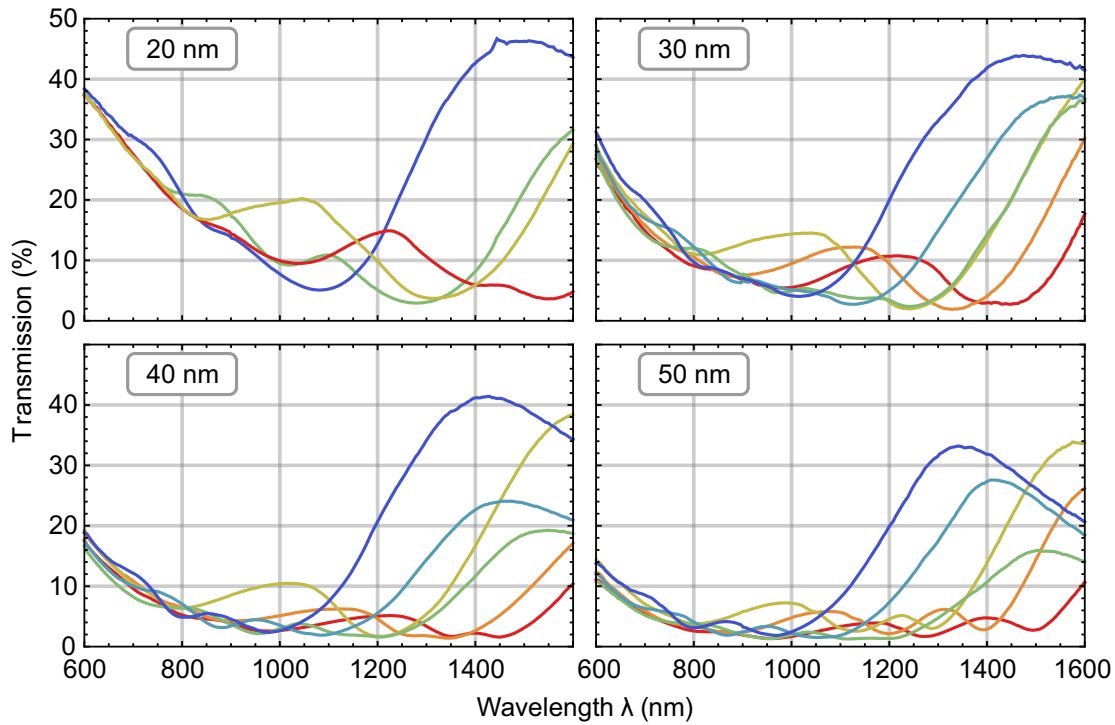
Figure 5.9: Far-field optical transmission spectra of all fabricated sample configurations. Each panel corresponds to a different thickness of the gold film and contains six spectra (except for the first panel due to a broken membrane) of all three array configurations measured with *x*- and *y*-polarized incident light respectively. Thereby, each spectrum is depicted in a certain color, corresponding to the color of a certain array period introduced in figure 5.8 (b), along which the incident light is polarized.

transmission maximum can be fully observed within the range of the spectroscopic data. These strong resonances in the spectra can be attributed to the $(1, 0)$ and $(0, 1)$ modes of the asymmetric arrays. The $(1, 1)$ mode can be excluded as the origin, because the resonance is drastically shifting when comparing measurements on the same array with orthogonal incident polarizations. Higher modes, like the $(2, 0)$ mode are also unlikely as the origin, because they are expected to occur at shorter wavelength.

One can compare the blue curves (polarization along the 850 nm period on array 3) for the different film thicknesses to the transmission data of the freestanding film excited by *x*-polarized light (along the 800nm period) shown in figure 5.4 in the previous section. Despite the comparable array periods on both samples, on the SiN supporting film, the resonance is significantly redshifted compared to the freestanding film samples. This is due to the refractive index of the SiN substrate, which increases the propagation constant of the thin film SPPs. Furthermore, the resonance on the SiN samples is significantly broadened, which may be attributed to the asymmetric refractive index environment or to the larger hole diameters.

Comparing the resonance positions for a certain film thickness, one can observe the expected redshift with an increasing array period along the incident polarization direction (blue to red curve in each panel in figure 5.9). Furthermore, by separately inspecting the behaviour of curves of the same color (array period) with altering film thickness, one can observe a blueshift of the resonance with increasing film thickness. As for the freestanding samples in section 5.2 this can be attributed to coupling of the SPPs on the upper and lower side of the gold film, leading to a shift of the thin film SPP dispersion relation.

Inspecting the spectra for the 50 nm and 40 nm films, it is apparent that the strength of the resonant optical transmission enhancement varies between the different array configurations. For array configuration 3, which constitutes the shortest periods, the resonant optical transmission enhancement is the highest and comparable for the $(1, 0)$ and $(0, 1)$ mode. Array configuration 2 exhibits a moderate and array configuration 1 the lowest resonant optical transmission enhancement. This behaviour can be attributed to the varying hole density in the arrays. Since the hole diameter is constant for all array configurations, array 3 exhibits the highest hole density and therefore also the largest integrated aperture size from the contribution of all holes.

On the low wavelength edge of all spectra, the optical transmission exhibits an increase with decreasing wavelength, which is independent of the array parameters. This increase of the optical transmission can be attributed to the spectral approach to the interband transitions in the gold. Between the $(1, 0)$ and $(0, 1)$ resonances at the long wavelength side of the spectra and the nonresonant transmission increase at the low wavelength side exists one more smaller feature. This feature is most clearly pronounced in the measurements on the 20 nm and 30 nm thick samples for the excitation along the longer period axes of the arrays (red to yellow curves). This weaker resonance may belong to the $(1, 1)$ mode of the array. This interpretation is consistent with the findings from the freestanding samples because of the following two accordances in the behaviour: Firstly, the resonance is weaker compared to the $(1, 0)$ and $(0, 1)$ resonances. Secondly, the mode is excited more efficiently with a polarization along the long period axis of the array. However, the blueshift of the resonance with increasing film thickness is less pronounced than for the freestanding film samples. This is partly caused by the fact, that the spectra are plotted over wavelength in this case rather than over energy for the freestanding films.

In some of the spectra occurs an additional feature between the $(1, 1)$ and the $(1, 0)$ or $(0, 1)$ mode. As for the freestanding films, this feature may be attributed to the fact, that the sample is illuminated by a focused beam rather than a plane wave. Therefore the illumination can contain wavevector components in the sample plane, which can cause the additional features in the spectra. In general, both the resonant and nonresonant optical transmission increases with decreasing film thickness. This is also in accordance with the findings from the measurements on the freestanding samples.

5.3.3 s-SNOM measurements

In addition to the far-field optical transmission spectra presented above, near field measurements are conducted utilizing the s-SNOM technique in transmission mode configuration. Thereby the AFM scan is performed on the top side of the SiN film and the near-fields of the hole array are measured through the 30 nm SiN layer (c.f. figure 5.8). All presented s-SNOM measurements utilize the pseudohetordyne detection scheme for interferometric measurements discussed in section 4.2.3 in combination with the Alpha HP OPO source tuned to a wavelength of 1600 nm. The tip tapping amplitude is set to approximately 60 nm and all shown s-SNOM data are demodulated at the third harmonic of the tip tapping frequency. Figure 5.10 displays the measured AFM topography (a), and optical near-field data (b-d) of array configuration 2 in a 30 nm thick gold film with x-polarized incident light. The array period in x-direction, which is relevant for the thin film SPP excitation is in this case is 1250 nm. From the AFM topography, one can clearly identify the individual holes in the array. This is due to the fact that the SiN layer is bend down 15 nm to 20 nm by the force of the tip in the hole regions (c.f. topography profile in figure 5.10 (a)). The plateau at the bottom of the holes proves that the SiN film is still intact after the focused ion beam milling process during the sample fabrication. However, the film can be thinner than 30 nm in the hole regions and the samples must be treated with care during the AFM measurements. Furthermore, the AFM topography reveals some small particles (bright dots) on the surface of the SiN film. The near-field amplitude signal shown in figure 5.10 (b) reveals a standing wave pattern with two maxima along an array period between two holes, which belongs to the $(1, 0)$ mode of the array. Inside the holes, the measured near-field amplitude vanishes. These observations are consistent with earlier non-interferometric a-SNOM measurements [134, 135]. Qualitatively, the measured standing wave pattern is in good agreement with the simulated out of plane near-fields above the film for the $(1, 0)$ mode shown in figure 5.2 (a). Above the small particles already observed in the AFM image, the amplitude signal drops significantly. This is due to the fact, that the distance between the tip apex and the metal film, from which the evanescent fields originate, is increased in this case.

In order to analyze a potential quantitative agreement of the measured data with a standing wave pattern, let us first consider the excitation mechanism of the thin film SPPs in further detail. An x-polarized incident plane wave can excite thin film SPPs at each hole mainly in $\pm x$ direction. Due to the ordering of the holes in an array and the resonant phasematching in x-direction in this case, the SPPs interfere constructively in positive and negative x-direction and form two counterpropagating SPP waves. The interference of the two waves result in a standing wave pattern:

$$E_z(x) = A e^{i2\pi x/p} + A e^{-i2\pi x/p} = 2A \cos(2\pi x/p), \qquad (5.5)$$

with the SPP amplitude A and a periodicity p, which is equal to the SPP wavelength in case of a resonant excitation. The harmonic time dependency of the electric field is omitted here. In theory, this yields an amplitude signal which is proportional to $|\cos(2\pi x/p)|$ and a phase
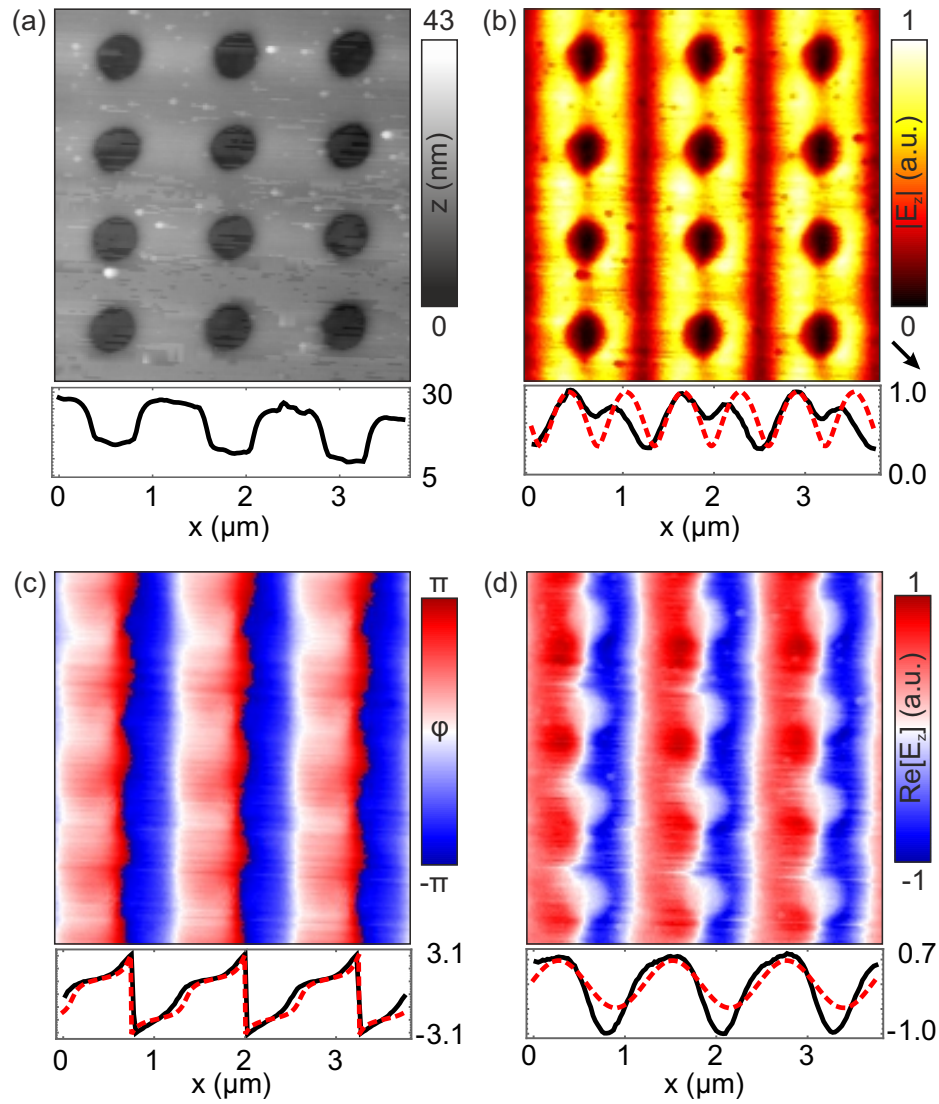
Figure 5.10: s-SNOM measurement of array configuration 2 in a 30 nm thick gold film with x-polarized incident light. (a) Shows the AFM topography. The profile is extracted centrally through the lowest row of holes. (b),(c) and (d) show the amplitude, phase and real-part of the measured electric near-field, respectively. The profiles (black solid curves) are extracted from the lowest four pixel lines of the 2D images. The red dashed curves reveal the model of an asymmetric standing wave given by equation (5.6).

signal, which exhibits alternating phase jumps of $\pm\pi$ separated by a distance of $p/2$, each time the cosine function changes its algebraic sign. However, the measured phase data shows a slightly different behaviour. The expected sharp steps of $\pm\pi$ are smeared out in the phase profile (black curve in figure 5.10 (c)). It turns out, that this behaviour can be reproduced by assuming an asymmetric SPP excitation efficiency:

$$E_z(x) = [A_1 e^{i2\pi(x-x_0)/p} + A_2 e^{-i2\pi(x-x_0)/p}]e^{i\varphi_0}, \tag{5.6}$$

with different amplitudes A_1 and A_2 for the SPPs propagating in $+x$ and $-x$-direction, respectively. The asymmetric SPP excitation efficiency can result from a slight alignment missmatch between the exciting Gaussian beam and the position of the tip. For instance, if the center of the exciting beam lies further in the $-x$-direction from the tip apex position, this will automatically yield a higher amplitude for the SPPs propagating in $+x$-direction at the tip position. This is because the excited SPP amplitude is maximal in the center of the beam, which lies left from the point of signal collection defined by the tip apex. To further fit the asymmetric standing wave to the measured data, a geometric shift x_0 and a global phase offset φ_0 is introduced in equation (5.6). Adjusting the parameters to be $p = 1250\,\text{nm}$, $A_1 = 0.65$, $A_2 = 0.325$, $x_0 = 0.41\,\mu\text{m}$ and $\varphi_0 = 1.18$ yields the red dashed curves in figure 5.10. The resulting phase profile in (c) is in very good agreement with the measurement. For the amplitude (b) and real part (d), the agreement is slightly worse due to an intensity asymmetry on both sides of each hole. This may be attributed to the asymmetric geometry for the collection of the scattered radiation from the tip. Only the scattered radiation in a certain solid angle is collected by the upper parabolic mirror (c.f. figure 4.5). In this case, the direction of the collected scattered radiation is denoted by the small arrow in the lower right corner of the amplitude image in figure 5.10 (b).

As for the far-field spectra, all combinations of array configurations and film thicknesses are measured in the near-field with an incident polarization in the x- and y-direction, respectively. All near-field measurements are performed with an excitation wavelength of $1600\,\text{nm}$. The resulting amplitude and real part data is summarized in figure 5.11 displaying one unit cell of the corresponding array for each measurement in a grid. The measurement data is rotated, such that the exciting polarization is always aligned in horizontal direction. Along the horizontal grid axis, the period of the hole array, relevant for the SPP excitation is increasing from left to right. On the vertical axis, the Au-film thickness is increasing from the top to the bottom. The data of each measurement is generated by averaging several unit cells of a large scale measurement like it is shown in figure 5.10. From the amplitude data in figure 5.11, one can distinguish three different types of SPP excitation patterns in the unit cells depending on the array period and film thickness. The different types of excitation patterns are sectioned by green dashed lines in the grid of amplitude images. In the left section, for small array periods, the high near-fields are concentrated mostly at the sides of the holes. From the real part images, one can clearly identify a dipolar excitation of the individual holes due to the horizontal polarization of the incident radiation. In the middle section between the green dashed lines, the standing wave pattern of the array mode known from figure 5.10 is excited
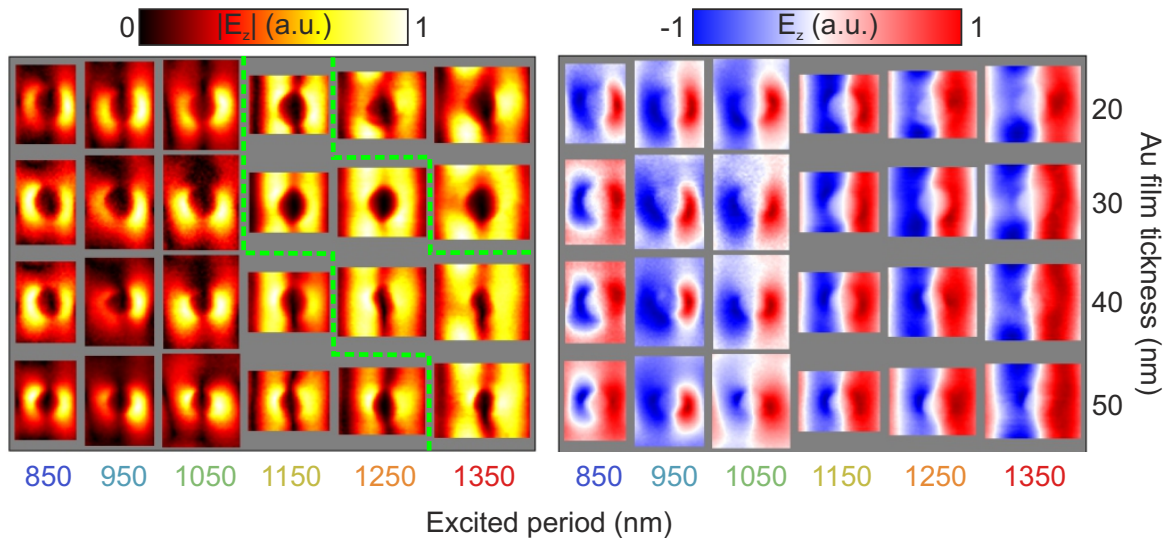
Figure 5.11: Amplitude and real part data of s-SNOM measurements of all array configurations and thicknesses. Each array is measured with the incident polarization along the long and short period axis, respectively at a wavelength of 1600 nm. The measurement data is averaged to one unit cell per measurement and ordered in a grid with varying film thickness on the vertical axis and array period relevant for the excitation on the horizontal axis.

very efficiently. The occurrence of this resonant excitation depends both on the film thickness and the periodicity of the holes in horizontal direction. With increasing film thickness, the resonance is shifting to higher array periods for the constant excitation wavelength of 1600 nm. This corresponds to a blueshift of the resonance with increasing film thickness for a fixed period, which is in accordance with the findings from the far-field measurements in figure 5.9. By comparing the near-field data in figure 5.11 to the far field spectra, it is apparent that the occurrence of the $(1,0)$ mode near-field pattern is slightly shifted to lower wavelength compared to the transmission maximum in the far-field spectra. The same behaviour could be observed from the EELS analysis, where the maximal near-fields occurred at the turning point between the transmission maximum and the following transmission minimum. As already mentioned in this context, this shift is in accordance with a well known redshift of the near-field resonance with respect to the far-field resonance for plasmonic nanoparticles [129]. In the upper right corner of the grid in figure 5.11, i.e. for the largest periods and lowest film thicknesses, the SPP excitation pattern deviates from the standing wave pattern of the $(1,0)$ mode. This may result from an additional excitation of the array mode along the short (vertical) axis of the hole array. Potentially also the $(1,1)$ mode could be already weakly excited in this case.

Plasmonic slot waveguides

The concept of plasmonic waveguides has already been introduced in section 2.3.5. The key benefit of plasmonic waveguides is the tight lateral mode confinement, which makes them attractive as building blocks for integrated nanophotonic circuits. A very promising candidate in this context is the plasmonic slot waveguide (PSW) [69, 70] or the closely related two-wire transmission line [79]. Figure 6.1 includes a schematic representation of a PSW in (a) and a plot of the transverse mode profile of the electric field intensity gained from a 2D mode analysis by finite element method calculations in (b). The PSW comprises a narrow, rectangular slot in a thin metal film [10, 73, 136] featuring a guided mode, which is strongly confined to the slot region.
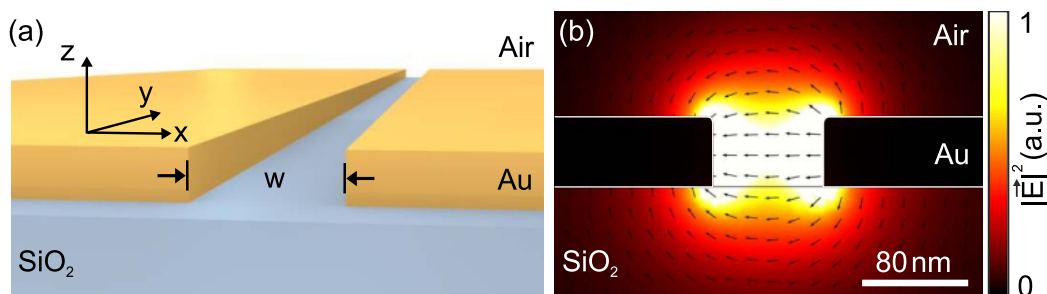
Figure 6.1: (a) Schematic representation of a PSW. (b) Calculated intensity distribution of the guided plasmonic mode in an 80 nm wide PSW in a 50 nm thick gold film . The black arrows indicate the orientation of the transverse electric field component. Taken from [21].

The near-field characterization of different types of plasmonic waveguides via s-SNOM in combination with the pseudoheterodyne detection has already been shown in literature [6, 7, 20, 137–139]. The key benefit of this characterization method is the interferometric detection, which allows to measure both the amplitude and phase of the vertical field component of the guided mode. The complex near-field data allows to extract the effective mode index n as well as the mode propagation length L. The effective mode index relates the SPP propagation constant β of the waveguide to the free space wavevector: $n = \beta/k_0$. Furthermore, s-SNOM

can be applied to study the functionality of plasmonic coupling structures to convert far-field radiation to the PSW-mode, which has been done for different dipole antenna couplers in ref. [20].

In this chapter, PSWs and different couplers to excite the PSW mode from the far-field are characterized by near-field measurements utilizing the NeaSNOM explained in section 4.2. In the first section, the focus lies on a quantitative analysis of the effective mode index and the propagation length via transmission mode s-SNOM measurements of PSWs in single- and poly-crystalline gold films respectively. In this context, a coupler design from reference [20] and a new coupler design are utilized for the excitation of the PSW mode via linear polarized light from the far-field. The descriptions in this section are partly identical to the descriptions in the related publication in Optics Express [21]. Furthermore, I want to emphasize, that many ideas for experimental details concerning the sample fabrication and near-field measurements utilized in this section were elaborated in close collaboration with Matthias Liebtrau during the time of his Master thesis [140]. In the second section, a special coupler design for the directional coupling to two PSWs is investigated via transmission mode s-SNOM measurements. The measurements proof the selective excitation of the PSWs depending on the helicity of the incident circularly polarized light onto the coupler. Especially the near-field phase data is beneficial for the understanding of the coupler functionality in this case.

6.1 PSWs in single- and poly-crystalline gold films

A handicap of many plasmonic waveguides that goes hand in hand with the tight transversal field confinement is the limited mode propagation length. Typical experimental values range between several microns and tens of microns for optical frequencies [20, 22, 24]. A significant contribution to the damping of the guided SPP modes can be attributed to Ohmic losses inside the metal. Other possible loss channels are connected with optical scattering from fabrication imperfections and leakage radiation into the substrate. A possible solution to overcome the limitations resulting from the rather short propagation lengths is to interface plasmonic waveguides with low loss dielectric waveguides [16, 139]. Another approach to optimize the performance of plasmonic waveguides and plasmonic nanostructures in general is to improve the structural and intrinsic material quality of the utilized metallic film. The ultimate improvement of the material quality is represented by a single-crystalline metallic film with no disturbing grain boundaries. However, the preparation of suitable single-crystalline gold films, presented in section 3.1.2, involves considerably higher experimental effort compared to the evaporation of poly-crystalline gold films. For instance, the chemical synthesis of the single-crystalline flakes is time consuming and critically dependent on the experimental conditions and quality of the applied chemicals. Additionally the yield of flakes, which are actually usable for further processing through focused ion beam milling i.e. flakes that have the desired thickness and sufficient lateral size, is rather low. The selection of the flakes in order to match these requirements is another time consuming step, since it involves

characterization by optical microscopy and atomic force microscopy. This may raise the question if the fabrication of single-crystalline plasmonic structures is always profitable, i.e. if the impact of the material quality on the performance of plasmonic devices justifies the additional effort. Surprisingly, quantitative comparisons of the SPP propagation length between single-crystalline and poly-crystalline films are rarely present in the literature [37, 141, 142]. The only quantitative comparison for guided plasmon polaritons is available for silver nanowires [24, 25]. This section addresses this issue and provides a quantitative comparison of PSWs in single-crystalline and poly-crystalline gold films via interferometric near-field characterization. PSWs with variable gap sizes down to 50 nm are investigated via s-SNOM measurements in transmission mode configuration. The effective mode index and the propagation length of the guided mode in the PSWs is extracted from the experimental near-field data by a 2D complex fit. The experimental results are compared to numerical 3D finite element calculations.

6.1.1 Samples

The two different types of gold films are fabricated by thermal evaporation and chemical synthesis according to sections 3.1.1 and 3.1.2, respectively. To enable a reliable quantitative comparison between the two materials, both films are fabricated with the same thickness of 50 nm on glass substrates. However, the two sample systems have thin layers of two different materials between the gold film and the glass substrate. In case of the thermally evaporated films, a 2 nm layer of chromium ensures the adhesion to the substrate. For the single-crystalline samples, an additional layer of 15 nm indium tin oxide (ITO) lies between the gold and the glass substrate. The electrical conductivity of the ITO layer ensures the compatibility of the samples with scanning electron/ion microscopy, while preserving optical transparency for near-infrared wavelengths. In both film types, the PSWs are patterned by focused ion beam milling (c.f. section 3.2) with a current of 1.5 pA, which is close to the lower limit of the ion microscope. This very low current, enables the smallest possible diameter of the focused ion beam and thus the best resolution for the patterned structures. These settings allow for patterning PSWs of widths down to 40 nm in single-crystalline films and a reliable and reproducible width of 50 nm in the thermally evaporated poly-crystalline film. The reduced patterning accuracy in poly-crystalline films results from grains at the surface and differently oriented crystallites in the film, which laterally alter the etch rate of the ion beam [23]. Figure 6.2 shows SEM images of PSWs and far-field couplers milled in single- and poly-crystalline films.

For the 40 nm slot in poly-crystalline gold in Figure 6.2 (a), it is apparent that at some positions there is residual metal in the slot. For the 50 nm slot in poly-crystalline gold in Figure 6.2 (b) the whole slot region is free from residual metal. However, the slot width is slightly varying due to the alternating etch rate mentioned above. The best patterning results are achieved for PSWs in single-crystalline gold, exemplarily shown for a 40 nm slot in figure 6.2 (c). No residual metal can be found inside the slot and the width is extremely homogeneous along the whole length of the slot.
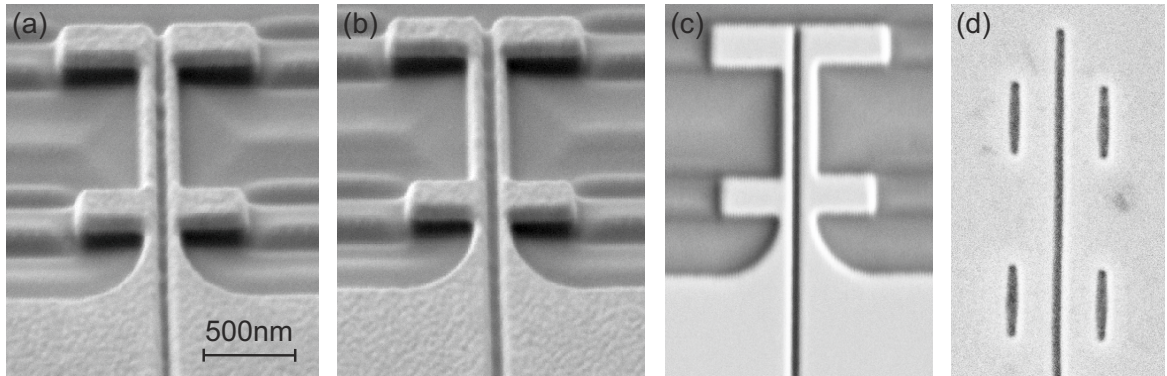
Figure 6.2: SEM images of PSWs and coupler structures in single- and poly-crystalline films. (a) and (b): 40 nm and 50 nm PSWs in poly-crystalline gold with the two-wire transmission line coupler design. (c): 40 nm PSW in single-crystalline gold. (d): 50 nm PSW in single-crystalline gold with a slot antenna coupler design.

PSWs of different slot widths between 50 nm and 170 nm are prepared in single- and poly-crystalline films for a parametric study via near-field measurements. Each waveguide is fabricated with a resonant coupler at one end, which efficiently excites the guided mode upon illumination with a linearly polarized input beam. For the set of waveguides in the poly-crystalline gold film, the geometry of the coupler is adopted from reference [20]. The coupler and its parameters are schematically depicted in 6.3 (a) and the parameter values are summarized in the left table in 6.1.
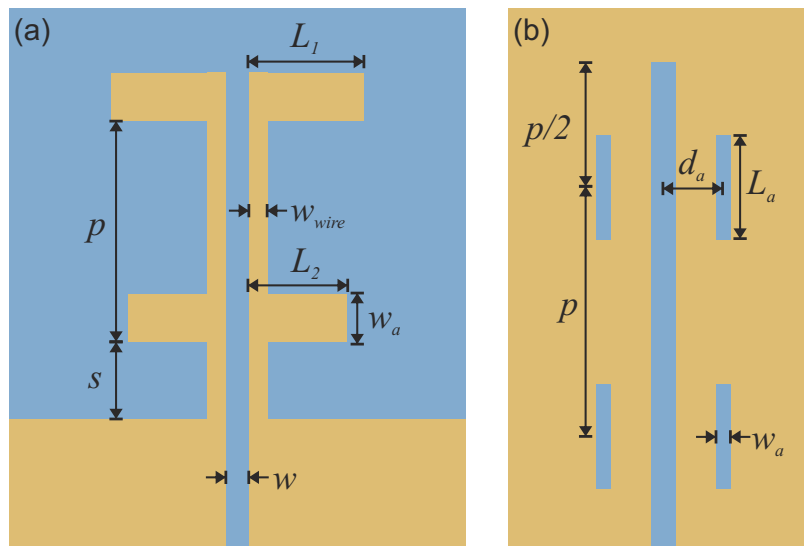
Figure 6.3: Schematic representations of the TL coupler used for the poly-crystalline samples (a) and the SA coupler used for the single-crystalline samples (b). The delineated geometrical parameters are given in table 6.1.

TL coupler	
w_{wire}	80 nm
w_{a}	210 nm
L_1	500 nm
L_2	420 nm
s	435 nm
p	970 nm

SA coupler	
w_{a}	60 nm
L_{a}	420 nm
d_{a}	250 nm
N	4

SA coupler periods	
w	p
50 nm	980 nm
60 nm	1020 nm
80 nm	1040 nm
100 nm	1060 nm
120 nm	1070 nm
150 nm	1080 nm

Table 6.1: Geometrical parameters of the TL coupler and the SA coupler. In case of the SA coupler, the period p of the antennas is adapted to the different effective mode indices caused by different width of the PSWs.

The coupler consists of two transmission line wires comprising a slot in between, which continues as the PSW at the end of the coupler. In the following, this coupler design is referred to as transmission line (TL) coupler. On the two-wire transmission line, a guided plasmonic mode is excited via a pair of rod antennas on each side. The period p of the rod antennas along the wire axis is chosen according to the effective mode index of the transmission line such that the excitations of the individual rod antennas interfere constructively for the design wavelength of 1550 nm. The lengths of the antennas are defined, such that the TL coupler is resonant i.e. has its largest coupling efficiency at 1550 nm upon illumination with linarly polarized light along the long axis of the rod antennas. The presence of the transmission line slightly shifts the resonances of the individual rod antennas compared to freestanding ones. The magnitude of this shift is different for the two rod antennas at the edge of the transmission line than for the antennas in the middle of the transmission line. To compensate for this effect, the two antennas on each transmission wire are designed with slightly different length L_1 and L_2.

Figure 6.4 (a) shows the AFM topography, as well as amplitude and phase data of a transmission mode s-SNOM measurement of the TL coupler at a wavelength of 1520 nm. This wavelength is used instead of the coupler design wavelength (1550 nm) for all following measurements, because the employed OPO light source produces a large amount of noise at 1550 nm in the frequency range of the the higher harmonics of the tip oscillation, which directly transfers to the measured near-field signals. The tapping amplitude in the measurements is roughly 60 nm and the incident linear polarization is oriented along the long axis of the rod antennas. The signal is extracted according to section 4.2.4 using the third demodulation order. The data clearly reveal the excited dipolar resonance of the individual rod antennas by the amplitude maxima at the poles of the antenna and a phase jump of π across the middle of the antenna. The phase difference between the two positions where the antennas are connected to the transmission wire on each side is 2π, confirming constructive interference of the antenna excitations into the propagating mode of the transmission line. There is a phase difference of π between the surface waves propagating along the two opposing transmission
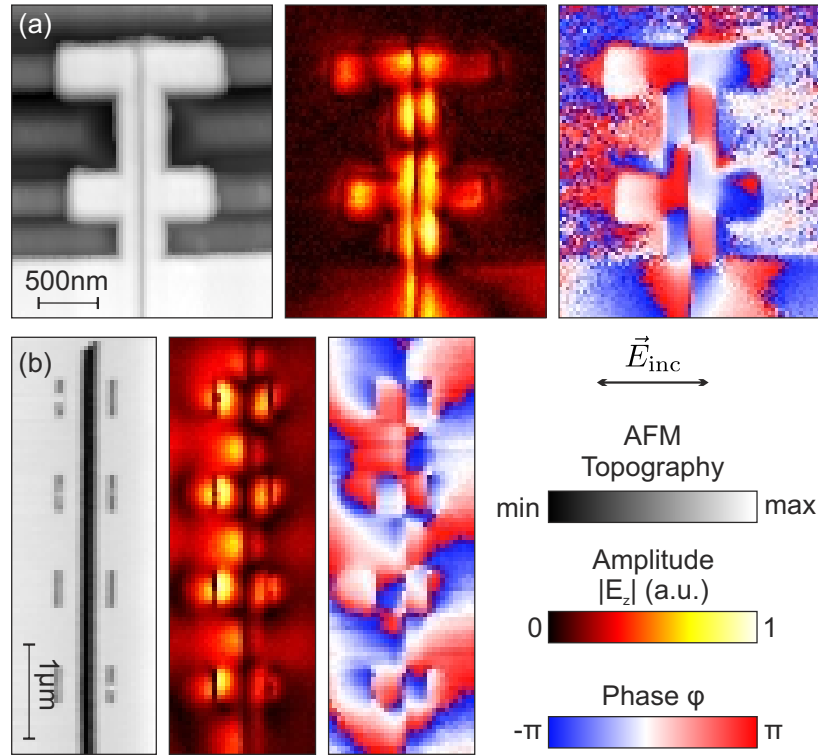
77

Figure 6.4: AFM, near-field amplitude and phase data from transmission mode s-SNOM measurements of the TL coupler (a) and the SA coupler (b). The linear polarization direction $\vec{E}_{\text{inc}}$ of the excitation beam is oriented perpendicular to the slot waveguide in both measurements.

line wires, matching the asymmetric nature of the PSW mode, which also exhibits a phase jump of π across the slot. This enables an efficient transmission from the TL coupler to the PSW mode. However, slight transmission losses may result from a small impedance missmatch at the connection due to a slightly higher effective mode index in the transmission line compared to the PSW. A tapering at the junction from the transmission line to the PSW is applied in some cases to reduce this effect (c.f. figure 6.2 (a-c)).

The FIB structuring of the TL coupler involves sequential patterning of individual rectangular structures, which are separately written from the center to the outside according to figure 3.3 (b). The alignment of all rectangles with respect to each other is essential for the final performance of the coupler. Therefore, tiny drifts of the sample or the ion beam during the writing process have a harmful impact on the coupling efficiency. For the patterning in the poly-crystalline gold film, the beam stability and sample position are sufficient to fabricate high quality TL couplers. However, for the single-crystalline films, the stability is significantly lower. This may be attributed to charging effects on the sample surface. In contrast to the poly-crystalline films, the single-crystalline flakes cover only a small fraction of the sample surface and are isolated from each other. Despite the ITO layer below the flakes, the conductivity for charge neutralization during the patterning process

is less compared to the closed poly-crystalline films. This may lead to a surface charge on the sample, which potentially influences the ion beam trajectory and disturb the patterning process. The disadvantage of the TL coupler design in combination with the single-crystalline flake is revealed by comparing the TL coupler geometries in figures 6.2 (b) and (c). The geometrical deviations from the design are significantly more pronounced for the TL coupler patterned into the flake. Therefore another coupler design is used in combination with the single-crystalline films. It consists of resonant slot antennas in close proximity to the PSW (c.f. fig 6.2 (d)). In the following, this design is referred to as slot antenna (SA) coupler. The total area of gold, which has to be removed during fabrication of the SA coupler is is immensely reduced compared to the TL coupler design. Consequently, the patterning time reduces to a few tens of seconds for the SA coupler compared to about ten minutes for the TL coupler, which minimizes the impact of the instabilities on the structure quality.

A schematic representation of the SA coupler with the geometric parameters is given in figure 6.3 (b) and the related parameter values are given in the middle and right table in 6.1. The functionality of the SA coupler relies on the individual resonant excitation of the slot antennas. To achieve this, the incident light has to be polarized along the short axis of the slot antenna in accordance with Babinet's principle. Upon resonant excitation, the charge accumulates predominantly in the areas adjacent to the long axis of the slot antennas. This can be estimated from the near-field amplitude image in figure 6.4 (b). Charge accumulations in a metallic film lead to an out-of-plane near-field component, which is the primary measured quantity in s-SNOM (c.f. section 4.2.5). The proximity of the slot antennas to the PSW on both sides generates an overlap of the charge accumulations at the antennas with the waveguide mode pattern. This enables an efficient excitation of the PSW mode via the antennas. A phasematched array of four antennas on each side leads to an accumulation of the individual excitations, which further enhances the coupling efficiency. Since PSWs of different width exhibit different effective mode indices, the periodicity of the slot antennas is adapted in each case according to the right table in 6.1. The near-field phase image indicates a phase difference of approximately π across the slot antennas, as expected for the resonant excitation. The phase shift across the waveguide is also approximately π as required by the symmetry of the fundamental PSW mode.

6.1.2 s-SNOM measurements of the PSW mode

The s-SNOM measurements of the PSW samples are performed in transmission mode configuration. A simplified scheme with respect to figure 4.5, reduced to the interferometric setup of the NeaSNOM in transmission mode is recovered in figure 6.5 (a). The Alpha-HP from *Stuttgart Instruments* tuned to a wavelength of 1520 nm is used as an external laser source according to section 4.2.2. The incident power onto the sample is approximately 1.5 mW, corresponding to a power of roughly 30 mW at the input of the NeaSNOM system. The waist radius of the Gaussian beam at the sample surface is determined to be approximately 4 μm by a knife edge measurement [140]. The samples are placed in the microscope, such that the PSWs are oriented along the y-direction given in figure 6.5 (b), showing a light
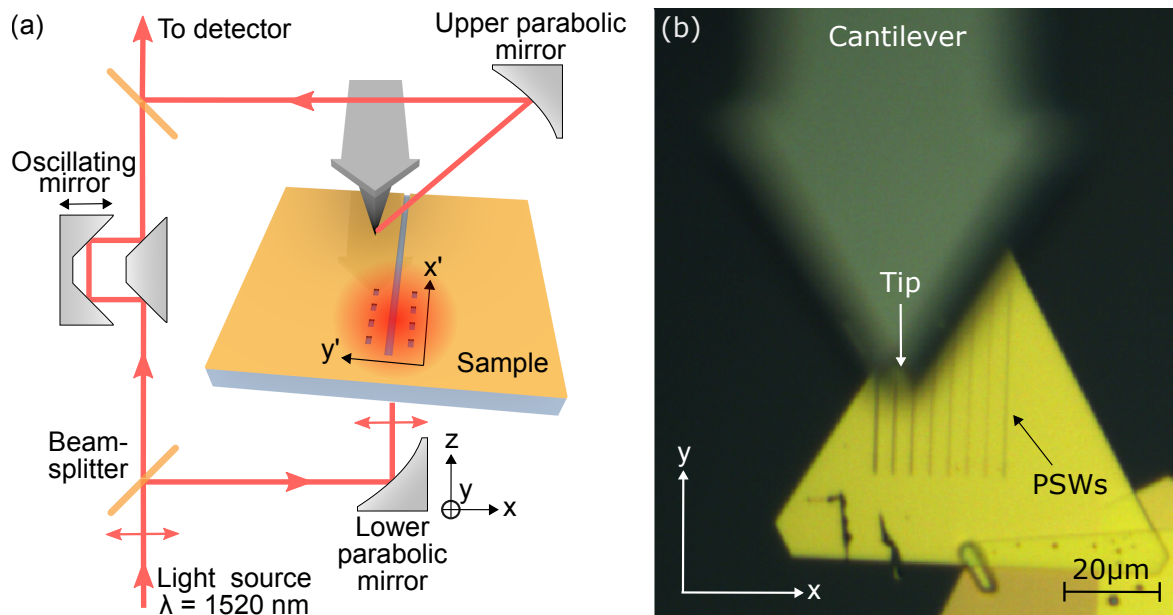
Figure 6.5: (a) Schematic view of the two beampath of the Mach-Zehnder interferometer for s-SNOM measurements in transmission mode configuration. (b) Camera image of the top view optical microscope in the NeaSNOM system. The single-crystalline gold flake with the PSWs lies below the cantilever. The PSWs are roughly oriented along the y-direction.

microscope image from an internal top-view optical microscope camera of the NeaSNOM. The flake with the PSWs of interest resides below the tip. The PSWs are ordered in a row with a pitch of 4 µm and the couplers are located at the bottom of the PSWs. Due to placement by hand, the error on the orientation along the y-direction can amount to a few degree. This small deviation can be corrected by adjusting the direction of the raster-scan accordingly with an accuracy of 1°. Thereby the fast axis is chosen to be parallel to the waveguide in x'-direction (c.f. figure 6.5 (a)). The incident beam is polarized along the x-direction (approximately y'-direction) to resonantly excite the respective coupler and thus efficiently launch the PSW mode, which propagates along the slot in x'-direction. The scan size is 2 µm in y'-direction and 15 µm to 20 µm along the x'-direction. The resolution is set to 25 nm per pixel and the averaging time per pixel is set between 10 ms and 20 ms such that the total raster-scan is taking approximately 30 min to 45 min. The resulting scan speed is below 2 µm/s in order to prevent a rapid degradation of the tip quality.

As discussed in section 4.2, the raster-scan during the measurement is implemented by moving the sample in order to maintain a fixed alignment of the upper parabolic mirror with respect to the tip. For a static position of the illuminating lower parabolic mirror, this leads to a moving excitation spot with respect to the sample and the coupling structures exciting the waveguide mode. In this scenario, the excitation efficiency drops during a scan along the waveguide away from the coupler, due to the finite size of the excitation spot of roughly 4 µm. To prevent this, the NeaSNOM can be operated in a synchronized mode, which enables a

movement of the lower parabolic mirror via slip stick actuators, that is coupled to the sample movements during the scan. This synchronization enables a measurement of the PSW mode over tens of micrometers along the waveguide, preserving a constant excitation efficiency. However, the movements of the lower parabolic mirror affect the measured near-field phase by alternating the optical path of the interferometer arm, which includes the sample. This leads to an additional phase, which depends on the position of the lower parabolic mirror i.e. the lateral position of the raster-scan.

Mirror movements in y-direction, perpendicular to the axis of the incident beam onto the parabola do not affect the optical path length. This can be explained by the inherent properties of the parabolic mirror. Due to Fermat's principle, any incoming ray parallel to the optical axis of the parabola travels the same optical path length to the focus on the sample. Thus, movements of the parabola in y-direction shift the focus accordingly, but do not alter the phase. In contrast, mirror movements in x-direction alter the optical path length between the first beamsplitter of the Mach Zehnder interferometer and the lower parabola (c.f. figure 6.5). The imposed phaseshift is given by:

$$\Delta\varphi(x) = k_0 x, \tag{6.1}$$

where k_0 is the free space wavevector of the utilized laser source and x is the position coordinate according to figure 6.5. The vertical beampath from the lower parabola to the sample is not altered, since the the mirror is only performing lateral movements in x-y-direction during the raster-scan. As already discussed above, the fast scan axis is chosen to be parallel to the waveguide by rotating the scan axis in the NeaSNOM control software. The imposed phaseshift given by equation (6.1) can be transformed into the rotated coordinate system with coordinates x' (fast axis) and y' (slow axis) of the raster-scan:

$$\Delta\varphi(x', y') = k_0(x' \cos(\alpha) - y' \sin(\alpha)), \tag{6.2}$$

where α is the angle between the x axis and the x' axis and takes values of roughly $90°$ when the fast axis is chosen parallel to the waveguide. The recorded phase raw data during a synchronized s-SNOM measurement can be corrected by a pixelwise subtraction of the imposed phaseshift depending on the lateral (x', y') pixel coordinate:

$$\varphi(x', y') = \varphi_{\text{raw}}(x', y') - \Delta\varphi(x', y') \tag{6.3}$$

According to equation (6.2), only minor corrections are necessary along the x'-axis parallel to the waveguide and major corrections are applied on the y'-axis perpendicular to the waveguide for $\alpha \approx 90°$. This sample orientation is intentioned to minimize residual systematic errors of the correction on the measured phase gradient along the waveguide, which is important to extract the effective mode index later in the data analysis.

Figure 6.6 exemplarily displays data of an s-SNOM measurement of a 60 nm wide PSW in single-crystalline gold. The illumination wavelength is 1520 nm and the tapping amplitude is roughly 60 nm. The near-field signals are demodulated at the third harmonic of the tip
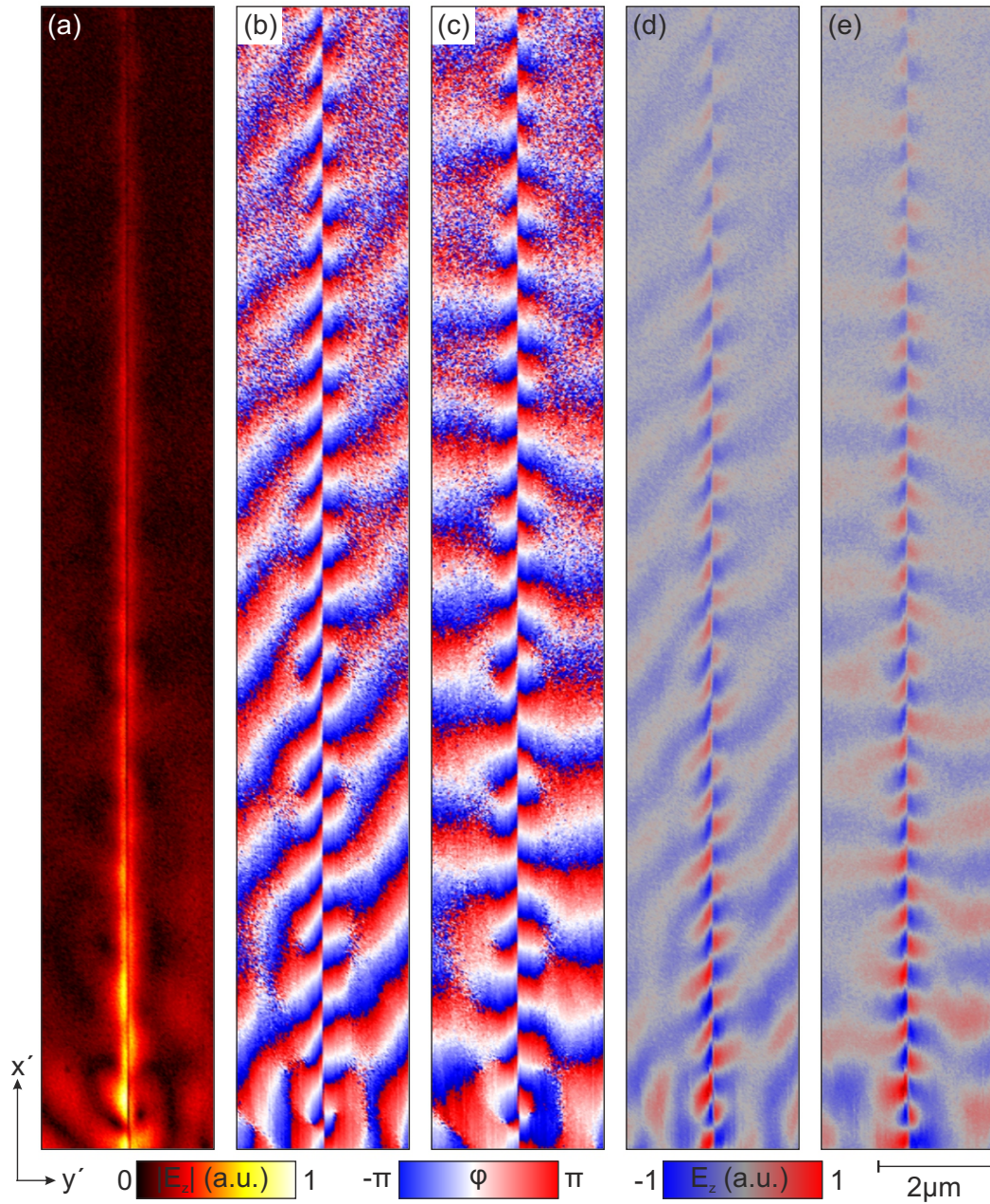
Figure 6.6: Transmission mode s-SNOM images of a 60 nm wide PSW in single-crystalline gold demodulated at the third harmonic of the tip oscillation frequency measured at a wavelength of 1520 nm with synchronized illumination. (a) Near-field amplitude $|E_z|$. (b) Raw near-field phase φ_{raw} and (c) corrected near-field phase φ. (d) Raw real part $E_{z,\mathrm{raw}}$ and (e) corrected real part E_z.

tapping frequency. The SA coupler, which excites the waveguide mode is not included in the scan region and lies further below in negative x'-direction. The excitation is hold fixed on the coupler via synchronization of the lower parabolic mirror during the measurement. The near-field amplitude $|E_z|$ shown in figure 6.6 (a) is tightly confined around the slot in y'-direction and decreases during mode propagation along the x'-direction. As expected from the calculated transverse electric field distribution depicted in figure 6.1 (b), the measured out-of-plane field component $|E_z|$ is small in the middle of the slot. Figure 6.6 (b) shows the raw near-field phase φ_{raw}. The linear increase of the phase along the slot indicates the propagation of the PSW mode in x' direction. However, the phasefronts of the propagating waves are tilted due to the synchronized movements of the lower parabola, which leads to the additional phase $\Delta\varphi$ along the x-direction (approximately y'-direction) according to equation (6.2). Figure 6.6 (c) shows the corrected near-field phase φ governed by applying the phase correction defined by equation (6.3) to the raw phase data in (b). After the correction, the phasefronts are horizontally aligned, as expected for the propagating waves in vertical (x') direction. The same observations can be made by comparing the raw real part $E_{z,raw}$ shown in (d) and the corrected real part E_z depicted in (e). The real part and phase data clearly reveal the expected antisymmetric nature of the PSW mode with a phase jump of π across the slot. During mode propagating, one observes a linear phase increase in x'-direction. Beside the PSW mode, which is tightly confined around the slot, copropagating free SPPs on the gold/air interface are present in the peripheral region of the scan further away from the slot.

In order to compare the optical properties of PSWs with different slot widths, the synchronized transmission mode s-SNOM measurement and phase correction discussed in the example above is applied to 50 nm to 170 nm wide PSWs in single- and poly-crystalline gold films. All measurements are performed with an excitation wavelength of 1520 nm and a tapping amplitude of 60 nm to 70 nm. A representative set of these measurements is shown in figure 6.7 including measurements of the narrowest 50 nm and intermediate approximately 100 nm wide PSWs in both film types. Figure 6.7 (a) shows amplitude and phase data of the near-field measurement along the $w = 50$ nm wide PSW in single-crystalline gold, The antenna coupler, which excites the waveguide mode is not included in the scan region and lies further below in negative x'-direction for all measurements. The experimental data for the $w = 50$ nm wide PSW milled into the poly-crystalline gold film is shown in figure 6.7 (b). Comparing the amplitude images of both measurements, it is immediately apparent that the propagation length is significantly shorter for the PSW in the poly-crystalline film. Additionally, one can observe a beating pattern at the PSWs close to the coupler for small x'-values. This is due to the fact that in this region the excitation spot overlaps with the scan area. The excitation, which is polarized mainly perpendicular to the PSW efficiently launches SPPs at the gold-air interface propagating away from the slot edges in positive and negative y'-direction. The interference of these SPPs with the waveguide mode results in the observed beating pattern around the PSW [20]. The beating pattern is more pronounced for the PSW in the poly-crystalline film. This is because here the scan region was defined closer to the coupler and the excitation beam to compensate for the rather poor propagation length. Figures 6.7 (c) and (d) display the amplitude and phase maps of PSWs with a slot width of
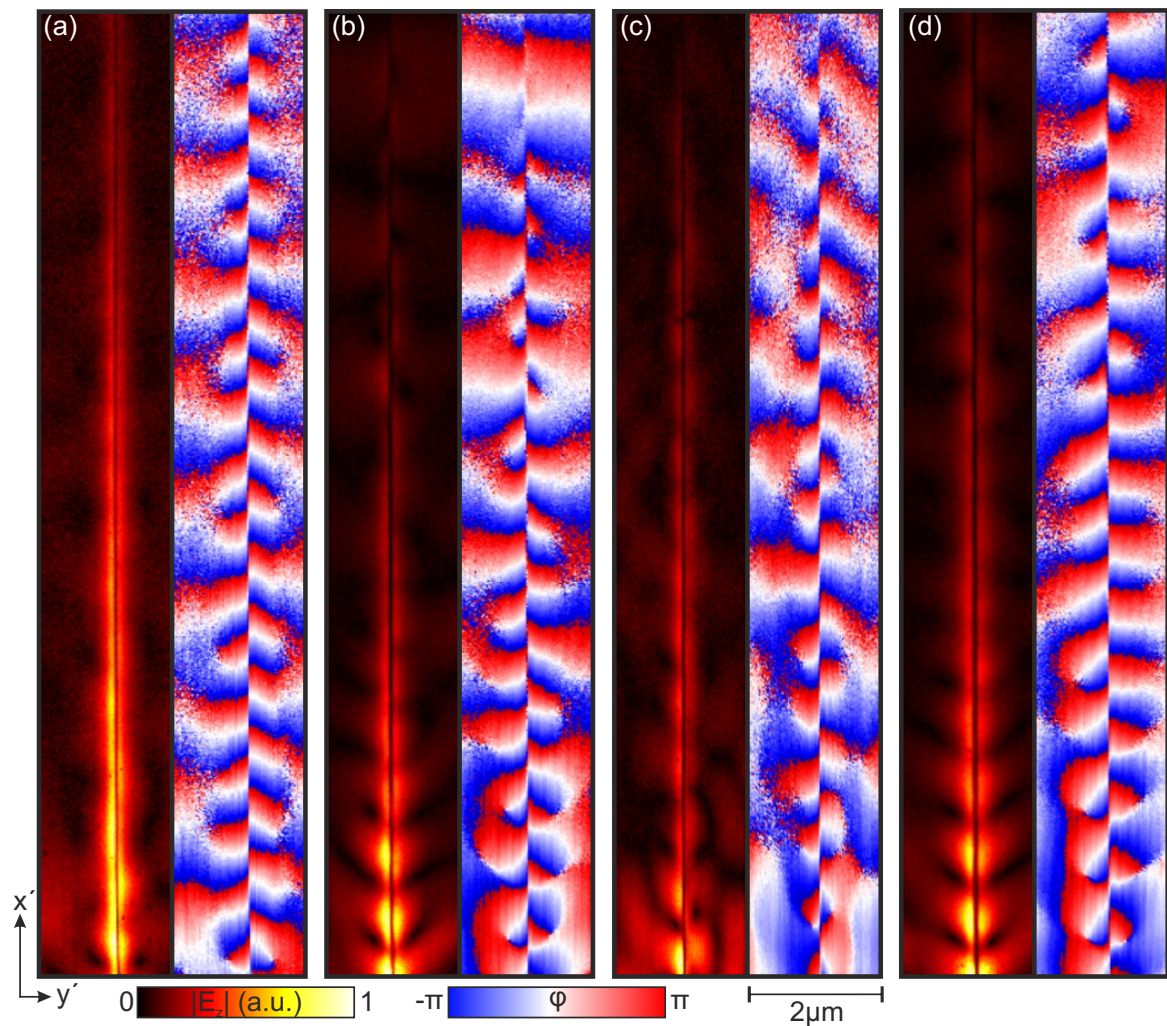
Figure 6.7: Amplitude $|E_z|$ and phase φ data of the measured near-field distribution around PSWs of different gap widths both in single-crystalline and poly-crystalline gold films. 50 nm gap width in single-crystalline gold (a). 50 nm gap width in poly-crystalline gold (b). 94 nm gap width in single-crystalline gold (c). 97 nm gap width in poly-crystalline gold (d). The signals are demodulated at the third harmonic of the tip oscillation frequency and measured at a wavelength of 1520 nm. Adopted from [21].

$w = 100\,\text{nm}$ milled into the single-crystalline gold film and the poly-crystalline gold film, respectively. In contrast to the case of the $w = 50\,\text{nm}$ wide slot, the propagation lengths are comparable for both film types.

In the following, the qualitative observations of the propagation length from above are confirmed by a quantitative analysis of the s-SNOM measurement series on both films. Therefore, the effective mode index n and the propagation length L of the waveguide mode are extracted from the measured near-field distributions, by fitting the following 2D model, which describes the E_z-component of the waveguide mode outside of the gap region, to the data:

$$E_z(x', y') = \begin{cases} E_r \exp[x'(ik_0 n - \frac{1}{2L}) - \frac{y' - y_0}{\kappa} + \varphi_0] & y' - y_0 \geq w/2. \\ -E_l \exp[x'(ik_0 n - \frac{1}{2L}) - \frac{y_0 - y'}{\kappa} + \varphi_0] & y_0 - y' \geq w/2 \end{cases} \tag{6.4}$$

In this model, the center of the slot is located at $y' = y_0$. The gap region is excluded from the fit. Different values for the amplitudes E_r and E_l on the right and left hand-side of the gap are built in the model to account for the slight asymmetry of the near-field amplitude in the measurements, which can be attributed to the specific geometry of the detection optics in the s-SNOM. i.e., the relative positions of the slot with respect to the AFM tip and the collecting parabolic mirror. The opposite algebraic signs on both sides of the waveguide take the phase jump of π across the slot into account and φ_0 represents a global phase. The evanescent decay of the mode perpendicular to the slot in y'-direction is described by the parameter κ.

Figure 6.8 (a) exemplarily shows the E_z component of the experimental data and of the fitted 2D model for the case of the $w = 50\,\text{nm}$ wide PSW milled in the single-crystalline film. The resulting parameters for the propagation length L and the effective mode index n for all measured gap widths are plotted in figure 6.8 (b) and (c), respectively. The error bars result from averaging fit results from the measurement data of the third and fourth demodulation order as well as the forward and backward scan direction, respectively. For the single- as well as the poly-crystalline gold film, the effective mode index decreases with increasing gap size. This relation between lateral confinement and effective mode index is also known from section 2.3.5 and is discussed specifically for PSWs in ref. [70]. In the single-crystalline film, the mode index is slightly smaller than in the poly-crystalline sample. This effect is probably not exclusively caused by the different properties of the gold film. To a greater degree, the shift may result from the different substrate configurations below the gold films, which is 2 nm chromium and glass for the poly-crystalline film and 15 nm of ITO and glass for the single-crystalline film. The lower refractive index of ITO [143] compared to glass might explain the shift, since the mode index of the PSW is very sensitive to the dielectric surrounding in a close region around the slot.

Interestingly, the propagation length shows a non-monotonic behaviour for both film types. In the case of the single-crystalline gold film, one observes a maximal propagation length of $L \approx 6\,\mu\text{m}$ for a gap width of $w = 80\,\text{nm}$. The maximal propagation length for the poly-crystalline gold film is about $L \approx 4\,\mu\text{m}$ and is reached for a gap width of $w = 100\,\text{nm}$. This non-monotonic behaviour can be explained by a trade-off between two different loss channels. With decreasing gap size, a larger fraction of the electric field resides in the metal
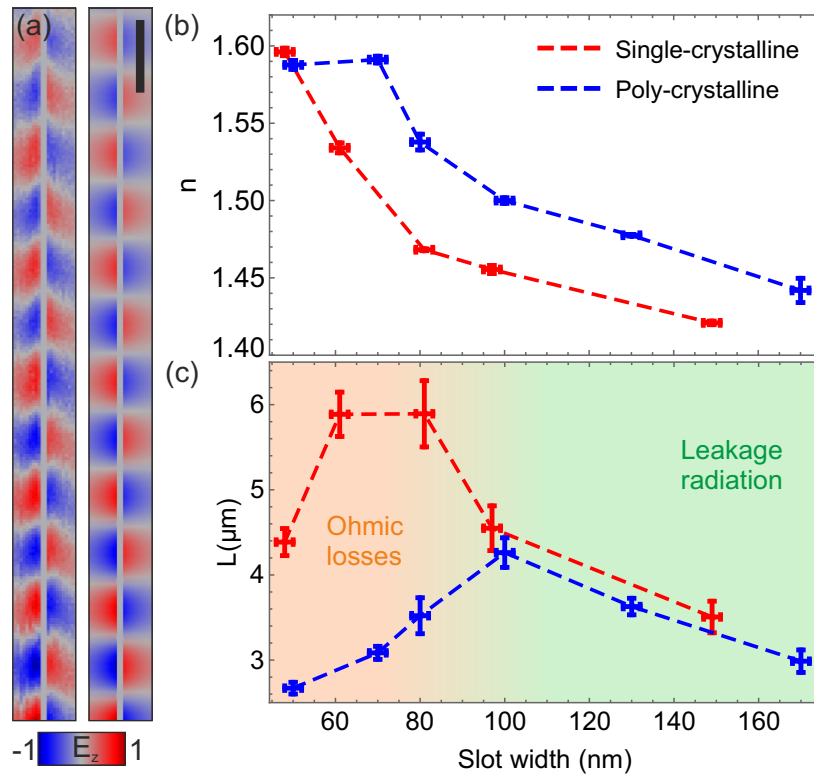
Figure 6.8: Results of the 2D complex fits. (a) Real part E_z around the $w = 50$ nm slot in the single-crystalline film: Measured data (left panel) and fit (right panel). The scale bar has a length of 500 nm. Extracted effective mode indices (b) and propagation lengths (c) both on poly-crystalline and single-crystalline gold for different slot width. Taken from [21].

and the Ohmic losses increase. In this regime, the quality of the gold film is expected to play a crucial role. This is in accordance with the observation that for slot width below $w = 100$ nm the propagation length of the PSWs defined in the single-crystalline gold film is up to a factor two larger than that of the PSWs in the poly-crystalline gold film due to the superior material quality. In contrast, for large gap sizes, Ohmic losses are expected to be reduced. This is because compared to very thin slots, a larger fraction of the electric field of the mode is located in the dielectric parts of the PSW geometry rather than in the lossy metallic parts. Hence, one could naively expect that L should monotonically increase with the gap size. Nevertheless, the fit results reveal a different behaviour, i.e., the propagation length decreases for the largest gap sizes for both film types. The reason for this is leakage radiation, which appears as the effective mode index falls below the refractive index of the glass substrate as well as the effective index of surface plasmon polaritons propagating at the gold-substrate interface. In this case, the waveguide mode becomes radiative. The resulting energy dissipation into the substrate and SPPs provides additional loss channels, decreasing the propagation length of the slot mode. This hypothesis is further supported by the fact that the maximum propagation length for both film types occur at the same effective mode

index of approximately 1.5. The overall shift of the mode indices between the two films leads to a larger specific slot width for emerging leakage radiation for the evaporated gold film. When the PSWs on both films are in the leaky regime for slot width above 100 nm, the propagation lengths are nearly the same, leading to the assumption that leakage radiation losses are dominating.

The experimental results presented above can be reproduced quantitatively by 3D numerical simulations employing a commercial finite element method solver (*COMSOL Multiphysics*). The simulations have been performed and evaluated by Prof. Linden for the publication in Optics Express [21], from which the following description is adopted.

The total size of the computational domain is $1.5\,\mu m \times 20\,\mu m \times 3\,\mu m$ ($x \times y \times z$). The coordinate system is defined according to figure 6.1 (a). To take advantage of the symmetry of the PSW mode, perfect electric conductor boundary conditions are applied to the yz-plane in the middle of the gap. All other boundaries of the computational domain are terminated by perfectly matched layers with a thickness of 750 nm. The 50 nm gold film is sandwiched between the glass substrate below (refractive index n=1.5) and air (refractive index n=1) above. The gap region consists of air. The dielectric function of the gold film is modelled by interpolation of the data provided by Johnson and Christy [59]. The slot waveguide has a length of $18.5\,\mu m$ and is terminated in y-direction on one end by $1.5\,\mu m$ of gold and on the other end by a perfectly matched layer. For reasons of calculation time and memory consumption, the phase-matched slot-dipole-antenna array is omitted and the slot mode is excited at the closed end of the waveguide by a normally incident, x-polarized Gaussian beam from the substrate side. The slot width is varied in a parameter sweep from $w = 40$ nm to $w = 150$ nm in steps of 10 nm. From each of these calculations, the transverse electric field component $E_x(y)$ is extracted along a line profile through the center of the slot in propagation direction (y-direction). The effective mode index and the propagation distance are obtained by fitting a 1D damped harmonic wave to the $E_x(y)$-data (see figure 6.9).
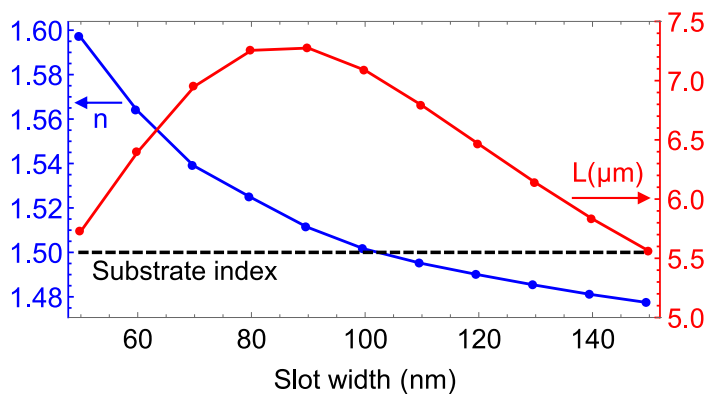
Figure 6.9: Calculated effective index (blue curve) and propagation length (red curve) of the PSW slot mode as a function of gap size. Taken from [21].

The numerical results are in good agreement with the experimental findings for the single-crystalline gold film. In particular, they also show a monotonic decrease of the effective mode index and a maximum of the propagation length for gap sizes around $w \approx 90\,\mathrm{nm}$. As in the experiments, the propagation length strongly decreases once the effective mode index becomes smaller than the refractive index of the substrate. Note that the latter aspect cannot be reproduced with 2D mode analysis calculations, in which leakage of the slot mode into the substrate is not properly taken into account.

6.2 Chiral couplers for the directional excitation of PSWs

A well-controlled and efficient interfacing between free space radiation and the guided mode in the PSW is an important step to utilize PSWs as building blocks for integrated optoelectronic devices. Especially functional couplers with distinct properties dependent on the polarization state of the incident light are promising candidates in this context. For example, a selective coupling into different guided modes or propagation directions has been recently shown [71, 79]. This section focuses on the near-field investigation of a functional coupling geometry, which enables a selective coupling dependent on the helicity of the incident light. The near-field measurements clearly confirm the directionality of the coupler. A further spectroscopic near-field analysis approves the functionality of the coupler in a relatively broad spectral range.

Figure 6.10 (a) shows an AFM image of the investigated sample. It was fabricated by Martin Thomaschewski from the University of Southern Denmark by electron beam lithography and has been investigated by an on-chip detection method of the incoupled light in this context [71]. The structures are made from a 100 nm thick gold layer on a glass substrate. The central element of the coupler geometry is a gold half ring (c.f. top part of figure 6.10 (b)), which transforms into a PSW on both ends of the half ring. The PSWs proceed in an S-shaped curve until they finally end in a straight line, where the on-chip detection took place for the initial purpose of the samples. The relevant parameters of the sample are highlighted in figure 6.10 (b)) and are determined from the AFM measurement. The ring radius is $R = 240\,\mathrm{nm}$, the wire width is $d = 235\,\mathrm{nm}$ and the slot width is $w = 95\,\mathrm{nm}$. Since the AFM image is always resulting from the convolution of the tip shape and the sample topography, the determined value for w is slightly underestimated and the determined value for d is slightly overestimated. The value for $2R$ was extracted from the distance between the two centers of the left flanks of the wires. In this case, the convolution with the tip shape is not hampering an accurate extraction of R, because it only affects the width, but not the position of the flanks.

Depending on whether the incident light onto the coupler is left-handed circularly (LHC) polarized or right-handed circularly (RHC) polarized, either the left or the right PSW is primarily excited. The functionality of the coupler relies on a resonant excitation of the ring, which is connected to the condition [144]
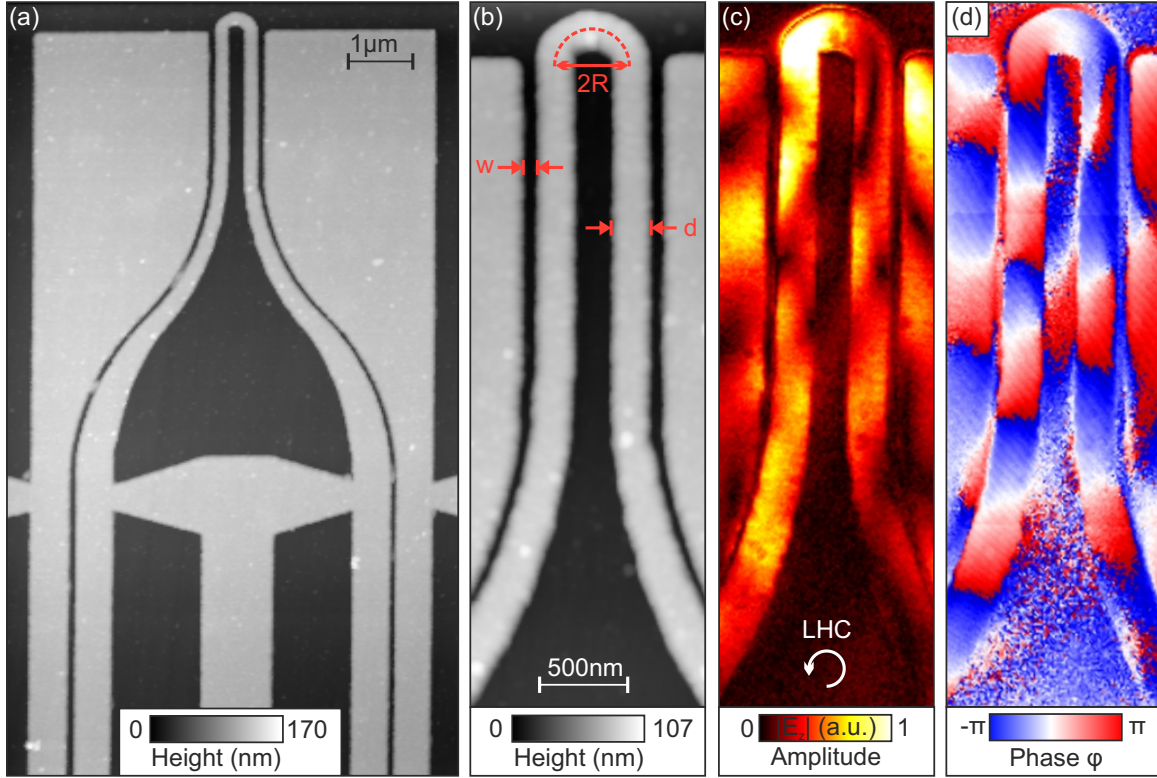
$$\beta = \frac{\sigma}{R}.$$

(6.5)

Figure 6.10: AFM images of the investigated sample (a),(b). The ring radius R, the PSW width w and the width d of the wire forming the ring are marked in the high resolution AFM scan in (b). (c) and (d) show near-field amplitude and phase of a transmission mode s-SNOM measurement with LHC polarized light at a wavelength of 1525 nm.

Thereby, β is the propagation constant of the guided mode along the ring, $\sigma = I_r - I_l$ is the polarization helicity defined by the difference of the LHC and RHC intensity components of the incident light and R is the radius of the ring marked in figure 6.10 (b). The resonance condition in equation (6.5) corresponds to the case when a propagating mode around a full ring acquires a phase of 2π, leading to a resonant circulation of the guided mode around the ring. In case of the half ring coupled to the PSWs on both sides, the resonant excitation is launching the PSW mode on each side depending on the helicity of the incident light. The functionality of the coupler can be verified by s-SNOM measurements, which are performed in transmission mode configuration with the tunable laser source (Stuttgart Instruments Alpha-HP) tuned to a wavelength of 1525 nm. The tapping amplitude is set to approximately 60 nm for all s-SNOM measurments. Again, the measurements are performed in synchronized mode in order to fix the excitation spot to the coupler during the scan. The phase correction according to equation (6.3) is applied to all data shown here. The circularly polarized light is generated by placing a circular polarizer (marked as polarization optics in figure 4.5) in the beampath just before the light is focused onto the antenna coupler array from below

by the parabolic mirror. Due to the limited space inside the NeaSNOM at this position, a circular polarizer (*Thorlabs* CP1L1550) to create LHC polarized light as one optical element is used instead of a combination of a polarizer and a quarter waveplate. The circular polarizer consists of a linear wire grid polarizer and a zero-order quarter waveplate glued together under an angle of $45°$ between the transmission axis of the polarizer and the fast axis of the waveplate. Owing to this design, the whole circular polarizer reduces to a compact planar optical element, which can easily be brought into the beampath at an arbitrary position and spares the need of alignement of the polarizer and the quarter waveplate. However, the compact design is at the cost of spectral flexibility. Due to the zero order waveplate, the helicity σ reduces when deviating from the design wavelength of 1550 nm. For an efficient linear to circular light conversion, the axis of the wire grid polarizer is aligned with the linear polarization axis of the incident beam. To create RHC polarized light, an achromatic half waveplate (*Thorlabs* AHWP10M-1600) is addtionally brought into the beampath behind the circular polarizer. No rotational alignement of the waveplate is needed, since it switches the helicity for any orientation angle of its fast axis.

The resulting data from a s-SNOM measurement of the coupler performed with LHC polarized light is shown in figures 6.10 (c,d) displaying the near-field amplitude and phase, respectively. The near-field amplitude indicates a large excitation of the PSW on the left hand side. The phase image reveals the expected positive phase gradient when following the coupler ring in a counterclockwise manner. The total phase increase along the half ring should amount to π. Furthermore, the phase data along the left PSW reveals the asymmetric nature of the waveguide mode also discussed in the previous section. This behaviour is not present at the PSW on the right hand side. Therefore one can conclude that the plasmonic excitations in the left PSW primarily belong to the PSW mode, while the plasmonic excitations at the right PSW may result from direct SPP excitation at the slot or SPPs excited at the top edge of the film. This effect can be observed even better in the large scale measurements shown in figure 6.11. The sample is measured at a wavelength of 1520 nm with three different polarization states of the exciting beam, namely LHC polarized light in (a), linear polarized light along the horizontal direction in (b) and RHC polarized light in (c).

In the two measurements with circularly polarized excitation, freely propagating SPPs can be launched at any of the illuminated edges of the film. Thereby the initial phase offset of the launched SPP depends on the orientation angle of the edge. The size of the excitation spot is large enough to launch SPPs at the top edge, the PSW edges, as well as the left and right edges of the film. The SPPs launched at the two opposing side edges exhibit a relative phase difference of π and the SPP launched from the top exhibits a phase shift of $\pm\pi/2$ with respect to the side edges as expected for the circularly polarized excitation. The interference of the SPPs launched from all edges forms a 2D standing wave pattern on the whole top part of the gold film, as it can be observed in the near-field amplitude images in (a) and (c). In case of a linearly polarized excitation in (b), SPPs can only be launched at the left and right edges of the sample and at the edges of the PSW, which are perpendicular to the incident polarization. The interference of the SPPs launched from the sample edges and the slot edges lead to a standing wave pattern in the excited upper part of the sample, which can also be observed in
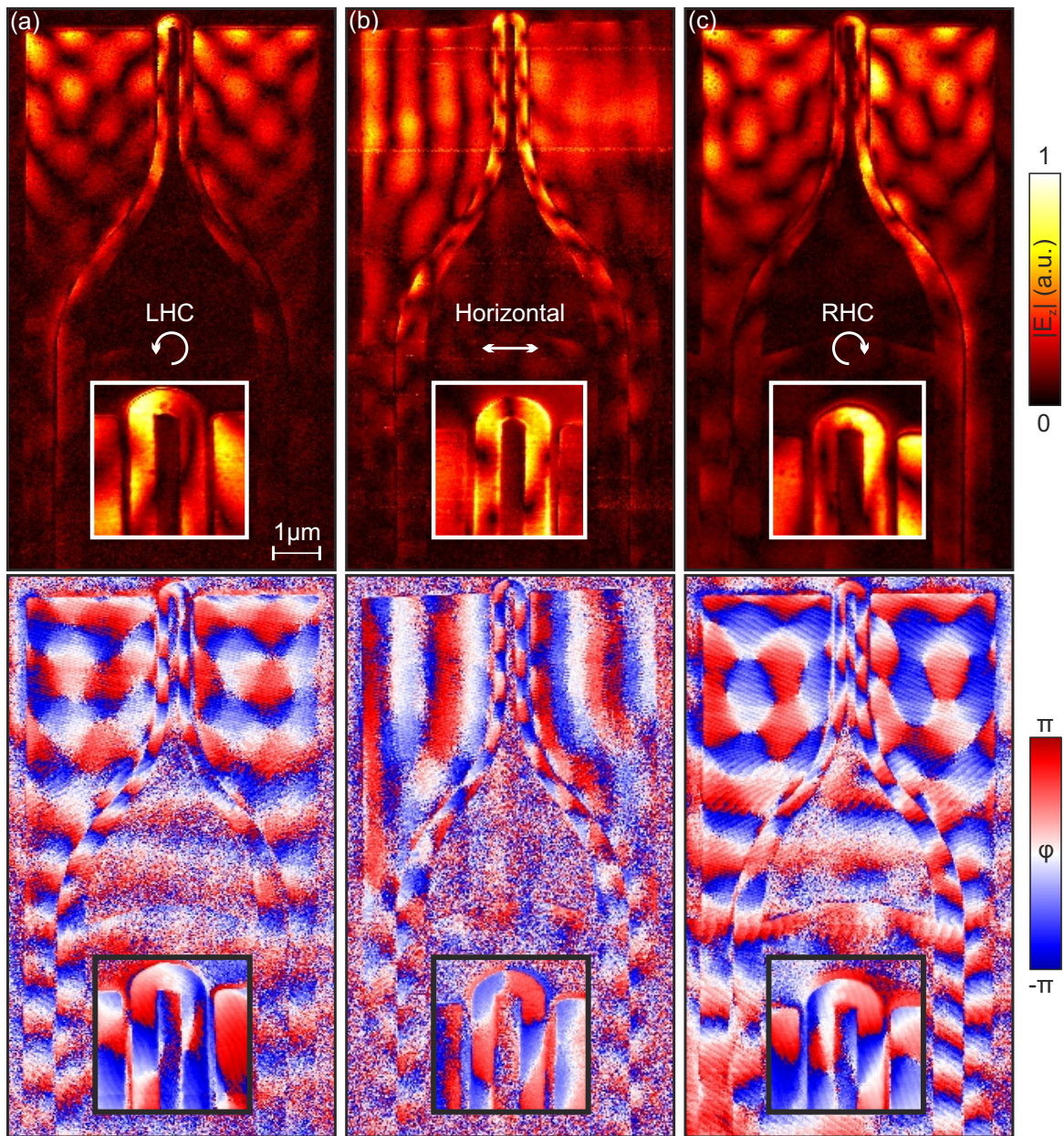
Figure 6.11: Large scale s-SNOM measurements with $\lambda = 1520$ nm with LHC (a), horizontally linear (b) and RHC (c) polarized light. The insets depict high resolution s-SNOM images of the ring coupler.

the amplitude image. Apparently, the standing wave pattern is more pronounced on the left part of the sample, which may be caused by an unintended slight shift of the excitation spot to the left during this measurement.

The insets given in the s-SNOM images shown in figure 6.11 depict high resolution measurements (1.5 μm×1.5 μm, 100×100 Pixels) of the ring coupler, which reveal its polarization dependent plasmonic excitation. Since the scan region is much smaller than the spot size of the excitation beam, the synchronisation of the excitation is omitted in these scans. For the measurements with LHC and RHC polarized light, the amplitude images show strongly directional excitation of the left and right side of the coupling ring, respectively. The propagation direction of the mode on the ring can be deduced from the phase images. In particular, it is indicated by the phase gradient, which is pointing clockwise along the ring for RHC excitation and counterclockwise for LHC excitation. For the linear polarized excitation, a dipolar mode of the ring is excited. The two poles exhibit a strong near-field amplitude in the left and right part of the ring separated by a dark region in the middle of the ring. The two bright regions exhibit a nearly constant phase with a relative phase jump of π with respect to each other, as expected for a dipolar resonance. For all excitation polarizations, the observation of the pure PSW mode excited by the ring is hampered in the upper part of the sample. This is due to the interference with free propagating SPPs launched at the edges. However, the excited PSW mode is still present after propagating through the S-shaped curve and can be observed on the straight parts of the PSW in the lower region of the sample from the large scale measurements. In this region, the direct excitation of SPPs at the edges is suppressed, since the excitation spot is located at the ring. In case it is present, the PSW mode shows the same properties as observed in the previous section. The amplitude images reveal the confinement of the PSW mode around the slot. The phase data exhibit the characteristic asymmetry of the PSW mode with a phase jump of π across the slot. The appearance of the characteristics of the PSW mode discussed above is a clear evidence for excitation of the PSW mode.

Evaluating the three measurements from this point of view leads to the conclusion that the PSW mode appears only in the left waveguide for LHC excitation, only in the right waveguide for RHC excitation and in both waveguides for the linear polarized excitation. The excitation of both PSWs by linearly polarized light can be understood from the fact that the linear polarization can be regarded as an equally weighted composition of LHC and RHC polarized light. In case of the measurements with circularly polarized excitation, free propagating SPPs excited at the top edge of the gold film are still weakly present in the lower part of the sample. However, the SPPs can be clearly distinguished from the PSW mode via the phase images. The free propagating SPPs exhibit a symmetric nature with no phase jump across the PSW. Due to the low intensity of the SPPs compared to the PSW mode, the SPPs can only be observed around the PSWs which are not excited by the coupler, i.e. the right PSW in (a) and the left PSW in (c). This is another evidence for the high directionality of the coupler.

Figure 6.12 shows the results of a spectroscopic near-field analysis of the ring coupler. s-SNOM images are recorded with different excitation wavelength between 1450 nm and 1650 nm in steps of 25 nm. All measurements are performed with an LHC polarized excitation
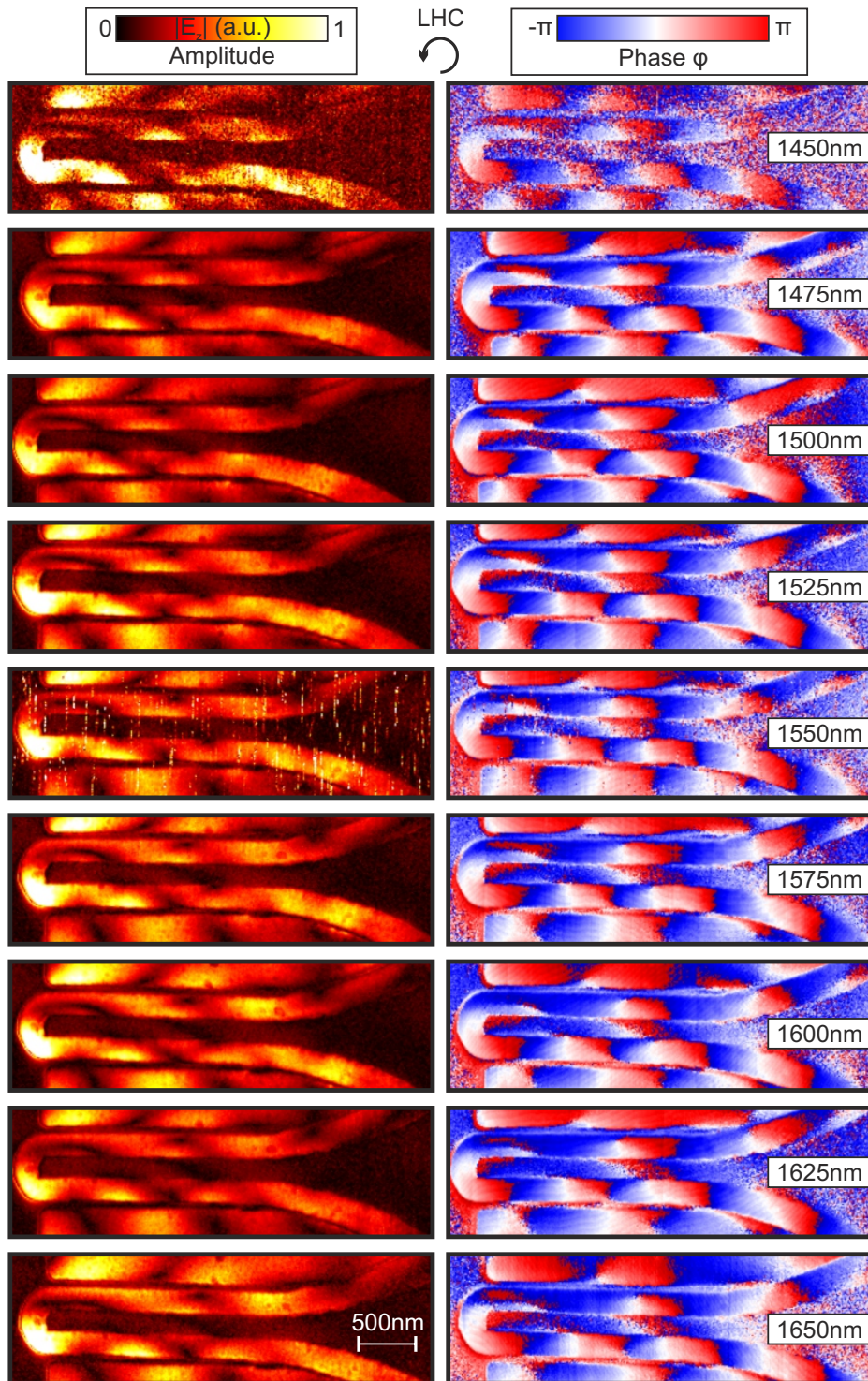
Figure 6.12: Spectroscopic near-field data of the ring coupler with variable excitation wavelength between 1450 nm and 1650 nm in steps of 25 nm. The exciting beam is LHC polarized.

beam. The amplitude images in the left column of figure 6.12 reveal the functionality of directional coupling over the whole measured spectral range concluded from the fact that the lower part of the ring appears bright in all measurements. The directional character of the coupling is also confirmed by the phase images in the right column of figure 6.12. In all measurements, one can observe the positive phase gradient during mode propagation around the half ring in a counterclockwise manner. Furthermore, at the lower PSW, which is primarily excited by the coupler upon LHC polarized illumination, one can recognize the antisymmetric nature of the PSW mode with a phase jump of π across the slot. In contrast, at the upper PSW, which is not or only weakly excited, the asymmetric nature of the PSW mode is absent.

So far, the directionality of the coupler has been qualitatively shown in dependence of the incident polarization. The spectroscopic near-field analysis shows that the directional functionality of the coupler is present over a relatively broad spectral range. However, for a quantitative analysis of directivity of the coupler from near-field measurements, the sample design is not optimal. The propagation distance of roughly 10 μm of the waveguide mode until reaching the final straight part of the PSW is relatively long. Therefore the remaining intensity of the PSW mode on the straight line is rather small due to propagation losses. For the highly directional coupling, where the initial intensity of the PSW mode at the coupler is very high, the PSW mode intensity could be quantitatively extracted from the amplitude images, e.g. from the straight parts of the PSWs in the measurements shown in figures 6.11 (a) and (c). However, to quantify the directionality, one would also have to extract the intensity from the other minor excited PSW, where no intensity of the PSW mode can be observed. Even for the completely nondirectional case with linear polarized excitation shown in figure 6.11 (b) the amount of intensity left in the lower straight part of the PSWs is to small to give reliable quantitative values of the mode intensity. Only the phase data, which is not helpful to extract the directionality, clearly confirms the presence of the PSW mode in this case.

Another approach for a quantitative analysis could be a comparison of the intensity on the bright part of the ring between the different measurements of the spectroscopic analysis. However, this approach is hampered by the fact that the s-SNOM measurements only give the amplitudes in relative units. For instance changing the wavelength or even only retracting and approaching the tip again will change the experimental conditions and may alter the absolute values of the measured amplitudes between different s-SNOM scans. Therefore a reliable quantitative comparison of near-field amplitudes is only possible in the same 2D scan, or by normalizing the measured amplitude at the position of interest to a certain position in the scan area, which is expected to give equal amplitudes for the different scans, e.g. for different polarizations or wavelength during the analysis. Off-resonant rod antennas which have their their resonances at significantly higher frequencies than the excitation frequencies could serve as potential structures for the intensity normalization. Maybe also the intensity of the SPPs excited at the edges of the sample could serve as a spectrally flat normalization quantity.

Another obstacle for a reliable spectroscopic analysis is the circular polarizer, which produces circularly polarized light only at a wavelength of 1550 nm, due to the utilized zero order quarter-waveplate. For all other wavelengths, the circular polarizer produces elliptically

polarized light, i.e. $\sigma < 1$ in equation (6.5).

At the end of this section I want to give a proposal for better suited samples as schematically shown in figure 6.13 to perform a parametric near-field study on the directional coupler. The proposal addresses three main aspects of improving the sample to enable a quantitative analysis of the results in the end. Firstly, the propagation distances from the exciting coupling ring to the final straight parts of the waveguides are reduced. For a near-field analysis a separation of the two waveguides of 1 μm to 2 μm micrometers is better suited. It is large enough to prevent inter waveguide coupling but significantly smaller than for the samples investigated above. This shrinks the propagation distance from the coupling ring to the straight waveguide parts and simultaneously enables a smaller scan area for the s-SNOM measurements, which drastically reduces the measurement time. Secondly, the waveguide type of the ring and the rest of the structure is the same in the proposal, i.e. a PSW in figure 6.13 (a) and a strip waveguide in figure 6.13 (b). This enables an extraction of the propagation constant β on the straight parts of the waveguides, which corresponds to β on the ring. Small deviations between the two propagation constants on the straight waveguides and the ring may arise from self-coupling effects of the propagating mode between the two sides of the ring. The strip waveguide may be even better suited for a quantitative analysis, because the propagation length is higher than for a PSW and free propagating SPPs near the excitation spot are absent. As a last aspect one could fabricate the samples with different radii of the coupling ring for a parametric study. This corresponds to a variation of only one parameter (R) in equation (6.5) instead of dependently altering the two other parameters when changing the wavelength.
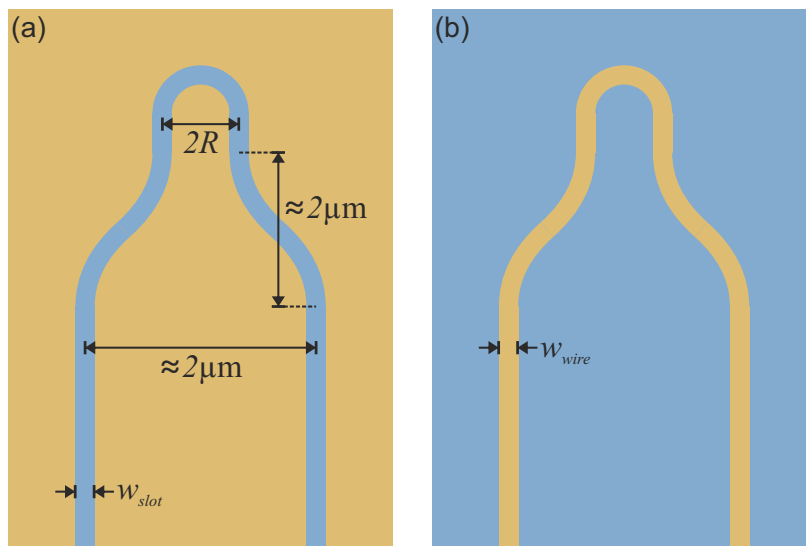
Figure 6.13: Proposals for improved samples towards a quantitative analysis of the coupling directionality via near-field measurements. The new concept can be applied both to a plasmonic slot waveguide (a) and a plasmonic strip waveguide (b).

Nanoporous gold films

Nanoporous gold films can be fabricated by an etching process from thin film alloys of gold and less noble metals [85, 145]. Details of the sample fabrication method utilized in this work are discussed in section 3.1.3. The nanoporous films exhibit randomly distributed near-field hotspots resulting from LSPP excitations inside the sample. These plasmonic hotspots occur for a wide range of excitation frequencies from the near-infrared to the visible regime. The strong LSPP resonances at the sample surface and the large scale fabrication ability makes these structures attractive e.g. for chemical sensing applications [13] and surface enhanced Raman scattering [14, 15].

Here, the spatial and spectral distribution of hotspots on nanoporous gold films is investigated by near-field measurements. In the first section, EELS measurements are presented allowing a near-field characterization from visible to near-infrared frequencies. An extensive EELS study on nanoporous gold and silver films can also be found in literature [146]. The second section shows interferometric s-SNOM measurements in three different configurations regarding the excitation and near-field detection. Non-interferometric s-SNOM measurements on nanoporous samples have already been reported on in reflection and transmission mode configuration [147, 148]. However, section 7.2 provides the first comparison of interferometric s-SNOM measurements in three different configurations, which allows for comparisons between plane wave excitation and excitation by a near-field source. Furthermore, the transmission mode measurement reveals new insights about the scattering of plasmons through the thin nanoporous network.

7.1 EELS measurement

The sample, which is investigated by EELS in the following has been fabricated according to section 3.1.3 with the following parameters: The fraction of gold in the initial film was 6 karat (25 % purity) and the film resided on the 68 % nitric acid for 17 h. For the purpose of TEM compatibility, a small piece of the fabricated nanoporous film is transferred directly onto a Cu 200 mesh carbon grid from *Quantifoil Micro Tools GmbH*, which serves as an

electron transparent substrate. The applied fabrication parameters lead to relatively large pore sizes up to several hundreds of nanometers, which can be seen in the STEM image of the sample in the upper left panel in figure 7.1. From the STEM image, it is also apparent, that the nanoporous film is thinned to a degree such that there exist complete holes in the film. Inside these holes, the electron beam can be transmitted without scattering at the material, which enables an EELS analysis in these regions.

An EELS measurement is performed on a representative square scan region with a size of 700 nm × 700 nm . The scan resolution is 10 nm/pixel and the energy resolution of the spectrometer is 16 meV. As already discussed in section 4.1, the actual energy resolution is determined by the width of the ZLP and is estimated between 0.1 eV and 0.15 eV. The EELS raw data is modified by three steps of data analysis. Firstly, the EEL spectra in all lateral pixels are aligned by overlaying the ZLP. As a second step, a mask is applied to the data, setting all pixels to zero, where the total amount of transmitted electrons is below 70 % of the average transmission. The masked region is depicted in black in all energy slices shown in figure 7.1 and is additionally depicted in the lower right panel as gray regions. Consistently, the masked regions correspond to the bright parts in the dark field STEM images, i.e. where a large fraction of the electrons is scattered by the gold. Furthermore, all spectra are normalized individually to the total amount of transmitted electrons, i.e. divided by the energy integral over the whole spectrum. This guarantees a quantitative comparison of the EELP signal of all spectra. Finally, the ZLP in every spectrum is approximated by a polynomial fit, which is then subtracted from the data.

Energy slices of the processed EELS data are shown for energy losses between 0.7 eV and 2.0 eV in steps of 0.1 eV in figure 7.1. For the first two shown energy slices of 0.7 eV and 0.8 eV, large parts of the unmasked regions appear to have a high EELP. This is partly caused by residuals of the ZLP, which were not completely removed by subtracting the fit model. However, from 0.9 eV to 2.0 eV the EELP can be attributed to LSPP excitations in the nanoporous film. Clear features of distinct "hotspots" appear in the energy region between 1.0 eV and 1.7 eV. Some resonant hotspots are marked by white dashed rectangles in the energy slice of their brightest appearance, corresponding to their resonance energy. At each hotspot, a spectrum integrated over an area of 2 by 3 pixels, which is exactly marked by the small black rectangles in the lower right panel of figure 7.1, is extracted. The corresponding EELP spectra are shown in figure 7.2. All spectra exhibit at least one resonance peak in the energy range between 1.0 eV and 1.5 eV. The energy positions of the strongest peaks in the spectra are in accordance with the slice energies, where the respective hotspot is highlighted by the white dashed rectangles in figure 7.1.

The hotspot at position 1 exhibits the strongest resonance (highest EELP) in the spectrum. The spectra are ordered by the maximum measured EELP signal. For the spectra in positions 2 to 4, the main resonance of the hotspot is accompanied by a second weaker resonance. As a general trend, one can observe that the stronger the second resonance, the weaker becomes the main resonance. In general, the widths of the occurring resonances in the spectra can be estimated roughly between 0.1 eV and 0.2 eV. However, these values have to be treated with care, because 0.1 eV is already at the resolution limit of the spectra due to the width of the
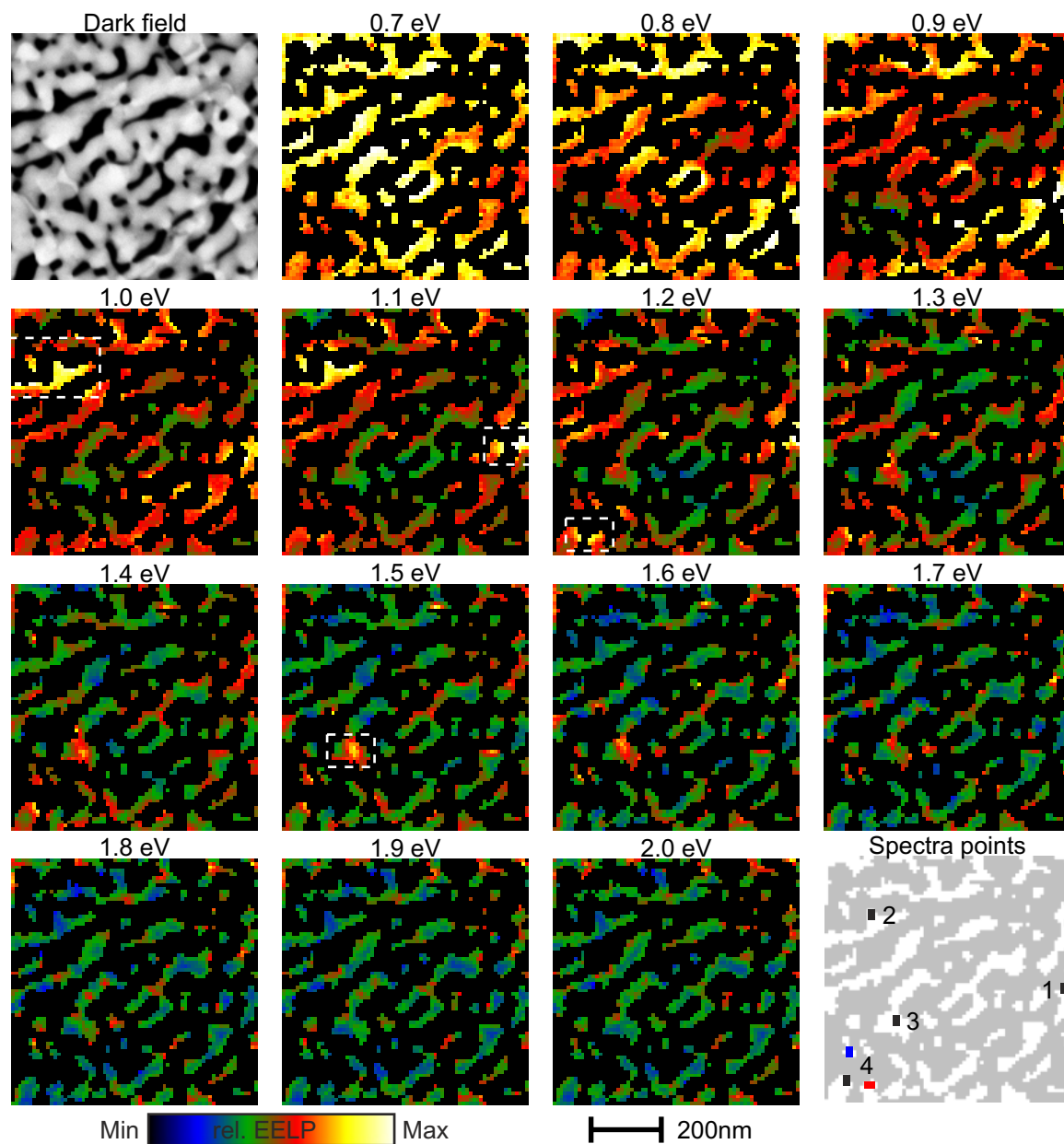
Figure 7.1: EELP maps for energy losses between 0.7 eV and 2.0 eV in steps of 0.1 eV of the EELS measurement on the nanoporous sample. The upper left panel shows a STEM image recorded by the dark field detector. The lower right panel depicts the mask applied to the EELS data as gray regions and clarifies positions by the rectangles, where the EEL spectra shown in figure 7.2 are extracted from.
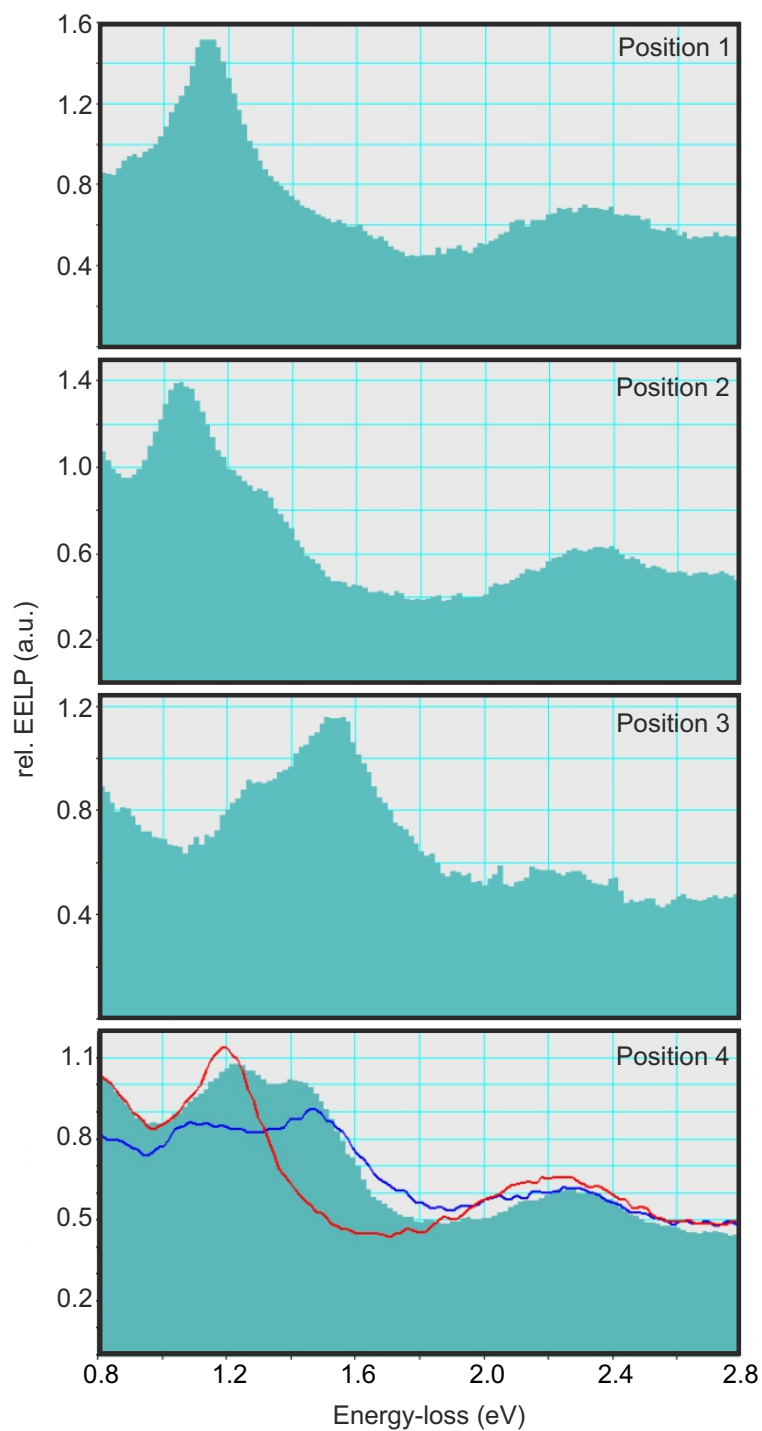
Figure 7.2: ELL spectra extracted from the EELS measurement on the nanoporous sample. The spectra are acquired from an integration over the 2 × 3 pixel rectangles marked in figure 7.1

ZLP. In reality the LSPP resonances are probably sharper than determined from the spectra. The measured spectral width from 0.1 eV to 0.2 eV correspond to LSPP lifetimes of 13 fs to 6.5 fs, which is reasonable for plasmonic resonances. At position 4, the strengths of the two occurring resonances at roughly 1.2 eV and 1.4 eV are comparable. However, the microscopic lateral field distribution of the hotspot in the energy slices significantly changes between the two resonance energies. To analyze this in further detail, two additional spectra are extracted at the positions marked with the blue and red rectangle in the lower right panel in figure 7.1. In the 1.2 eV EELP map, the hotspot appears bright in the region of the black and red rectangle. In contrast at 1.4 eV, a large EELP can be observed in the region of the black and blue rectangle. From the spectra plots for all three positions in the lowest panel in figure 7.2, it can be estimated, that the spectrum from the position of the black rectangle contains the features of both spectra extracted from the positions of the blue and red rectangles. This supports the hypothesis, that the two peaks belong to distinct LSPPs. From the arrangement of the two cases of paired rectangles once above each other and once beside each other, one may also conclude that the polarizations of the two LSPPs are almost orthogonal in the sample plane.

7.2 s-SNOM measurements

The sample, which is investigated by s-SNOM measurements in the following has been fabricated according to section 3.1.3 from a 12 K (50 %) leaf gold film, which resided on 68 % nitric acid for 20 h. Afterwards the nanoporous film is transferred to a glass substrate, which allows for reflection and transmission mode s-SNOM measurements. The applied fabrication parameters lead to slightly smaller pore sizes than in the previous section and the network remains 3D (c.f. figure 3.2). The thickness of the nanoporous gold film was measured to be approximately 125 nm by AFM measurements. Further details about the dependence of the pore properties on the fabrication parameters including SEM images can be found in section 3.1.3 and in [149]. The s-SNOM measurements are performed with the pseudoheterodyne detection technique in three different measurement modi, which are outlined in the sketches in figure 7.3. The depicted modi in (a) and (c) correspond to the standard reflection and transmission mode configurations discussed in section 4.2. The measurement mode depicted in (b) is identical to the reflection mode in (a), but with a horizontal polarization of the incident light. Also the detected light from the scattered radiation is filtered for horizontal polarization in this case. The in-plane angle of collection for the scattered radiation is clarified by a white arrow in the amplitude image for each measurement. All measurements include a scan area of 4 μm × 4 μm with a resolution of 20 nm/pixel. The scan is performed on different positions of the sample for the three measurements.

For the conventional near-field measurement in reflection mode presented in figure 7.3 (a), the OPO of the Alpha HP laser, tuned to a wavelength of 1400 nm, was used for illumination. The amplitude signal exhibits a relatively homogeneous ground level on the whole area of the nanoporous sample. Also the phase signal is almost constant along the fast (horizontal) axis
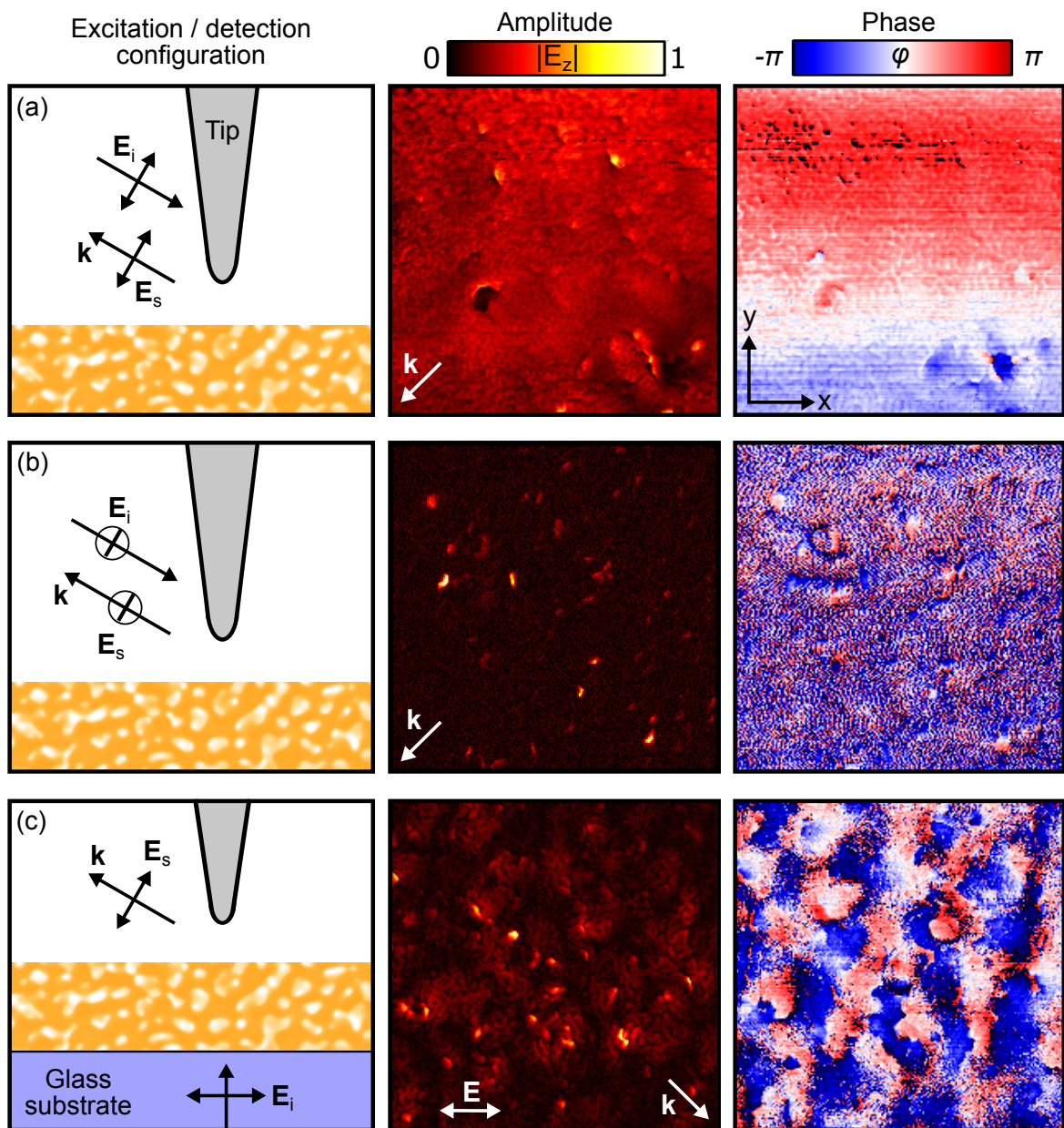
Figure 7.3: Interferometric s-SNOM measurements of the nanoporous gold film.
(a) In conventional reflection mode configuration with p-polarized incident light ($\lambda = 1400$ nm).
(b) In a modified reflection mode configuration with s-polarized incident light ($\lambda = 1040$ nm).
(c) In transmission mode configuration ($\lambda = 1040$ nm). Each subfigure contains a sketch depicting the excitation and detection configuration as well as an amplitude and phase image demodulated at the fourth harmonic of the tip oscillation frequency.

of the scan. The phase gradient during the measurement along the slow (vertical) axis can be attributed to a long term thermal drift in the reference arm of the interferometer during the scan. Apart from a few bright hotspots only slight variations from the homogeneous ground level occur due to the nanoporous nature of the film. The almost homogeneous ground level can be attributed to the near-field interaction between the tip and the sample, initiated by a direct excitation of the tip. According to figure 4.7 (a) in section 4.2.5 the vertical polarization component of the incident light excites a dipole moment in the tip, which induces an image dipole in the sample. The interaction between the two dipoles yields a significant near-field signal. However, in this simplified picture, the nanoporous nature of the film has to be neglected and treated as an effective homogeneous medium. For the near-field interaction, taking place on lateral lengths scales on the order of the tip apex dimensions, which is comparable or even smaller than the order of the average pore size, this is a highly questionable approximation. More precisely, the response of the sample may be attributed to the sum of microscopic nonresonant polarizations in the gold network excited by the near-field of the tip. On top of the almost homogeneous signal, bright hotspots appear at some positions on the sample. At these points the nanoporous film provides a local structure, featuring a LSPP resonance with a large out-of-plane electric near-field component. The LSPP resonance can either be excited by the local near-fields provided by the dipole moment of the tip, or directly by the incident radiation. In any case, for a strong LSPP resonance, this leads to a significantly higher near-field amplitude than the average ground level on the rest of the sample. In some cases also the near-field phase differs from the average phase in the surrounding region at these points. Additionally, the amplitude image exhibits some regions, which appear darker than the average ground level. This may be attributed to dirt i.e. residuals of materials other than gold remaining from the fabrication process, which hamper the near-field interaction between the tip and the film.

Figure 7.3 (b) shows a reflection measurement performed with horizontal incident polarization at a wavelength of 1040 nm provided by the pump laser of the Alpha HP. Due to the horizontal polarization, the tip can no longer be excited directly from the external radiation. In this case, most of the scan area exhibits no near-field signal at all, characterized by a vanishing near-field amplitude and a undefined (random) near-field phase. On these areas of vanishing near-field signal, neither the tip nor the sample respond to the horizontally polarized incident field. However, hotspots appear at some points on the sample. Only these hotspots exhibit a significant near-field amplitude and a well-defined near-field phase. At these hotspots, the nanoporous film eventually exhibits a structure featuring an LSPP resonance, which can be efficiently excited by the horizontal incident field at the given excitation frequency. The excited LSPP involves strong vertical near-field components, which can be probed by the tip, leading to a significant near-field signal. For many hotspots, the phase image reveals an in-plane dipole moment of the LSPP, characterized by two regions with an approximate relative phase shift of π.

Figure 7.3 (c) shows a transmission mode measurement with an incident polarization along the horizontal scan axis at a wavelength of 1040 nm provided by the pump laser of the Alpha HP. Comparable to (b), the amplitude image reveals bright hotspots at some positions of

the scan. Since the excitation is taking place from the substrate side of the sample, one can conclude that the excited LSPPs resulting in hotspots extend through the entire 125 nm thick film. In contrast to the measurement shown in figure 7.3 (b), the rest of the sample does not appear completely dark. At the sample surface exist relatively large regions of moderate near-field signal. The near-field signal in these regions may originate from LSPPs excited at the substrate side of the sample, which do not directly extend to the upper side of the film. However, the near-fields of these LSPPs may scatter through the film resulting in the extended region of moderate near-field signal. This hypothesis is further supported by the near-field phase signal. On the hotspots and the surrounding regions of moderate near-field signal the phase is well defined and often reveals a dipolar character, which is primarily oriented along the horizontal direction as the exciting polarization.

7.3 Comparison of the measurement techniques

The near-fields of nanoporous gold films have been investigated via EELS on an electron transparent substrate and via s-SNOM on a glass substrate in three different measurement modi. In all cases, hotspots could be observed. However, all performed measurements reveal partly complementary information about the samples. The EELS measurement provides the whole spectroscopic information about the sample in one measurement. In this case, the data normalization enables a direct quantitative comparison between different hotspots and excitation frequencies. However, the EELS measurement can only be performed on 2D networks and does not provide phase information. Additionally, the sample is only excited from the electron beam as a localized near-field source. The polarization dependent response of the sample to an optical excitation from the far-field can only be revealed by s-SNOM measurements. From the three different s-SNOM measurement modi, hotspots can be observed both on the illuminated side of the film and on the opposite side. Measuring in the standard reflection mode configuration (a) in principle allows for a normalization of the near-field signal of the hotspot to the average ground level of the near-field signal on the nanosponge, which enables a quantitative comparison of the signals on the hotspots between consecutive measurements, e.g. when performing a near-field spectroscopy. A more refined method for normalizing the hotspot signals to the signals on a solid gold film beside the nanoporous sample is presented in [149]. The other measurement modi (b) and (c) provide no ability for absolute signal normalization. Nevertheless, they reveal further important information. For instance, measurements (b) and (c) exclusively exhibit hotspots, which can be excited by far-field radiation without the need of the tip as a near-field source, i.e. they demonstrate the natural near-field response of the nanoporous sample to far-field radiation. Measurement (c) additionally reveals the transmission properties of the localized near-fields through the nanoporous film. In both cases, the in-plane polarization during the s-SNOM measurement can be chosen arbitrarily by rotating the sample.

Conclusions

In this work, two different techniques for the experimental investigation of optical near-fields, namely EELS and s-SNOM have been applied on plasmonic nanostructures. The investigated plasmonic sample systems range from extended array structures featuring thin-film SPPs over 1D plasmonic waveguide structures up to LSPPs occurring on random nanoporous gold structures.

The fabrication of plasmonic nanostructures presented in chapter 3 include the preparation of thin gold films and their patterning via FIB milling. Beyond the standard thermal evaporation method for the preparation of thin gold films, additional approaches for the chemical synthesis of single-crystalline and nanoporous gold films were covered in this context. Furthermore a new approach for the fabrication of freestanding structured thin gold films was presented.

In chapter 5, plasmonic hole arrays in both freestanding and SiN supported thin gold films have been investigated, using EELS and s-SNOM near-field measurements, respectively. Both near-field characterization techniques are complemented with far-field optical transmission spectroscopy. The samples feature an extraordinary optical transmission, which can be explained by a resonant excitation of SPPs via the hole arrays, which scatter to far-field radiation via the array on the other side of the film. The hole arrays feature different standing wave patterns of the resonantly excited SPPs, for different excitation energies according to the eigenmodes of the arrays. These standing wave patterns could be observed by the near-field measurements and consistently attributed to resonances in the optical far-field transmission spectra. Thereby, the near-field resonance was slightly redshifted with respect to the far-field resonance. The same behaviour is well-known for plasmonic nanoparticles and can be explained within the simple model of a driven damped harmonic oscillator [129].

In case of the freestanding films, the EELS and far-field measurements were compared to results from numerical simulations and theoretical calculations. In this context, plamonic hole arrays in freestanding films with different thicknesses from 22 nm to 74 nm were investigated. EELS was successfully performed only on the thinnest 22 nm film, due to insufficient electron transparency of the thicker samples. The eigenenergies of all observed array resonances from

EELS measurements, far-field spectra, numerical simulations and theoretical considerations are summarized in figure 5.7. From this analysis, one can identify a consistent blueshift of the eigenenergies for all array modes with increasing film thickness in all datasets. This behaviour can be explained by a shift of the thin film SPP dispersion relation with decreasing film thickness. Interestingly, the EELS analysis revealed an array mode, which could not be observed in the far-field. This mode can be classified as an optical dark mode, which can only be excited during the EELS measurement because the electron beam acts as a localized near-field source in this case.

SiN supported plasmonic hole arrays with different array periods between 850 nm and 1350 nm and film thicknesses between 20 nm and 50 nm were investigated by s-SNOM measurements in transmission mode configuration at a wavelength of 1600 nm. The near-fields were measured through the 30 nm thick SiN membrane. The resonant excitation of a standing wave pattern associated with the first eigenmode of the array could be observed in the near-field measurements for certain combinations of film thicknesses and array periods. For increasing thickness of the gold film the resonance shifts to longer array periods, which is equivalent to a blueshift of the resonance. The resonance positions of the first array eigenmode observed in the near-field are in accordance with the resonances occurring in the far-field optical transmission spectra.

In chapter 6, PSWs and far-field couplers for an efficient excitation of the waveguide mode were investigated by transmission mode s-SNOM measurements. In the fist part, a parametric study on PSWs of different widths between 50 nm and 170 nm in single- and poly-crystalline gold films was performed in order to study the effect of the material quality on the mode propagation. The waveguide mode was launched on one side of the PSW via a fixed focused beam excitation with $\lambda = 1520$ nm onto a far-field coupler. The measured near-field amplitude and phase along the PSW reveals the asymmetric nature of the guided mode during propagation. The effective index and the propagation length of the PSW mode was extracted from the near-field data via a 2D complex fit. For the PSWs both in single- and poly-crystalline films, the effective mode index decreases with increasing slot width, which can be attributed to the general correlation between confinement and propagation constant in plasmonic waveguides. Interestingly, the propagation length exhibits a maximum at certain PSW widths for both materials. This can be explained by a trade-off between higher Ohmic losses, accompanied with the higher mode confinement for the thin PSWs and emerging leakage radiation losses as the effective mode index falls below the refractive index of the glass substrate for the thicker PSWs. The higher quality of the single-crystalline film has a huge impact in the regime of high Ohmic losses for slot widths below 80 nm. Here, a maximum propagation length of 6 μm could be observed corresponding to an improvement up to a factor of two compared to the poly-crystalline films. However for slot widths above 100 nm, where leakage radiation is dominant, both materials support mode propagation over comparable distances of 3 μm to 4 μm.

In the second part of the chapter, the selective excitation of two PSWs by a plasmonic ring coupler upon illumination with circularly polarized light has been demonstrated via transmission mode s-SNOM measurements. The excitation could be mostly restricted to

one or the other output PSW by switching the helicity of the circularly polarized excitation beam. For an excitation with linearly polarized light, corresponding to a symmetric linear combination of left- and right-handed circularly polarized light, both PSWs are excited. A spectroscopic analysis reveals that the directional functionality of the coupler is preserved in a wavelength range between 1450 nm and 1650 nm.

In chapter 7, near-field measurements have been performed on nanoporous gold films via EELS on an electron transparent substrate and via s-SNOM on a glass substrate. In all cases, hotspots originating from LSPPs could be observed. EEL spectra were extracted at four hotspot positions. The spectra reveal LSPP resonances at energies between 1.0 eV and 1.5 eV, which form the hotspots. Some hotspots constitute at least two overlayed LSPP resonances. The spectral width of the individual LSPPs lies roughly between 0.1 eV and 0.2 eV. This corresponds to LSPP lifetimes of 13 fs to 6.5 fs, which is reasonable for plasmonic resonances [4]. However, these values have to be taken with care, because 0.1 eV is already at the resolution limit of the spectra due to the width of the ZLP.

Additionally, s-SNOM measurements have been performed on a different nanoporous gold film in three measurement modi, namely reflection mode with primarily vertical and horizontal incident polarization and transmission mode configuration. The best visibility of the hotspots is provided by measurements with horizontal incident polarization both in reflection and transmission mode. The occurrence of hotspots in the transmission mode measurement implies that some LSPPs range through the entire 125 nm thick film.

Outlook

The s-SNOM measurements on the plasmonic hole arrays could be extended to observe the $(1, 1)$ or $(2, 0)$ mode by either reducing the excitation wavelength or investigate samples with larger array periods. One could also attempt to excite the dark "$(1.5, 0)$" mode, which was already observed in the EELS analysis using s-SNOM. However, in s-SNOM measurements, this can only be achieved in reflection mode, for which the tip is acting as a near-field source in order to excite the dark mode. The $(1.5, 0)$ mode could also be invesitgated in far-field experiments by inclining the sample with respect to the axis of the incident beam, which imposes an additional phase shift of the arriving phase fronts in the sample plane.

The parametric study of the PSWs in single- and poly-crystalline gold revealed a maximum of the mode propagation length for a certain slot width, due to the trade off between Ohmic and leakage radiation losses. The emergence of leakage radiation can potentially be shifted to larger slot width or be completely suppressed by adding a thin dielectric layer with a refractive index similar to the substrate on top of the PSWs. A sufficiently thick layer on top can provide a symmetric refractive index environment around the PSW. In this case, the effective mode index of the PSW is always larger than the surrounding refractive index, which fully prevents leakage radiation. This enables to study the effect of the material quality and slot width exclusively on the Ohmic losses. However for the s-SNOM investigation, the top dielectric layer must be very thin in order to be able to probe the evanescent fields of the PSW via the tip on the top surface. A 30 nm thick cover layer of polymethyl methacrylate (PMMA)

deposited by spin coating, which has the same refractive index as the glass substrate, could be a good starting point. Indeed, the s-SNOM measurements on the SiN covered plamonic hole arrays have shown that evanescent fields can be measured through a 30 nm dielectric layer.

The selective excitation of two distinct PSWs by a plasmonic ring coupler based on the helicity of the incident light was demonstrated in section 6.2 via s-SNOM measurements. This analysis revealed some drawbacks of the investigated sample, which was originally designed for a far-field investigation. In the end of this section, two optimized samples for near-field investigations on chiral coupling were proposed (c.f. figure 6.13). The anticipated improvements include shorter measurement times and a quantitative extraction of the coupling directionality.

The nanoporous films investigated in chapter 7, with their structural diversity resulting from the application of different fabrication parameters constitute a huge playground for further near-field measurements. Combining EELS and s-SNOM in different configurations on the very same sample area could provide extensive information about the nature of the occurring hotspots regarding their spectral behaviour, response to different incident polarizations and the near-field transmission and plasmon scattering through the film. Furthermore, by comparing the measurement results, one might also gain a deeper understanding of how to interpret the data from the different techniques and configurations individually in future investigations.

In principle, the NeaSNOM system in combination with the pulsed external laser sources provides the opportunity to investigate nonlinear optical effects like second harmonic generation (SHG) in plasmonic nanostructures in the near-field. Reasonable candidates as plasmonic structures for such investigations could be V-shaped nanoantennas, which show SHG in far-field experiments [150] or plasmonic hole arrays, on which second harmonic near-field experiments have already been conducted using a-SNOM in transmission mode [135]. In our case, upconverted light via SHG from the NIR radiation of the employed Alpha HP OPO laser could be detected by the VIS detector in the NeaSNOM. Note that only non-interferometric SHG near-field signals can be detected, since there is no upconversion in the reference arm. Additionally, the fundamental excitation could be measured as usual with the NIR detector for comparison. However, first application attempts of this method to V-shaped nanoantennas via transmission mode s-SNOM remained unsuccessful so far. Although a strong excitation of the fundamental antenna mode could be observed via transmission mode s-SNOM measurements with the NIR detector [151], only noise could be measured via the VIS detector down to the first demodulation order. In this context, the temporal width of output pulses T_p of the OPO have been temporally compressed from initially $T_p \approx 400\,\mathrm{fs}$ to $T_p \approx 100\,\mathrm{fs}$ in the best case [101]. Further pulse compression to the sub-100 fs regime might strongly enhance the SHG on the sample and eventually enable a significant signal-to-noise ratio in the near-field detection of the SHG signals. Furthermore one could try SHG s-SNOM experiments on different samples e.g. the SiN supported plasmonic hole arrays investigated in section 5.3.3 or on the nanoporous gold films measured in section 7.2.

Bibliography

[1]   D. K. Gramotnev and S. I. Bozhevolnyi, *Plasmonics beyond the diffraction limit*,
      Nat. Photonics **4** (2010) 83 (cit. on pp. 1, 19).

[2]   E. Abbe,
      Beiträge zur Theorie des Mikroskops und der mikroskopischen Wahrnehmung,
      Archiv für mikroskopische Anatomie **9** (1873) 413 (cit. on pp. 1, 7).

[3]   L. Rayleigh,
      XXXI. Investigations in optics, with special reference to the spectroscope,
      The London, Edinburgh, and Dublin Philosophical Magazine and Journal of Science
      8 (1879) 261 (cit. on pp. 1, 7).

[4]   S. A. Maier, *Plasmonics: fundamentals and applications*,
      Springer Science & Business Media, 2007 (cit. on pp. 1, 2, 10, 13, 48, 107).

[5]   L. Novotny and B. Hecht, *Principles of nano-optics*,
      Cambridge university press, 2012 (cit. on pp. 1, 3–7, 10, 11, 18, 19, 31, 32, 40).

[6]   J. Dorfmuller et al.,
      Plasmonic nanowire antennas: experiment, simulation, and theory,
      Nano Lett. **10** (2010) 3596 (cit. on pp. 1, 19, 73).

[7]   V. A. Zenin et al.,
      Near-field characterization of bound plasmonic modes in metal strip waveguides,
      Opt. Express **24** (2016) 4582 (cit. on pp. 1, 2, 19, 73).

[8]   A. Akimov et al.,
      Generation of single optical plasmons in metallic nanowires coupled to quantum dots,
      Nature **450** (2007) 402 (cit. on pp. 1, 19).

[9]   D. F. P. Pile and D. K. Gramotnev,
      Channel plasmon–polariton in a triangular groove on a metal surface,
      Opt. Lett. **29** (2004) 1069 (cit. on pp. 1, 19).

[10] A. Melikyan et al., *High-speed plasmonic phase modulators*,
      Nat. Photonics **8** (2014) 229 (cit. on pp. 1, 19, 73).

[11] K. A. Willets and R. P. Van Duyne,
      Localized surface plasmon resonance spectroscopy and sensing,
      Annu. Rev. Phys. Chem. **58** (2007) 267 (cit. on pp. 1, 19).

[12] K. M. Mayer and J. H. Hafner, *Localized surface plasmon resonance sensors*,
      Chem. Rev. **111** (2011) 3828 (cit. on pp. 1, 19).

[13] W.-C. Shih et al., *Simultaneous chemical and refractive index sensing in the
      1–2.5 μm near-infrared wavelength range on nanoporous gold disks*,
      Nano Lett. **16** (2016) 4641 (cit. on pp. 1, 21, 97).

[14] J. Qi et al., *Surface-enhanced Raman spectroscopy with monolithic nanoporous gold
      disk substrates*, Nanoscale **5** (2013) 4105 (cit. on pp. 1, 97).

[15] K. Liu et al., *Porous Au–Ag nanospheres with high-density and highly accessible
      hotspots for SERS analysis*, Nano Lett. **16** (2016) 3675 (cit. on pp. 1, 97).

[16] D. E. Chang et al., *Strong coupling of single emitters to surface plasmons*,
      Phys. Rev. B **76** (2007) 035420 (cit. on pp. 1, 19, 74).

[17] M. Peter et al., *Fluorescence enhancement by a dark plasmon mode*,
      Appl. Phys. B **124** (2018) 83 (cit. on p. 1).

[18] W. Cai and V. M. Shalaev, *Optical metamaterials*, vol. 10, 6011, Springer, 2010
      (cit. on pp. 1, 9, 19).

[19] N. Yu et al., *Light propagation with phase discontinuities: generalized laws of
      reflection and refraction*, Science **334** (2011) 333 (cit. on pp. 1, 19, 29).

[20] A. Andryieuski et al.,
      Direct Characterization of Plasmonic Slot Waveguides and Nanocouplers,
      Nano Lett. **14** (2014) 3925 (cit. on pp. 2, 19, 73, 74, 76, 83).

[21] M. Prämassing et al., *Interferometric near-field characterization of plasmonic slot
      waveguides in single-and poly-crystalline gold films*, Opt. Express **28** (2020) 12998
      (cit. on pp. 2, 22, 23, 73, 74, 84, 86, 87).

[22] H. Wei et al., *Plasmon waveguiding in nanowires*, Chem. Rev. **118** (2018) 2882
      (cit. on pp. 2, 74).

[23] J.-S. Huang et al.,
      Atomically flat single-crystalline gold nanostructures for plasmonic nanocircuitry,
      Nat. Commun. **1** (2010) 1 (cit. on pp. 2, 21, 75).

[24] P. Kusar et al., *Measurement and reduction of damping in plasmonic nanowires*,
      Nano Lett. **12** (2012) 661 (cit. on pp. 2, 74, 75).

[25] H. Ditlbacher et al., *Silver nanowires as surface plasmon resonators*,
      Phys. Rev. Lett. **95** (2005) 257403 (cit. on pp. 2, 75).

[26] G. Binnig, C. F. Quate and C. Gerber, *Atomic force microscope*,
      Phys. Rev. Lett. **56** (1986) 930 (cit. on pp. 2, 31).

[27] G. Binnig et al., *Atomic resolution with atomic force microscope*,
      EPL (Europhysics Letters) **3** (1987) 1281 (cit. on p. 2).

[28] M. Varela et al., *Materials characterization in the aberration-corrected scanning transmission electron microscope*, Annu. Rev. Mater. Res. **35** (2005) 539 (cit. on p. 2).

[29] B. Knoll and F. Keilmann, *Near-field probing of vibrational absorption for chemical microscopy*, Nature **399** (1999) 134 (cit. on pp. 2, 31, 49).

[30] D. W. Pohl, W. Denk and M. Lanz, *Optical stethoscopy: Image recording with resolution λ/20*, Appl. Phys. Lett. **44** (1984) 651 (cit. on pp. 2, 31).

[31] M. Bosman et al., *Mapping surface plasmons at the nanometre scale with an electron beam*, Nanotechnology **18** (2007) 165505 (cit. on p. 2).

[32] F. von Cube et al., *Spatio-spectral characterization of photonic meta-atoms with electron energy-loss spectroscopy*, Opt. Mater. Express **1** (2011) 1009 (cit. on pp. 2, 12, 15, 19, 34).

[33] A. Polman, M. Kociak and F. J. G. de Abajo, *Electron-beam spectroscopy for nanophotonics*, Nat. Mater. (2019) 1 (cit. on pp. 2, 32).

[34] I. C. Bicket et al., *Correlative electron energy loss spectroscopy and cathodoluminescence spectroscopy on three-dimensional plasmonic split ring resonators*, Microscopy **67** (2018) i40 (cit. on p. 2).

[35] T. Neuman et al., *Mapping the near fields of plasmonic nanoantennas by scattering-type scanning near-field optical microscopy*, Laser & Photonics Reviews **9** (2015) 637 (cit. on p. 2).

[36] R. Esteban et al., *Direct near-field optical imaging of higher order plasmonic resonances*, Nano Lett. **8** (2008) 3155 (cit. on p. 2).

[37] M. Kuttge et al., *Loss mechanisms of surface plasmon polaritons on gold probed by cathodoluminescence imaging spectroscopy.*, Appl. Phys. Lett. **93** (2008) 113110 (cit. on pp. 2, 75).

[38] W. Demtröder, *Experimentalphysik 2*, vol. 2, Springer, 2005 (cit. on p. 4).

[39] J. D. Jackson, *Classical electrodynamics*, John Wiley & Sons, 2007 (cit. on pp. 4, 6).

[40] M. G. Silveirinha, *Nonlocal homogenization model for a periodic array of ϵ-negative rods*, Phys. Rev. E **73** (2006) 046612 (cit. on p. 5).

[41] J. W. Goodman, *Introduction to Fourier optics*, Roberts and Company Publishers, 2005 (cit. on p. 7).

[42] J. B. Pendry, *Negative refraction makes a perfect lens*,
Phys. Rev. Lett. **85** (2000) 3966 (cit. on p. 9).

[43] N. Fang et al., *Sub–diffraction-limited optical imaging with a silver superlens*,
Science **308** (2005) 534 (cit. on p. 9).

[44] T. Taubner et al., *Near-field microscopy through a SiC superlens*,
Science **313** (2006) 1595 (cit. on pp. 9, 10).

[45] Z. Liu et al., *Far-field optical hyperlens magnifying sub-diffraction-limited objects*,
Science **315** (2007) 1686 (cit. on p. 9).

[46] H. Raether, *Surface plasmons*, Springer Tracts in Modern Physics **111** (1988) 1
(cit. on p. 10).

[47] R. Hillenbrand, T. Taubner and F. Keilmann,
Phonon-enhanced light–matter interaction at the nanometre scale,
Nature **418** (2002) 159 (cit. on pp. 10, 31, 49).

[48] J. D. Caldwell et al.,
Low-loss, infrared and terahertz nanophotonics using surface phonon polaritons,
Nanophotonics **4** (2015) 44 (cit. on p. 10).

[49] V. W. Brar et al., *Hybrid surface-phonon-plasmon polariton modes in
graphene/monolayer h-BN heterostructures*, Nano Lett. **14** (2014) 3876
(cit. on p. 10).

[50] S. Dai et al.,
Graphene on hexagonal boron nitride as a tunable hyperbolic metamaterial,
Nature Nanotech **10** (2015) 682 (cit. on p. 10).

[51] J. Chen et al., *Optical nano-imaging of gate-tunable graphene plasmons*,
Nature **487** (2012) 77 (cit. on p. 10).

[52] Z. Fei et al., *Gate-tuning of graphene plasmons revealed by infrared nano-imaging*,
Nature **487** (2012) 82 (cit. on p. 10).

[53] M. D'yakonov, *New type of electromagnetic wave propagating at an interface*,
Sov. Phys. JETP **67** (1988) 714 (cit. on p. 10).

[54] N. Talebi et al., *Wedge Dyakonov waves and Dyakonov plasmons in topological
insulator Bi_2Se_3 probed by electron beams*, ACS Nano **10** (2016) 6988 (cit. on p. 10).

[55] P. Drude, *Zur elektronentheorie der metalle*, Annalen der physik **306** (1900) 566
(cit. on p. 10).

[56] H. Lorentz, "The motion of electrons in metallic bodies I", *KNAW, proceedings*,
vol. 7, 1905 438 (cit. on p. 11).

[57] F. Cheng et al., *Structural color printing based on plasmonic metasurfaces of perfect
light absorption*, Scientific Reports **5** (2015) 11045 (cit. on pp. 11, 53).

[58] C. F. Bohren and D. R. Huffman,
Absorption and scattering of light by small particles, John Wiley & Sons, 2008
(cit. on p. 11).

[59] P. B. Johnson and R.-W. Christy, *Optical constants of the noble metals*,
Phys. Rev. B **6** (1972) 4370 (cit. on pp. 12, 15, 16, 87).

[60] F. Yang, J. Sambles and G. Bradberry,
Long-range surface modes supported by thin films, Phys. Rev. B **44** (1991) 5855
(cit. on pp. 15, 16).

[61] F. Bleckmann et al.,
Spectral imaging of topological edge states in plasmonic waveguide arrays,
Phys. Rev. B **96** (2017) 045417 (cit. on p. 18).

[62] Z. Cherpakova et al.,
Transverse Anderson localization of surface plasmon polaritons,
Opt. Lett. **42** (2017) 2165 (cit. on p. 18).

[63] J.-C. Weeber et al., *Plasmon polaritons of metallic nanowires for controlling
submicron propagation of light*, Phys. Rev. B **60** (1999) 9061 (cit. on p. 19).

[64] J. R. Krenn et al., *Non–diffraction-limited light transport by gold nanowires*,
EPL (Europhysics Letters) **60** (2002) 663 (cit. on p. 19).

[65] P. Berini, *Plasmon-polariton waves guided by thin lossy metal films of finite width:
Bound modes of symmetric structures*, Phys. Rev. B **61** (2000) 10484 (cit. on p. 19).

[66] M. L. Brongersma, J. W. Hartman and H. A. Atwater, *Electromagnetic energy
transfer and switching in nanoparticle chain arrays below the diffraction limit*,
Phys. Rev. B **62** (2000) R16356 (cit. on p. 19).

[67] S. A. Maier et al., *Local detection of electromagnetic energy transport below the
diffraction limit in metal nanoparticle plasmon waveguides*, Nat. Mater. **2** (2003) 229
(cit. on p. 19).

[68] I. V. Novikov and A. A. Maradudin, *Channel polaritons*,
Phys. Rev. B **66** (2002) 035403 (cit. on p. 19).

[69] G. Veronis and S. Fan,
Guided subwavelength plasmonic mode supported by a slot in a thin metal film,
Opt. Lett. **30** (2005) 3359 (cit. on pp. 19, 73).

[70] G. Veronis and S. Fan, *Modes of Subwavelength Plasmonic Slot Waveguides*,
J. Light. Technol. **25** (2007) 2511 (cit. on pp. 19, 73, 85).

[71] M. Thomaschewski et al.,
On-Chip Detection of Optical Spin–Orbit Interactions in Plasmonic Nanocircuits,
Nano Lett. **19** (2019) 1166 (cit. on pp. 19, 88).

[72]   R. F. Oulton et al., *Plasmon lasers at deep subwavelength scale*,
       Nature **461** (2009) 629 (cit. on p. 19).

[73]   D. K. Gramotnev, K. C. Vernon and D. F. P. Pile,
       Directional coupler using gap plasmon waveguides, Appl. Phys. B **93** (2008) 99
       (cit. on pp. 19, 73).

[74]   Y. C. Jun et al., *Nonresonant enhancement of spontaneous emission in
       metal-dielectric-metal plasmon waveguide structures*, Phys. Rev. B **78** (2008) 153111
       (cit. on p. 19).

[75]   C. Huck et al., *Surface-enhanced infrared spectroscopy using nanometer-sized gaps*,
       ACS Nano **8** (2014) 4908 (cit. on p. 19).

[76]   M. Hentschel et al., *Chiral plasmonics*, Science advances **3** (2017) e1602735
       (cit. on p. 19).

[77]   M. Prämassing et al., *Freestanding metasurfaces for optical frequencies*,
       Opt. Lett. **44** (2019) 2105 (cit. on pp. 19, 21, 27–29).

[78]   Q. Ai et al.,
       Ultranarrow second-harmonic resonances in hybrid plasmon-fiber cavities,
       Nano Lett. **18** (2018) 5576 (cit. on p. 21).

[79]   C. Rewitz et al., *Coherent control of plasmon propagation in a nanocircuit*,
       Phys. Rev. Applied **1** (2014) 014007 (cit. on pp. 21, 73, 88).

[80]   M. I. Stockman et al., *Roadmap on plasmonics*, Journal of Optics **20** (2018) 043001
       (cit. on p. 21).

[81]   C. Schörner, S. Adhikari and M. Lippitz,
       A single-crystalline silver plasmonic circuit for visible quantum emitters,
       Nano Lett. (2019) (cit. on p. 21).

[82]   H.-J. Schill,
       Herstellung einkristalliner Goldplatelets für plasmonische Anwendungen,
       Bachelor thesis: Universität Bonn, 2018 (cit. on p. 22).

[83]   E. Krauss et al.,
       Controlled growth of high-aspect-ratio single-crystalline gold platelets,
       Crystal Growth & Design **18** (2018) 1297 (cit. on p. 22).

[84]   T. Härtling et al., *Controlled photochemical particle growth in two-dimensional
       ordered metal nanoparticle arrays*, Nanotechnology **21** (2010) 145309 (cit. on p. 22).

[85]   Y. Ding, Y.-J. Kim and J. Erlebacher,
       Nanoporous gold leaf:"Ancient technology"/advanced material,
       Advanced materials **16** (2004) 1897 (cit. on pp. 23, 97).

[86]   W. Sigle et al., *EFTEM study of surface plasmon resonances in silver nanoholes*,
       Ultramicroscopy **110** (2010) 1094 (cit. on pp. 27, 53).

[87] N. Talebi et al., *On the symmetry and topology of plasmonic eigenmodes in heptamer and hexamer nanocavities*, Appl. Phys. A **116** (2014) 947 (cit. on pp. 27, 53).

[88] A. Cui et al., *Directly patterned substrate-free plasmonic "nanograter" structures with unusual Fano resonances*, Light: Science & Applications **4** (2015) e308 (cit. on p. 27).

[89] A. Faßbender et al., *Direct phase mapping of broadband Laguerre-Gaussian metasurfaces*, APL Photonics **3** (2018) 110803 (cit. on p. 29).

[90] R. Decca, H. Drew and K. Empson, *Investigation of the electric-field distribution at the subwavelength aperture of a near-field scanning optical microscope*, Appl. Phys. Lett. **70** (1997) 1932 (cit. on p. 31).

[91] H. A. Bethe, *Theory of diffraction by small holes*, Phys. Rev. **66** (1944) 163 (cit. on p. 31).

[92] F. J. Garcıa de Abajo, *Optical excitations in electron microscopy*, Rev. Mod. Phys. **82** (1 2010) 209 (cit. on pp. 32, 62).

[93] F. J. García de Abajo and M. Kociak, *Probing the Photonic Local Density of States with Electron Energy Loss Spectroscopy*, Phys. Rev. Lett. **100** (2008) 106804 (cit. on p. 32).

[94] U. Hohenester, H. Ditlbacher and J. R. Krenn, *Electron-Energy-Loss Spectra of Plasmonic Nanoparticles*, Phys. Rev. Lett. **103** (2009) 106801 (cit. on p. 32).

[95] R. H. Ritchie, *Plasma Losses by Fast Electrons in Thin Films*, Phys. Rev. **106** (5 1957) 874 (cit. on pp. 32, 62).

[96] F. von Cube, *Near field characterization of plasmonic nanostructures with electron energy loss spectroscopy*, PhD thesis: Universität Bonn, 2014 (cit. on p. 34).

[97] T. Weber, *Near-field characterization of superfocusing plasmonic nanostructures by electron energy loss spectroscopy*, PhD thesis: Universität Bonn, 2017 (cit. on p. 34).

[98] C. C. Ahn, *Transmission electron energy loss spectrometry in materials science and the EELS atlas*, John Wiley & Sons, 2006 (cit. on p. 35).

[99] R. Hegenbarth et al., *Two-color femtosecond optical parametric oscillator with 1.7 W output pumped by a 7.4 W Yb:KGW laser*, JOSA B **28** (2011) 1344 (cit. on p. 39).

[100] L. Rieland, *Untersuchung von Mehrphotonenabsorption in Halbleiter-Photodioden*, Bachelor thesis: Universität Bonn, 2018 (cit. on p. 40).

[101] F. Affeld, *Erzeugung von 100 fs Laserpulsen durch Selbstphasenmodulation in einer optischen Faser und Dispersionskompensation mit einem Prismenkompressor*, Bachelor thesis: Universität Bonn, 2020 (cit. on pp. 40, 108).

[102] N. Ocelic, *Quantitative Near-field Phonon-polariton Spectroscopy*, PhD thesis: Technische Universität München, 2007 (cit. on p. 42).

[103] N. Ocelic, A. Huber and R. Hillenbrand, *Pseudoheterodyne detection for background-free near-field spectroscopy*, Appl. Phys. Lett. **89** (2006) 101124 (cit. on pp. 42, 46).

[104] R. Hillenbrand and F. Keilmann, *Material-specific mapping of metal/semiconductor/dielectric nanosystems at 10 nm resolution by backscattering near-field optical microscopy*, Appl. Phys. Lett. **80** (2002) 25 (cit. on p. 49).

[105] T. Taubner, R. Hillenbrand and F. Keilmann, *Nanoscale polymer recognition by spectral signature in scattering infrared near-field microscopy*, Appl. Phys. Lett. **85** (2004) 5064 (cit. on p. 49).

[106] A. Cvitkovic, N. Ocelic and R. Hillenbrand, *Analytical model for quantitative prediction of material contrasts in scattering-type near-field optical microscopy*, Opt. Express **15** (2007) 8550 (cit. on p. 49).

[107] B. Hauer, A. P. Engelhardt and T. Taubner, *Quasi-analytical model for scattering infrared near-field microscopy on layered systems*, Opt. Express **20** (2012) 13173 (cit. on p. 49).

[108] S. Amarie, T. Ganz and F. Keilmann, *Mid-infrared near-field spectroscopy*, Opt. Express **17** (2009) 21794 (cit. on p. 51).

[109] T. W. Ebbesen et al., *Extraordinary optical transmission through sub-wavelength hole arrays*, Nature **391** (1998) 667 (cit. on p. 53).

[110] E. Popov et al., *Theory of light transmission through subwavelength periodic hole arrays*, Phys. Rev. B **62** (2000) 16100 (cit. on p. 53).

[111] L. Martín-Moreno et al., *Theory of Extraordinary Optical Transmission through Subwavelength Hole Arrays*, Phys. Rev. Lett. **86** (2001) 1114 (cit. on p. 53).

[112] C. Genet and T. W. Ebbesen, *Light in tiny holes*, Nature **445** (2007) 39 (cit. on pp. 53, 54).

[113] F. J. García de Abajo, *Colloquium: Light scattering by particle and hole arrays*, Reviews of Modern Physics **79** (2007) 1267 (cit. on p. 53).

[114] H. Liu and P. Lalanne, *Microscopic theory of the extraordinary optical transmission*, Nature **452** (2008) 728 (cit. on p. 53).

[115] J. Braun et al., *How Holes Can Obscure the View: Suppressed Transmission through an Ultrathin Metal Film by a Subwavelength Hole Array*, Phys. Rev. Lett. **103** (2009) 203901 (cit. on pp. 53, 54).

[116] J. Grant, I. J. H. McCrindle and D. R. S. Cumming,
Multi-spectral materials: hybridisation of optical plasmonic filters, a mid infrared metamaterial absorber and a terahertz metamaterial absorber,
Opt. Express **24** (2016) 3451 (cit. on p. 53).

[117] I. J. H. McCrindle et al., *Hybridization of optical plasmonics with terahertz metamaterials to create multi-spectral filters*, Opt. Express **21** (2013) 19142 (cit. on p. 53).

[118] R. Gordon et al.,
A New Generation of Sensors Based on Extraordinary Optical Transmission,
Accounts of Chemical Research **41** (2008) 1049 (cit. on p. 53).

[119] F. Eftekhari et al., *Nanoholes As Nanochannels: Flow-through Plasmonic Sensing*,
Analytical Chemistry **81** (2009) 4308 (cit. on p. 53).

[120] J.-Y. Li et al., *Scanning near-field optical microscopy study of metallic square hole array nanostructures*, Journal of Applied Physics **104** (2008) 114303 (cit. on p. 53).

[121] J.-Y. Chu et al., *Near-field observation of plasmon excitation and propagation on ordered elliptical hole arrays*, Appl. Phys. A **89** (2007) 387 (cit. on p. 53).

[122] G. Ctistis et al., *Optical Transmission through Hexagonal Arrays of Subwavelength Holes in Thin Metal Films*, Nano Lett. **7** (2007) 2926 (cit. on p. 53).

[123] L. Jiang-Yan, G. Lin and L. Zhi-Yuan, *Near-field optical observations of surface plasmon wave interference at subwavelength hole arrays perforated in Au film*,
Chinese Physics B **22** (2013) 117302 (cit. on p. 53).

[124] M. Mrejen et al., *Near-field characterization of extraordinary optical transmission in sub-wavelength aperture arrays*, Opt. Express **15** (2007) 9129 (cit. on p. 53).

[125] C. Sönnichsen et al., *Launching surface plasmons into nanoholes in metal films*,
Appl. Phys. Lett. **76** (2000) 140 (cit. on p. 53).

[126] K. Busch, M. König and J. Niegemann,
Discontinuous Galerkin methods in nanophotonics,
Laser & Photonics Reviews **5** (2011) 773 (cit. on p. 57).

[127] C. Matyssek et al., *Computing electron energy loss spectra with the Discontinuous Galerkin Time-Domain method*,
Photonics and Nanostructures - Fundamentals and Applications **9** (2011) 367
(cit. on p. 57).

[128] B. Schröder et al.,
Real-space imaging of nanotip plasmons using electron energy loss spectroscopy,
Phys. Rev. B **92** (2015) 085411 (cit. on p. 59).

[129] J. Zuloaga and P. Nordlander, *On the energy shift between near-field and far-field peak intensities in localized plasmon systems*, Nano letters **11** (2011) 1280
(cit. on pp. 61, 72, 105).

[130] W. C. Chew and W. H. Weedon, *A 3D perfectly matched medium from modified maxwell's equations with stretched coordinates*,
Microwave and Optical Technology Letters **7** (1994) 599 (cit. on p. 62).

[131] M. König et al., *Stretched-coordinate PMLs for Maxwell's equations in the discontinuous Galerkin time-domain method*, Opt. Express **19** (2011) 4618
(cit. on p. 62).

[132] F. von Cube et al.,
Angular-resolved electron energy loss spectroscopy on a split-ring resonator,
Phys. Rev. B **89** (2014) 115434 (cit. on p. 65).

[133] T. Weber et al., *Near-field study on the transition from localized to propagating plasmons on 2D nano-triangles*, Opt. Express **25** (2017) 16947 (cit. on p. 65).

[134] S. Hohng et al.,
Light emission from the shadows: Surface plasmon nano-optics at near and far fields,
Appl. Phys. Lett. **81** (2002) 3239 (cit. on p. 69).

[135] J. Beermann and S. Bozhevolnyi,
Second-harmonic near-field optical microscopy of periodic nanoholes in metal films,
Laser Physics Letters **1** (2004) 592 (cit. on pp. 69, 108).

[136] K. C. Y. Huang et al., *Electrically driven subwavelength optical nanocircuits*,
Nat. Photonics **8** (2014) 244 (cit. on p. 73).

[137] M. Spasenović et al.,
Measurements of modal symmetry in subwavelength plasmonic slot waveguides,
Appl. Phys. Lett. **95** (2009) 203109 (cit. on p. 73).

[138] V. A. Zenin et al., *Boosting local field enhancement by on-chip nanofocusing and impedance-matched plasmonic antennas*, Nano Lett. **15** (2015) 8148 (cit. on p. 73).

[139] Y. Chen et al., *Efficient interfacing photonic and long-range dielectric-loaded plasmonic waveguides*, Opt. Express **23** (2015) 9100 (cit. on pp. 73, 74).

[140] M. Liebtrau,
Fabrication and Near-field Characterization of Plasmonic Slot Waveguides,
Master thesis: Universität Bonn, 2018 (cit. on pp. 74, 79).

[141] J. H. Park et al., *Single-crystalline silver films for plasmonics*,
Advanced Materials **24** (2012) 3988 (cit. on p. 75).

[142] C.-Y. Wang et al.,
Giant colloidal silver crystals for low-loss linear and nonlinear plasmonics,
Nat. Commun. **6** (2015) 7734 (cit. on p. 75).

[143] R. Synowicki, *Spectroscopic ellipsometry characterization of indium tin oxide film microstructure and optical constants*, Thin Solid Films **313** (1998) 394
(cit. on p. 85).

[144] Y. Lefier et al., *Directing nanoscale optical flows by coupling photon spin to plasmon extrinsic angular momentum*, Nano Lett. **18** (2018) 38 (cit. on p. 88).

[145] J. Erlebacher et al., *Evolution of nanoporosity in dealloying*, Nature **410** (2001) 450 (cit. on p. 97).

[146] M. Bosman et al., *Light splitting in nanoporous gold and silver*, ACS Nano **6** (2012) 319 (cit. on p. 97).

[147] J. Zhong et al., *Strong spatial and spectral localization of surface plasmons in individual randomly disordered gold nanosponges*, Nano Lett. **18** (2018) 4957 (cit. on p. 97).

[148] H.-A. Chen et al., *Plasmonic properties of a nanoporous gold film investigated by far-field and near-field optical techniques*, Journal of Applied Physics **110** (2011) 054302 (cit. on p. 97).

[149] N. Grund, *Near-field characterization of nanoporous gold films*, Master thesis: Universität Bonn, 2020 (cit. on pp. 101, 104).

[150] H. Linnenbank and S. Linden, *Second harmonic generation spectroscopy on second harmonic resonant plasmonic metamaterials*, Optica **2** (2015) 698 (cit. on p. 108).

[151] L. Naumann, *Scanning Near-Field Optical Microscopy of Plasmonic Metasurfaces*, Master thesis: Universität Bonn, 2019 (cit. on p. 108).

Appendix

Frequency component u_n at the s-SNOM detector

The frequency components u_n can be found by inserting equations (4.3) and (4.4) together with the complex coefficient $\sigma_{\text{ref}} = s_{\text{ref}} e^{i\phi_{\text{ref}}} = E_{\text{ref}}/E_i$ relating the reference field to the initial field into equation (4.5):

$$u(t) \propto \left| \sum_{n=0}^{\infty} \sigma_n \cos(n\Omega t) + \sum_{n=0}^{\infty} \sigma_{\text{b,n}} \cos(n\Omega t) + \sigma_{\text{ref}} \right|^2 \tag{1}$$

$$= \left[\sum_{n=0}^{\infty} \sigma_n \cos(n\Omega t) + \sum_{n=0}^{\infty} \sigma_{\text{b,n}} \cos(n\Omega t) + \sigma_{\text{ref}} \right] \tag{2}$$

$$\cdot \left[\sum_{n=0}^{\infty} \sigma_n \cos(n\Omega t) + \sum_{n=0}^{\infty} \sigma_{\text{b,n}} \cos(n\Omega t) + \sigma_{\text{ref}} \right]^*, \tag{3}$$

where "$*$" denotes the complex conjugate. Since the multiplication $\cos(j\Omega t)\cos(l\Omega t)$ yields components of the form $\cos((j \pm l)\Omega t)$, the frequency component u_n constitutes only products of σ_j and σ_l with $j \pm l = n$, where σ_j and σ_l can be the scattering coefficients of the near-field contribution, background contribution or the contribution from the reference beam respectively. For the reference beam, it is always $j, l = 0$, because it is not affected by the tip oscillation. Furthermore, assuming $s_{\text{b,0}}, s_{\text{ref}} \gg s_{\text{b,j}}, s_j, s_{\text{b,l}}, s_l$ and $j, l > 0$, only products of $\sigma_{\text{b,0}}$ with $\sigma_{\text{b,n}}, \sigma_n$ and products of σ_{ref} with $\sigma_{\text{b,n}}, \sigma_n$ significantly contribute to u_n. The leading term of the frequency component u_n is then given by

$$\begin{aligned} u_n = {} & \sigma_{\text{b,n}}\sigma_{\text{ref}}^* + \sigma_{\text{b,n}}^*\sigma_{\text{ref}} \\ & + \sigma_n\sigma_{\text{ref}}^* + \sigma_n^*\sigma_{\text{ref}} \\ & + \sigma_{\text{b,n}}\sigma_{\text{b,0}}^* + \sigma_{\text{b,n}}^*\sigma_{\text{b,0}} \\ & + \sigma_n\sigma_{\text{b,0}}^* + \sigma_n^*\sigma_{\text{b,0}}. \end{aligned} \tag{4}$$

Each line in equation 4 has the form

$$s_1 e^{i\phi_1} s_2 e^{-i\phi_2} + s_1 e^{-i\phi_1} s_2 e^{i\phi_2} = 2s_1 s_2 \cos(\phi_1 - \phi_2). \tag{5}$$

Application of this relation leads to the formula for u_n presented in the main text:

$$u_n = 2s_{ref}[s_{b,n}\cos(\phi_{b,n} - \phi_{ref}) + s_n\cos(\phi_n - \phi_{ref})] \\ + 2s_{b,0}[s_{b,n}\cos(\phi_{b,n} - \phi_{b,0}) + s_n\cos(\phi_n - \phi_{b,0})].$$

(6)

List of Figures

List of Abbreviations

AFM	Atomic force microscopy.
CCD	Charge-coupled device.
DGTD	Discontinuous Galerkin time-domain.
EEL	Electron energy-loss.
EELP	Electron energy-loss probability.
EELS	Electron energy-loss spectroscopy.
EOT	Extraordinary optical transmission.
FIB	Focused ion beam.
IBL	Ion beam lithography.
ITO	Indium tin oxide.
LDOS	Local density of states.
LHC	Left handed circularly.
LSPP	Localized surface plasmon polariton.
NA	Numerical aperture.
NIR	Near infrared.
OPO	Optic parametric oscillator.
PDM	Point dipole model.
PID	Proportional integral differential.
PSW	Plasmonic slot waveguide.
RHC	Right handed circularly.
SA coupler	Slot antenna coupler.
SEM	Scanning electron microscopy.
SHG	Second harmonic generation.
SNOM	Scanning near-field optical microscopy.
a-SNOM	aperture-type SNOM.
s-SNOM	scattering-type SNOM.
SPP	Surface plasmon polariton.
STEM	Scanning transmission electron microscopy.
TEM	Transmission electron microscopy.
TL coupler	Transmission line coupler.
TM	Transverse magnetic.
VIS	Visible.
ZLP	Zero-loss peak.

Publications

Parts of this thesis have already been published in refereed scientific journals:

- M.Prämassing, T. Leuteritz, HJ. Schill, A. Fassbender, S. Irsen and S. Linden, *Freestanding metasurfaces for optical frequencies*, Opt. Lett. **44** (2019) 2105
  `https://doi.org/10.1364/OL.44.002105`

- M. Prämassing, M. Liebtrau, HJ. Schill, S. Irsen and S. Linden, *Interferometric near-field characterization of plasmonic slot waveguides in single-and poly-crystalline gold films*, Opt. Express **28** (2020) 12998
  `https://doi.org/10.1364/OE.384629`

Acknowledgements

description of his methods.

Lastly, I want to thank two great scientists in the field of nanophotonics working at the RWTH Aachen University. Andreas Heßler was the first fellow student I got to know at the very beginning of my studies in physics in Aachen. He accompanied me through the whole time of my bachelor and master studies as a very good friend and contributed to this thesis with very helpful comments and discussions. Special thanks also go to Prof. Thomas Taubner, who initially evoked my interest in the topic of nanophotonics and gave Andreas and me the opportunity to work in his nano optics group during our graduation.